KU LEUVEN

ARENBERG DOCTORAL SCHOOL
Faculty of Science

Inclusions in yield stress or highly shear-thinning dispersions

Blandine Barabé

Supervisors:
Prof. Dr. M.P. Lettinga
Dr. D.Z. Gunes
(Nestlé Research, Lausanne)

Dissertation presented in partial
fulfillment of the requirements for the
degree of Doctor of Science (PhD):
Physics

May 2021

Inclusions in yield stress or highly shear-thinning dispersions

Blandine BARABÉ

Examination committee:
Prof. Dr. J. Van de Vondel, chair
Prof. Dr. M.P. Lettinga, supervisor
Dr. D.Z. Gunes, supervisor
(Nestlé Research, Lausanne)
Prof. Dr. C. Clasen
Prof. Dr. C. Glorieux
Prof. Dr. C. Bartic
Prof. Dr. E. Koos

Prof. Dr. M. Vamvakaki
(University of Creta)

Dissertation presented in partial fulfillment of the requirements for the degree of Doctor of Science (PhD): Physics

May 2021

Uitgegeven in eigen beheer, Blandine Barabé, Celestijnenlaan 200A box 2402, B-3001 Leuven (Belgium)

Preface

This PhD received funding from the European Union through an ESR grant, within the Horizon 2020 Marie Curie-Sklodowska Innovative Training Network Distruc, Grant Agreement No. 641839.
My main institution within Distruc, the Nestlé Research Center in Switzerland, is warmly acknowledged. So is my other host institution, the Forschungszentrum Jülich (FZJ) in Germany, and my secondment institution, FORTH, Greece.
Both Dr. D.Z. Gunes (Nestlé) and Prof. Dr. M.P. Lettinga (FZJ) are acknowledged for supervising this PhD. I would also like to thank key scientific collaborators: S. Abakumov, Dr. L. Chambon, Dr. J. Engmann, Dr. E. Moghimi, S. Nicolae, Prof. Dr. G. Petekidis. For their reviewing of the manuscript, I would like to thank the jury, and my manuscript re-readers: Dr. P. Drews, Dr. I. Flammia, Dr. L. Oluwasayo, G. d'Oria and Dr. C. Maurer. For the general scientific and technical discussions, I would like to acknowledge the Distruc community and the three research groups I have been part of during this PhD: *Virtual Prototyping* at Nestlé, *IBI-4* at the FZJ, and the *Polymer & Colloid Science* group in FORTH.
Beyond the daily research work, I enjoyed the opportunities to reinforce my skills as a researcher. I am in particular very grateful to the university of KU Leuven for the high level training offer available at the doctoral level.

In short, this PhD was a rich work experience, throughout industrial and academic institutions, countries, and languages. Beyond the science, a warm and friendly work environment is a blessing and I surely enjoyed the atmosphere of the Distruc meetings and of my research groups...the Waffle Wednesdays, the Stammtisch...On the private side, it has been a pleasure to share this journey with solid friends, (good-) old or met along the way, and with my family.
A deep thank you.

Abstract

Sedimentation of non-buoyant inclusions can be decelerated by suspending the inclusions in highly viscous matrices and it can even be stably arrested when the matrix has a large enough yield stress. Macroscopic properties of both inclusion and suspending fluid are used to predict inclusion drag enhancement in highly shear-thinning fluids and stability in yield stress fluids. The influence of inclusion fraction on the rheology of yield stress fluids was rationalized by micro-mechanical laws. Beyond their strong fundamental relevance, properties at rest and under shear of highly shear-thinning and yield stress fluids containing inclusions echo shelf-life and process challenges for consumer products, building materials, and can explain geological phenomena.

In this PhD work, we decided to use model systems to tackle three different questions in a generic way:

i the influence of model colloidal anisotropic suspensions on inclusion stability.
ii the influence of inclusion fraction on the rheological properties of a model colloidal gel.
iii the relevance of the use of macroscopic stability criterion for immersed small cylinders consisting of disk stacks, sinking through the surface of a jammed yield stress fluid.

Goal i: in ch. 3, the sedimentation of large non-interacting spherical inclusions through networks of model mono-disperse, slender colloidal rods is investigated at low Reynolds numbers. The influence of rod concentration, rod length, and inclusion stress on the inclusion's creeping motion is investigated. The decrease of sedimentation speeds as a function of rod concentration is compared to the prediction based on the Stokes law, using the zero-shear viscosity from an adapted version of the Doi-Edwards theory for semi-dilute colloidal rods suspensions. The experimental speeds display the same concentration dependence as the zero-shear viscosity, and are thus strongly dependent on the rod length. The experimentally determined sedimentation speed is, however, a fraction of 2 and 4 lower than expected for rods of 0.88 and 2.1 μm, respectively. The results for both rod lengths superimpose when plotted against the overlap concentration, demonstrating at an extra dependence on the entanglement, of which we discuss the possible origin.

Goal ii: in ch. 4, the influence of the inclusion fraction on rheological properties of model depletion gel, composed of attractive spherical colloidal particles, is investigated. We observe that the reduced elastic modulus increases more steeply when the inclusion fraction increases, than predicted by the Krieger-Dougherty homogenization model. The crossover stress from LAOS rheometry also shows a stronger dependence on the volume fraction than predicted by the reduced yield stress homogenization mode, especially at high oscillation frequencies. The start up stress-strain relationship displays a yielding behavior in two steps, and we report similar results for the first peak stress from step rate tests than for LAOS crossover stresses. Depletion attractive forces between the colloids and the inclusions may explain those phenomena, as the homogenization model is only valid in the absence of inclusion-matrix direct contact, e.g. sticky interactions between inclusion and the matrix's elements. The two step yielding mechanism of the gels is affected by the inclusion fraction, as it induces a broadening of the first peak, while the second peak seems to be shifted to higher values of strain. This suggests a more gradual breaking of inter-cluster bonds than for the bare gel. Lastly, no significant influence of the inclusion fraction on gel recovery after submitting the gels to a well defined LAOS shear protocol was found.

Having studied the delayed sedimentation of inclusion and inclusion dependant yielding using colloidal matrices, goal iii is introduced: in ch. 5 we investigate the stability of disk stacks at the interface of a non-colloidal jammed system, considered as a continuum. The critical disk mass, associated to the onset of viscous sedimentation through the interface of milk foams, can be used to quantify the sinking yield stress, using critical yield number for immersed cylinders of small height. A clear correlation is obtained between the critical sinking stress of disk stacks at foams interface with apparent yield stresses obtained with vane rheometer. However, the correlation is foam type dependent. Taking the combined effect of interfacial forces and the influence of foam type on the sinking behavior of disks into account, we define foam type dependent stability criteria.

Samenvatting

Sedimentatie van niet-drijvende inclusies kan vertraagd worden door de inclusies te suspenderen in hoog-viskeuze matrices en zij kunnen zelfs stabiel vastgezet worden, indien de matrix een afdoende hoge vloeispanning heeft. De macroscopische eigenschappen van zowel inclusies als het fluïdum waarin deze gesuspendeerd zijn, worden gebruikt om versnelling van het slepen van inclusies door afschuifverdunnende vloerstoffe of fluïda en de stabiliteit in fluïden met vloeispanning te voorspellen. De invloed van wrijving tussen de inclusie en de matrix op de rheologie van vloeispannings fluïda werd op basis van micromechanische wetten gerationaliseerd. Afgezien van de grote fundamentele relevantie, weerspiegelen de eigenschappen van sterk afschuifverdunnende of vloeispannings fluïda met inclusies ook de levensduur-op-de-plank van voedingsmiddelen, proces uitdagingen voor consumentproducten, en geologische processen.

Wij hebben besloten om in dit proefschrift modelsystemen te gebruiken om drie verschillende vraagstukken te ontrafelen op een algemene manier:

i de invloed van model colloïdale anisotrope suspensies op de stabiliteit van inclusies.
ii de invloed van de inclusiefractie op de rheologische eigenschappen van een model colloïdale gel.
iii de relevantie van het gebruik van een macroscopisch stabiliteitscriterium voor ondergedompelde smalle cilinders, bestaande uit een stapel schijfjes zinkend door het oppervlak van een vastgelopen vloeispanning fluïdum .

Doel i: in hoofdstuk 3 onderzoeken we de sedimentatie van niet-interagerende bolvormige inclusies door netwerken van model monodisperse, slanke colloïdale staven bij lage Reynoldsgetallen. De invloed van de staafconcentratie, staaflengte, en de spanning uitgeoefend door de inclusie op de kruipbeweging van de inclusie wordt onderzocht. De afname van de sedimentatiesnelheid met toenemende staafconcentratie wordt vergeleken met de voorspelling op basis van de Stokes-wet, waarbij gebruik wordt gemaakt van een aangepaste versie van de Doi-Edwards theorie voor semi-verdunde colloïdale staaf suspensies. De experimenteel waargenomen sedimentatiesnelheden vertonen de zelfde concentratieafhankelijkheid als de nul-afschuif viscositeit en zijn daarmee sterk afhankelijk van de staaflengte. Deze snelheid is echter een factor 2 en 4 lager dan verwacht voor staven van lengte 0.88 en 2.1 μm, respectievelijk. De resultaten voor beide staaflengtes komen met elkaar wanneer als deze geplot worden als function de overlapconcentratie, ov dat er een extra afhankelijkheid is van de mate van verstrengeling, waarvan we de oorsprong bestuderen.

Doel ii: in hoofdstuk 4 onderzoeken we de invloed van de fractie van inclusies op de rheologische eigenschappen van model-depletie-gels, bestaande uit bolvormige colloïdale deeltjes en kleine polymeren. Wij zien dat de gereduceerde elastische modulus scherper toeneemt met toenemende inclusie-fractie dan voorspeld door het Krieger-Dougherty homogenisatiemodel. De overkruisingspanning uit LAOS rheometrie neemt scherper toe met de volumefractie dan voorspeld door het gereduceerde vloeispanning homogenisatiemodel, vooral voor hoge oscillatiefrequenties. Wij rapporteren soortgelijke resultaten voor de eerste piekspanning in een afschuifsnelheid-stap test. Attractieve depletiekrachten tussen de colloïiden en de inclusies kunnen mogelijk deze fenomenen verklaren, omdat het homogenisatiemodel alleen geldig is in de afwezigheid van directe contacten tussen inclusies en matrix, zoals plakkende interacties tussen inclusies en elementen van de matrix. Het twee-stap mechanische nageven van de gel wordt beïnvloed door de fractie van inclusies, omdat deze een verbreding van de eerste piek tot gevolg heeft, terwijl de tweede piek lijkt te schuiven naar hogere waardes. Dit suggereert een meer geleidelijk verbreken van verbindingen tussen clusters dan voor een kale gel. Ten slotte, kon een significante invloed van de inclusiefractie op het herstel van een gel, nadat het door grote oscillatie een afschuif-protocol verstoord was, niet aangetoond worden.

Doel iii: in hoofdstuk 5 wordt de stabiliteit van een stapel schijfjes in het contactoppervlak van een vastgelopen continue schuim beschouwd. De kritische schijfjes massa, geassocieerd met de aanzet van de viskeuze sedimentatie door het contactoppervlak van melkschuim, kan gebruikt worden om de afschuifspanning voor zinken te kwantificeren voor ondergedompelde cilinders van geringe hoogte. Een duidelijke correlatie is verkregen tussen de kritische zinkspanning van de stapel schijfjes aan het contact oppervlak van het schuim en de schijnbare vloeispanning, zoals verkregen door vaanrheologie. Echter, de correlatie hangt af van het type schuim. Door rekening te houden met het gecombineerde effect van oppervlaktekrachten en de invloed van het schuimtype op het zink gedrag van de schijfjes, kunnen we een stabiliteitscriterium definiëren dat afhangt van het schuimtype.

List of symbols

0.1 Symbols in modern latin letters

Symbol	Description	Units
a	Constant in the Papanastasiou equation	s^{-1}
A	Coefficient associated to the extra viscosity term associated to tube reptation	
$A(269)$	Absorption coefficient at a wavelength of 269 nm	
B	Exponential fit constant	
$\mathrm{B_n}$	Bingham number	
c	Rods concentration	$\mathrm{mg.mL^{-1}}$
$c*$	Rods overlap concentration	$\mathrm{mg.mL^{-1}}$
$c(269)$	Virus concentration determined at a wavelength of 269 nm	$\mathrm{mg.mL^{-1}}$
C_d	Viscous drag coefficient	
C_dp	Plastic drag coefficient	
d	Rod diameter	m
d_bare	Bare rod diameter	m
D	Microspheres diameter	m
De	Deborah number	
D_r	Rotational characteristic diffusion coefficient	$\mathrm{rad^2.s^{-1}}$
D_r0	Rotational characteristic diffusion coefficient in infinitely dilute conditions	$\mathrm{rad^2.s^{-1}}$
$\overline{D_\mathrm{r}}$	Diffusion coefficient accounting for the tube reptation dynamics in the zero-shear viscosity expression for semi-dilute rods colloidal suspensions	$\mathrm{rad^2.s^{-1}}$
D_t	Translational characteristic diffusion coefficient	$\mu\mathrm{m^2.s^{-1}}$
D_t0	Translational characteristic diffusion coefficient in infinitely dilute conditions	$\mu\mathrm{m^2.s^{-1}}$
$D_\mathrm{s,x}$	Diffusion constant in the direction transversal to the	$\mu\mathrm{m^2.s^{-1}}$

Symbol	Description	Units
	sedimentation direction	
$D_{\mathrm{s,z}}$	Diffusion constant along the sedimentation direction	μm^2.s^{-1}
E	Exponantial fit constant	Pa
e	Thickness of the UV-visible spectroscopic cell	cm
E_k	Kinetic energy in the drag coefficient definition	J
F_{C}	Interfacial force	N
F_{D}	Viscous drag force	N
F_{dp}	Plastic drag force	N
F_{I}	Inclusion buoyancy force	N
$F_{\mathrm{I,crit}}$	Critical inclusion buoyancy force	N
F_{Y}	Yield force	N
F_{Ymax}	Maximum yield force	N
G	Elastic modulus in shear	Pa
$G'(0)$	Elastic modulus of the bare yield stress fluid	Pa
$G'(\phi)$	Elastic modulus of a yield stress fluid loaded with a volume fraction ϕ of inclusions	Pa
G'_{min}	Minimum elastic modulus in the pre-conditioning tests	Pa
G'_{pl}	Plateau elastic modulus	Pa
$G'_{\mathrm{pl}}(0)$	Plateau elastic modulus of the bare yield stress fluid	Pa
$G'_{\mathrm{pl}}(\phi)$	Plateau elastic modulus of the bare yield stress fluid loaded with a volume fraction ϕ of inclusions	Pa
h	Height of the cylinder for the foams tests	m
$h(\dot{\gamma})$	Function of the shear rate used to define yield stress fluid behavior above the yield stress	
k	Consistency	Pa.s$^{\mathrm{n}}$
l	Characteristic length of the matrix used for comparison with the characteristic inclusion length	m m
l_{S}	Sedimentation length	m
L	Rod contour length	m
L_{P}	Rod persistence length	m
M_{w}	Rod molecular weight	g.mol^{-1}
M_{n}	Rod number average molar mass	g
n	Viscosity vs shear rate power law exponent	
P	Polymer pressure	Pa
$\mathrm{Pe_r}$	Rotational Peclet number	
$\mathrm{Pe_t}$	Translational Peclet number	
q_{s}	In the description of the depletion interaction between two colloids: intercolloid distance scaled by the colloid radius	
R	Inclusion radius	m
Re	Reynolds number	

Symbol	Description	Units
R_{g}	Radius of gyration	m
s	Characteristic surface area used in the definition of the drag coefficient	m^2
S	Surface area on which the buoyancy force is exerted	m^2
T	Temperature	K
$U_{\mathrm{dep}}(r)$	Asakura and Oosawa potential	J
V	Inclusion volume	m^3
V_{t}	Terminal speed for one inclusion	m.s^{-1}
V_S	Experimental sedimentation speed averaged on all inclusions	m.s^{-1}
$V_{\mathrm{overlap}}(r)$	Overlap volume in the Asakura and Oosawa potential	m^3
We	Weissenberg number	
Y	Dimensionless yield number	
$\mathrm{Y}_{\mathrm{crit}}$	Critical yield number	
$\mathrm{Y}_{\mathrm{crit,OT}}$	"On top" critical yield number	
t	Lag time	s

0.2 Greek symbols

Symbol	Description	Units
$\Delta\rho$	Density mismatch between the inclusion and the matrix	g.mol^{-1}
Δr_{x}	Displacement transversal to the sedimentation direction	m
Δr_{z}	Displacement along the sedimentation direction	m
γ	Shear strain	
$\gamma_{\mathrm{crossover}}$	Strain associated to the crossover of the elastic and loss modulus in the LAOS tests	
γ_{min}	Strain associated to the minimum elastic modulus in the pre-conditioning tests	
$g(\phi)$	Function associated to the homogenization model	
$\dot{\gamma}$	Shear rate	s^{-1}
ϵ_{269}	Extinction coefficient at 269 nm	L.mol^{-1}.cm^{-1}
η	Viscosity of a fluid, ex: Newtonian, yielded yield stress fluid	Pl
$\eta_m(\dot{\gamma})$	Shear rate dependent viscosity of the matrix	Pl
η_{S}	Solvent viscosity	Pl
ξ	Mesh size	m
λ_{r}	Rotational characteristic relaxation time	s
λ_{S}	Sedimentation characteristic time	s
λ_{t}	Translational characteristic relaxation time	s
ν	Number density of the rods	
ω	Angular frequency	rad.s^{-1}
ϕ, ϕ_{I}	Volume fraction of inclusions	
ϕ_{col}	Volume fraction of colloidal spheres	
ϕ_{G}	Volume fraction of colloidal spheres associated to the glass transition	
ϕ_{J}	Volume fraction (bubbles, drops..) associated to the jamming transition	
ϕ_{sol}	Solid fraction	
ϕ_{m}	Maximum packing fraction	
ρ_{I}	Inclusion density	g.mol^{-1}
ρ_{M}	Matrix density	g.mol^{-1}
τ	Shear stress	Pa
τ_{Y}	Yield stress	Pa
$\underline{\tau}_{\mathrm{Y}}$	Yield stress tensor	
$\tau_{\mathrm{C}}(0)$	Yield stress of the bare yield stress fluid	Pa
$\tau_{\mathrm{C}}(\phi)$	Yield stress of a yield stress fluid loaded with a	Pa

	volume fraction ϕ of inclusions	
$\tau_{\text{crossover}}(0)$	Crossover stress from LAOS tests for the bare gel	Pa
$\tau_{\text{crossover}}(\phi_{\text{I}})$	Crossover stress from LAOS tests for the bare gel	Pa
	for an inclusion content ϕ_{I}	Pa
τ_{I}	Shear stress exerted by the inclusion	Pa
II_{τ}	Second stress invariant	
$\theta(s)$	Orientation of the tangent in the definition of	
	the persistence length	rad

0.3 Fundamental constants

Symbol	Description	Value
g	Gravity acceleration constant	9.81 m.s^{-2}
k_B	Boltzmann constant	1.3806·10^{-23} J.K^{-1}
N_a	Avogadro number	6.022·10^{23} mol^{-1}

0.4 Abbreviations

Symbol	Description
FZJ	Forschungszentrum Jülich
H-B	Herschel-Bulkley
K-D	Krieger-Dougherty
MSD	Mean square displacement
PMMA	Poly(Methyl Methacrylate)
pnipam	Poly(N-isopropylacrylamide)
SDE	Stokes Doi-Edwards
wt	Wild type

0.5 Thesaurus

Symbol	Description
Brownian motion	Thermal driven motion.
Colloidal particles	Nanometric to micrometric particles, thermally driven.
Inclusion creeping motion	Inclusion moving at Re $<$ 1.
Depletion forces	Attractive forces resulting from an imbalance in osmotic pressure.
Filler	Inclusion added to a matrix to tune ex: mechanical properties.
Homogenization model	Model that tackles a heterogeneous problem by an homogeneous law.
Isotropic suspension of colloidal rods	Colloidal rods suspension with neither orientational nor positional order.

Contents

Preface i

Abstract iii

Samenvatting v

List of symbols vii
- 0.1 Symbols in modern latin letters vii
- 0.2 Greek symbols x
- 0.3 Fundamental constants xii
- 0.4 Abbreviations xii
- 0.5 Thesaurus xii

Contents xiii

List of Figures xvii

List of Tables xxix

1 Introduction 1
- 1.1 Relevance 1
- 1.2 Motivation and aim 3
- 1.3 Outline 4

2 State of the art 7
- 2.1 Yield stress fluids 7
  - 2.1.1 What is a yield stress fluid? 8
  - 2.1.2 Yield stress fluids: main descriptive models 8
  - 2.1.3 Microstructural origin of the yield stress 12
- 2.2 Inclusions suspending abilities 14
  - 2.2.1 Predicting stability from macroscopic parameters 15

2.2.2 Review of theoretical and experimental studies 20
2.2.3 Inclusions in viscous, shear thinning fluids 32
2.3 Model systems: criteria and selection 36
2.3.1 Matrix selection 36
2.3.2 Non-Brownian inclusions 41

3 Stability of beads in suspensions of rod-like viruses 45
3.1 Introduction 45
3.2 Theory 47
3.3 Materials 51
3.3.1 Sedimentation experiments 51
3.3.2 Diffusion experiments: orientational and translational tracking of fd viruses 56
3.4 Results 58
3.5 Discussion 62
3.5.1 Absence of a yield stress 62
3.5.2 Discrepancy between experimental and theoretical speeds 62
3.5.3 Note on the overlap concentration 65
3.5.4 Outlook: feasibility of pnipam-coated fd gel 66
3.6 Conclusion 67
3.7 Acknowledgements 68

4 Rheology of doped gels 69
4.1 Introduction 69
4.2 Depletion interaction notion and volume fraction dependence phenomenology 71
4.3 Materials 72
4.3.1 Matrix 72
4.3.2 Depletant 72
4.3.3 Inclusions 73
4.3.4 Sample preparation 74
4.3.5 Analysis techniques: Rheology and Imaging 74
4.4 Results 78
4.4.1 Imaging 78
4.4.2 Linear tests 79
4.4.3 Non-linear tests 83
4.5 Discussion 89
4.6 Conclusions and outlook 91
4.7 Acknowledgments 92

5 Critical sinking stress of disks through a foam 93
5.1 Introduction 93
5.2 Theory 95

5.3 Materials and methods 97
5.3.1 Sample preparation 97
5.3.2 Test setup 98
5.3.3 Test protocol: disk sinking tests 99
5.4 Results 100
5.4.1 Results of the disk settling trials 100
5.4.2 Comparison of disk settling trials with vane rheometry data 102
5.5 Discussion 104
5.6 Conclusion 106
5.7 Acknowledgements 107

6 Conclusion 109
6.1 Outlook 111

A Pnipam grafting of fd rods: preparation and rheology 113
A.1 Introduction 113
A.2 Materials 113
A.2.1 Samples characteristics 113
A.2.2 Validation of the grafting procedure 114
A.2.3 Gel formation and characteristics 114
A.3 Results 117
A.3.1 Grafting of pnipam on fd virus 117
A.3.2 Rheology of pnipam grafted fd gels 118
A.4 Conclusion 118
A.5 Acknowledgements 120

Bibliography 121

Scientific communication 137
A.6 Publications in peer-reviewed journals 137
A.7 Posters 137
A.8 Presentations in international conferences or workshops 138

List of Figures

1.1 Gravity effects of blue spherical inclusions in a white yield stress or shear-thinning dispersion. 3

1.2 Research topics from left to right. The inclusions, depicted in blue, are large enough for the matrix to be considered as a continuum. i: effect of anisotropic colloidal particles, depicted in black, on sedimentation of a large inclusion. The arrow represents the gravity force. The rods are bigger than real for purpose of explanation. ii: effect of the increase of inclusion concentration on gels' linear and non-linear rheological properties, the arrows illustrate the velocity vectors. iii: study of foams yielding by disk sinking, the arrow represents the gravity force. 4

2.1 Flow curves (Shear stress vs strain) of typical Newtonian and non-Newtonian fluids. a) Shear stress as a function of shear rate for Newtonian, shear-thinning, and shear-thickening fluids. b) The yield stress fluid samples behave elastically until the critical shear strain is reached: the shear stress increases with the shear rate with a slope G until the yield stress is reached. Above that critical strain value, the shear stress is independent of the shear strain. c) Shear stress as a function of shear rate for two types of yield stress fluids. The Bingham fluids flow with a constant viscosity while the H-B or Casson fluids are shear-thinning above the yield stress. For yield stress fluids, below the yield stress, the stress is independent of the shear rate. 10

2.2 Summary of the characteristic yield stress microstructures. Adapted from Nelson et al. 2017 [115] and Mewis et al. 2012 [106]. The yield stress fluids are separated in “repulsion dominated” and “attraction dominated” categories and illustrative pictures are presented for both [115]: A colloidal glasses, B emulsions C foams, D colloidal gel, E electro/magnetorheological fluid, F fiber gel. In the sketch for the repulsion dominated systems [106], the caging notion is illustrated: the grey particle at the center is caged by the surrounding particles in black and white. 13
2.3 a) Jamming diagram for repulsive colloidal spheres (grains, bubbles, droplets etc...). The physical state of suspensions of spheres is mapped as a function of temperature, inverse suspension density and applied load. Inside the clear zone, the grains are jammed. Outside, they can flow past each other. Taken from Trappe et al. 2001 [155]. b) Gelation diagram for attractive colloids. The physical state of the suspension is mapped as a function of the inverse of the scaled attraction energy, the inverse of the volume fraction and the scaled applied stress. Inside the clear zone, the suspension are gelled, outside they have a liquid-like behavior. Taken from Trappe et al. 2001 [155]. . . . 14
2.4 Force balance of a spherical inclusion stably immersed in a yield stress fluid. The inclusion, of radius R, volume V and density ρ_{I}, is immersed in a fluid of yield stress τ_{Y} and density ρ_{M}. In this situation, there is a balance between the buoyancy force of the inclusion, $\boldsymbol{F}_{\mathrm{I}}$, and the reaction force exerted by the matrix, $\boldsymbol{F}_{\mathrm{M}}$. 15
2.5 Three different trajectories for a spherical inclusion. a) Pure Brownian motion. b) Pure sedimentation motion. c) Combination of Brownian and sedimentation motion. 18
2.6 a) Active inclusion at rest and under shear, there is a mechanical cohesion between the inclusion and the matrix. b) Passive inclusion at rest and under shear. At rest, there is an intermediate layer, depicted in white, between the matrix and inclusion, either solvent, or interface. Under shear, there is slip at the inclusion interface, energy is dissipated in the mobile intermediate layer. There is no mechanical cohesion between the inclusion and the matrix. Adapted from Chen et al. 1999 [30]. 24
2.7 Numerical simulation of the yielded region around a smooth hard spherical inclusion sedimenting in a Bingham fluid in the creep limit [17]. The yielded "liquid" region is in white, while the blue zone surrounding it as well as the inclusion’s polar cap in blue are unyielded, "solid" regions. Adapted from Beris et al. 1985 [17]. 25

2.8 Drag coefficient as a function of the dimensionless yield number from finite elements simulations. a) For a bounded Bingham fluid [15] for varying sphere diameter to tube diameter ratios: from the 2:1 benchmark problem to 50:1, which matches unbounded results [17]. Adapted from Blackery et al. 1997. b) Drag coefficient for an inclusion falling in a viscoelastic H-B fluid, expressed as a function of the Deborah (De) number [58]. At low De numbers, elasticity is neglectible and the results agree with Beris simulations [17] for simple Bingham fluids. Taken from Fraggedakis et al. 2016 [58]. 26

2.9 Yielded borders in white and velocities colormap for two type of inclusions. The color code correspond to velocity fields where dark blue corresponds to no motion and red is the highest velocity. a) Two spheres settling in the wake in a Bingham fluid. The white line between the inclusions indicates that the inclusions are connected by a plug of unyielded material (although that is not reflected in the color code). Adapted from Chaparian et al. 2018 [26]. b) Axisymmetric bat inclusion. The bat shape is surrounded by a white diamond shape border that contains unyielded material. Adapted from Chaparian et al. 2017 [24]. 28

2.10 Critical yield number as a function of inclusion shape and orientation for adhering inclusions. As a note, the estimate for the spheres critical yield number is indicated by a discontinuous line. It is higher than the 0.143 value in Beris and Tabuteau's works, which is attributed to elastic effects [58]. Adapted from Jossic et al. [78]. 30

2.11 Summary of the critical yield numbers as a function of surface properties, shape and the presence of a second inclusion in the wake. 30

2.12 For several micellar suspensions, drag coefficient K normalized for wall effects with the coefficient $\mathrm{K_N}$, as a function of the Weissenberg number. Different symbols correspond to different experimental systems, for which the nature of the micellar building block, and electrostatic properties vary. From Mendoza et al. [104]. 34

2.13 a) Structure of fd virus: a DNA strand at the middle is covered by coat proteins: g3p, g6p, etc...Proteins functional groups can be used to graft chemicals on the surface of fd virus, and the overall charge of the biological colloidal rods is negative. b) Sketch of a charged fd rod of length L and diameter d_{bare} and effective diameter d_{eff} in an ionic solvent. 38

2.14 Phase diagram of fd virus as a function of concentration, ionic strength, and grafting of PEG polymer. The sketches illustrate the phases' characteristics, and for illustrational purpose the aspect ratio is smaller than for fd. For high concentrations and ionic strengths, the colloidal rods are in the nematic phase. Below the experimental points, where the line is a guide for the eye, the colloidal rods are in the isotropic phase. The phase diagram is adapted from Grelet et al. [64], and the rods sketches from Stephen Lower's work, http://chemwiki.ucdavis.edu/. 39

2.15 a) Sketch for the depletion interaction induced by polymer coil of radius r_S around two colloids or radius R separated by a distance r. Adapted from Guu [68]. b) Depletion potential as a function of the distance r between the two colloids. Adapted from Koumakis [91]. 41

2.16 Two step yielding of an attractive PMMA colloids depletion gel. The stress first increases elastically when the stress increases, until a stress overshoot peak is reached, which marks the onset of plastic deformation. For higher strains, a second stress overshoot is reached. The graphs on glasses and attractive glasses also display stress overshoot peaks which are a signature of structural yielding. From Koumakis et al. 2011 [88]. 42

2.17 Characteristic features: inclusion of diameter $2R$ in a background composed of anisotropic particles (not to scale) of characteristic dimension l. 43

3.1 Sketches of dispersed colloidal rods in two concentration ranges, which affects the viscosity of the dispersion. On the left, rods are so dilute that they can freely rotate, where the tips of the rods describe a sphere of diameter equal to the rod length, which is the rod's excluded volume. In the dilute state, these sphere do not overlap, $c < c*$, and the associated viscosity is defined as the sum of the solvent viscosity and the viscosity associated with the rotational diffusion of each rod inside the excluded volume. On the right, the concentration is so high that the spheres overlap, so $c > c*$. According to the tube model [44], a single rod diffuses out of a confining tube formed by the surrounding rods, which size is a function of the rods concentration. The viscosity in this semidilute state is defined as the sum of the solvent viscosity, the viscosity associated to rotational diffusion in the dilute state and a term taking into account the concentration dependant tube reptation. 48

3.2 Viscosity as a function of shear rate for fd virus Y21m bare, grafted with PEG polymers at an ionic strength of 100 mM and Y21m bare at 10 mM (20 mM Tris), at a concentration of c = 6.8 mg/mL. The marks on the ordinate axis are theoretical calculations for the zero-shear viscosity, as detailed in eq. 3.1. Adapted from Lang et al. [93]. 49
3.3 AFM picture of fd virus [74]. The contour length is the length of the fully stretched virus [14], while the persistence length is directly proportional to the rod's bending rigidity [151, 14] and is calculated using the function $\theta(s)$ represented on the picture, where s is the position around the contour length and $\theta(s)$ the orientation of the tangent at this position [14]. 50
3.4 a) Sketch illustrating the notion of mesh size for an isotropic suspension of colloidal rods. b) Mesh size as a function of rods concentration for pf1 and fd. 52
3.5 a) Scanning Electron Micrograph of the polystyrene inclusions. Adapted from Polysciences Inc. website. b) Polystyrene inclusions, in black, in a fd virus solution at c(fd) = 7 mg/mL, inclusion stress of 1.6 mPa. 52
3.6 a) Home-built horizontal microscopy setup used at the FZJ. From left to right, the white light source and corresponding lenses set and polarization filter, the slot for the sample holder, microscope objective, revolver, tube and camera. b) Keyence digital microscope used at the Nestlé Research Center. From left to right, the planar white light source on which a polarizing filter can be adapted, the sample holder, and the microscope objective. The microscope head is tilted of 90°, which allows for horizontal imaging. 54
3.7 Image processing. a) Raw picture b) Thresholded picture. c) Example of inclusion detection for the pictures from the FZJ setup, see fig. 3.6. The initial raw picture (fig. a)) is overlayed with red detection circles centered on the inclusions. The latter were detected with the *tp.batch* command on the thresholded, binary pictures. d) Example of inclusion detection for the pictures from the Nestlé Research Center setup. The initial raw picture is overlayed with detection squares centered on the inclusions. The latter were detected with the *label* command on thresholded, binary pictures. 56

3.8 Filtering process for $c(\text{fd}) = 7$ mg/mL, $I = 10$ mM and $\tau_\text{I} = 1.6$ mPa. a) Unfiltered sedimentation lengths as a function of time. The sedimentation length is the sedimentation height of the inclusions, minus the height in the first frame. b) Sedimentation length as a function of time, post filtering using the speeds histogram. Scatter: averaged trace. Red line: linear regression of the averaged trace. c) Speeds histogram. d) Mean square displacement (MSD) in the direction transversal to sedimentation, x and in the direction parallel to sedimentation, z as a function of the lag time. Above lag times of some seconds, the MSD in the x direction has a slope of 1, and the MSD in the z direction has a slope of 2. 57

3.9 Rotational and translational diffusion constants for fd and pf1 virus as a function of number density times the cubed virus length. The diffusion constants were obtained from fluorescent imaging experiments. 58

3.10 Raw sedimentation speed as a function of inclusion stress, with linear regression fits (full lines) for different concentrations of fd virus: a) 0 mg/mL b) 3 and 5 mg/mL and c) 7 and 9 mg/mL. 59

3.11 Slopes obtained from fig. 3.10 a)-c) as a function of fd rods concentration. The solid line is the SDE prediction, and the dashed line is the SDE prediction divided by a factor 2.5. . . . 60

3.12 a) Reduced sedimentation speed for fd and pf1 at an inclusion stress of 1.6 mPa with the SDE prediction. In the case of pf1, the flexibility of the rods was taken into account by using two values of the constant A, which is a coefficient in the modified diffusion coefficient expression [93], see section 3.2. b) Reduced sedimentation speed as a function of reduced rod concentration c/c^*, for both systems fd wild type and pf1. 61

3.13 Sketch illustrating the definition of the characteristic sedimentation, translational and rotational times. a) The characteristic sedimentation time is the time needed for an inclusion to fall of one inclusion diameter. b) The network rotational relaxation time is defined as the time for a colloidal rod to change its orientation by an angle α. c) The network translational relaxation time is the time needed for a rod to translate of one inclusion diameter. 62

3.14 a) Rotational and b) translational Peclet number for fd and pf1 as a function of rod concentration rescaled by c^*. The Peclet numbers are calculated using sedimentation rates from experiments. The characteristic diffusion times at the corresponding rod concentrations are extrapolated from fig. 3.3.2. 64

3.15 Birefringence image of sedimenting 10 μm polystyrene spherical inclusions in a pf1 virus solution at c(pf1) = 2.8 mg/mL, inclusion stress of 1.6 mPa. Although the contrast is enhanced, and light intensity maximized in crossed polarized configuration, no birefringence around the falling inclusions is observed. 67

4.1 For a stock solution of PMMA colloidal spheres, linear elastic modulus scaled by the cubic colloids radius and by thermal energy k_BT as a function of colloids volume fraction. The experimental points correspond to PMMA colloids of radius ranging from 130 to 300 nm, dispersed in various organic solvents. The slope is of 30 below the glass transition, and 50 above. Adapted from Koumakis et al. 2012 [90]. 72
4.2 Sketch of the inclusion doped colloidal gel. Above, magnification of the colloidal solution, below, magnification of the colloidal solution next to the inclusion. The colloids as well as the characteristic cluster size are larger than in reality. 73
4.3 Optical microscopy image of the inclusions in the colloidal gel obtained using the FZJ's home-made setup. 75
4.4 Optical microscopy darkfield imaging of the PMMA colloidal gel doped with 5% inclusion fraction a) before b) and after pre-shear. The inclusion are in dark grey on a lighter gray background. . 76
4.5 Laser reflection images of the colloidal gel with 5% inclusion fraction, at different steps of the pre-conditioning tests. The inclusions appear white on a dark background. The samples are imaged just above the bottom plate. The left picture was taken after the pre-conditioning test at 300% strain, the right picture was taken after a later test, the pre-conditioning test at 800% strain. 76
4.6 Schematics of the test protocol. a) Pre-shear at high oscillation amplitude is followed by recovery, followed by the actual test: linear properties and their evolution are probed using dynamic frequency sweeps or time sweeps, while non-linear properties are assessed using strain sweeps and step rates. b) A preconditioning step is inserted between pre-shear and recovery: the sample undergoes oscillatory shear at specific amplitudes in order to tune the sample's properties [109]. 77

4.7 Linear properties of weak PMMA gels doped with density mismatched glass inclusions. (a) Second *Block* of the protocol: gel coarsening after rejuvenation for 0, 5, 10% of inclusion as probed by G'. The plateau values of the elastic modulus, G'$_{\text{pl}}$ were used to assess the influence of inclusion fraction on linear properties. The red lines correspond to exponantial fits performed in order to compare the gel structuration properties as a function of inclusion fraction. (b) Dynamic frequency sweeps corresponding to *Block 3* of the protocol, for several inclusion fractions. 80
4.8 Linear properties of weak PMMA gels doped with density mismatched glass inclusions. (a) Reduced plateau elastic modulus as a function of inclusion fraction. The trend for experimental points is up to 1.6 higher than predicted by the Krieger-Dougherty model. (b) Characteristic time obtained by an exponential fit of the dynamic time sweeps, for the three inclusion fractions. . . . 81
4.9 Linear properties of weak PMMA gels doped with density mismatched glass inclusions. Evolution of the plateau modulus G'_{pl} as a function of the number of rejuvenations for different inclusions fractions ϕ_{I}. 82
4.10 Yielding properties of weak PMMA gels doped with density mismatched glass inclusions. a) LAOS at $\omega = 1$ rad/s as a function of the inclusion fraction. b) Crossover strain from LAOS tests as a function of inclusion fraction and angular frequency. c) Crossover stress from LAOS tests as a function of inclusion fraction and angular frequency. Chateau's model for the reduced yield stress is a function of the reduced elastic modulus g(ϕ_{I}), and is depicted as a black line when the K-D type theoretical expression for g(ϕ) is used, and using brown symbols when the experimental plateau elastic modulus is used. 84
4.11 Yielding properties of weak PMMA gels doped with density mismatched glass inclusions. Step rate tests at shear rates of a) 2 s^{-1}, b) 0.5 s^{-1}, c) 0.05 s^{-1}. 85
4.12 Yielding properties of weak PMMA gels doped with density mismatched glass inclusions: step rate tests. a) Reduced peak stress, experimental data extracted from the stress overshoot at rates of 2, 1, 0.5, 0.01, 0.05 s^{-1}. Chateau's model for the reduced yield stress is a function of the reduced elastic modulus g(ϕ_{I}), and is depicted as a black line when the K-D type theoretical expression for g(ϕ) is used, and using brown symbols when the experimental plateau elastic modulus is used. b) Reduced peak strain, experimental data extracted from the stress overshoot at rates of 2, 1, 0.5, 0.01, 0.05 s^{-1}. 86

4.13 Yielding properties of weak PMMA gels doped with density mismatched glass inclusions. Step rate tests at various strain rates for a) $\phi_\mathrm{I} = 0\%$ b) $\phi_\mathrm{I} = 5\%$ c) $\phi_\mathrm{I} = 10\%$. 87
4.14 Pre-conditioning tests for the 10% inclusion sample. a) Dynamic time sweep following the pre-conditioning step for different pre-conditioning amplitudes. The plateau linear modulus is taken as the value of linear modulus at the end of the time sweep. b) Scaled plateau linear elastic modulus as a function of the pre-conditioning amplitude for three inclusion fractions. 88
4.15 Magnification of the colloidal suspension and the colloidal suspension at the vicinity of the wall. Upper figure: inspired by fig. 2.15, the depletion attractions between colloids are represented. The coils of linear polymer chains are modeled by brown disks. The depleted zones around the grey colloids, where the centers of the disks cannot penetrate, are depicted by a discontinuous line. Lower figure: also inspired by fig. 2.15, the depletion interactions at the wall between colloids and the inclusion is depicted. A depleted zone is depicted around the inclusion, depicted in darker gray than the colloids. 91

5.1 Foaming machines. a) Example of NDG machine with a capsule. Adapted from NDG website. b) Sketch of Aeroccino foaming device, top view displaying the stirring coil. Adapted from Völp et al. [158]. 97
5.2 Sinking disk in the foam. a) Upper view of a stack of black disks falling in a white milk foam. The foam is placed in a specifically designed beaker equipped with a centering rod glued to the bottom of the beaker: the disks are therefore well centered and stacked on the foam. b) Sketch illustrating the "Side view" of the stack of disks sinking in the foam along the centering rod. 98
5.3 a) Four edge vane operating in a foam layer. b) Tangent intersection method for the foam type A, with a foam total height of approx. 22 mm. There is an abrupt change in the slope, and the intersection of the two slopes is taken as a measure of the foam's yield stress. 100

5.4 Stability diagram of the disks of the foam of type A, with a foam total height of 20 mm. The stable and sinking situation are separated by a line, and depend on the probe overall mass, which is a linear function of the stacking height normalized by the disk diameter. On the right of the diagram, three pictures of the disks stacks set on the foam are displayed as a function of their position in the stability diagram. (i) For few disk stacks, the disk stacks are set on a planar foam interface. (ii) For higher stacking the interface gets curved. (iii) Even higher stacking overcome the foam strength, the foam interface breaks up and the disk stacks form tunnel shapes in the foam while they sediment. 101
5.5 a) Sinking and vane rheometry yield stress as a function of foam height, for foam types A (extracted foams) and B (Aeroccino foams). b) Sinking tests yield stress as a function of the vane rheometry yield stress. The two straight lines correspond to foams generated by two different techniques: the red line correspond to foams of type A and the black line to foams of type B. 102
5.6 a) Forces exerted on a cylinder of radius R, and small height h, volume V and density ρ_I, set at the interface of a yield stress fluid layer, where the yield stress fluid has a yield stress τ_Y and density ρ_M. The cylinder mass is just below the critical mass, according to experimental observations that account for interfacial forces. F_Y is the yield force, F_I the force exerted by the inclusion, F_C the interfacial forces. b) In orange, unyielded yield stress fluid, in blue, hypothetical corresponding yielded region. The sketch is inspired by the experimental shape of the interface prior to disk stack sinking and the theoretical shape of yielded regions for immersed squares and rectangles [118, 26]. 103
5.7 Yield force as a function of the critical buoyancy force substracted by the interfacial force. The two straight lines correspond to foams generated by two different techniques: the red line correspond to foams of type A and the black line to foams of type B. The slope of the curves has the meaning of a critical yield number. 104

A.1 Vial turning technique for a batch of successfully grafted fd-pnipam. 115
A.2 Auto-correlation functions $g_2(0) - 1$ as obtained by DLS for a fd-pnipam at the indicated temperatures. The relaxation of $g_2(0) - 1$ slows down when the gelation temperature is reached. 116
A.3 AFM pictures of a) fd wild type b) 2k pnipam coated fd virus, *batch 3*. 117

A.4 a) Oscillatory dynamic strain sweeps for a pnipam grafted fd virus sample at $c = 3$ mg/mL in a 100 mM Tris buffer. The first dynamic strain sweep is stopped right after yielding, defined here as G'<G". Then following recovery and equilibration of linear properties, a second dynamic strain sweep is perfomed, and stopped after yielding. b) Oscillatory dynamic time sweeps for a pnipam grafted fd virus sample at $c = 3$ mg/mL in a 100 mM Tris buffer. The time sweeps after the first and the second dynamic strain sweep start just after the critical strain in the strain sweeps corresponding to an higher viscous than elastic modulus has been reached. 119

List of Tables

5.1 "On top" critical yield number as a function of foam type and height. 104

Chapter 1

Introduction

1.1 Relevance

Suspensions of non-colloidal inclusions in a continuous complex fluid phase are omnipresent in industrial applications. They range from consumer products such as gellified emulsions for food [33] or medical [103] applications, to building materials for instance aerated or particle reinforced cement [39, 143, 48]; they can also be found in geological materials e.g. gas bubbles filled lavas [154, 8]. The viscoelastic properties of the continuous phase enables these materials to bear the mass of fillers for long shelf life [32]. In the case of structural materials such as cement, fillers are added to tune the visco-elastic properties [48]. As for food products, fat droplets of targeted size stabilized in high viscosity water based matrices, enable the tuning of specific mouthfeel [33]. Over long shelf life [33], or under external shear [125, 126] unwanted heterogeneities may appear in the products, as gravity induces sedimentation or creaming of solid fillers, bubbles or droplets [114], as depicted in fig. 1.1 resulting in altered end properties. Such challenges are especially crucial for extreme shear thinning fluids or weak, low elastic moduli gels, which are ubiquitous in foods for instance for the design of innovative products like particles laden foams or due to directives such as suppressing non-clean label ingredients or cutting fat content. Control of particle sedimentation is thus needed to predict product stability.

Assessing the stability of systems with solid inclusions in high viscosity fluids is also of fundamental relevance [32, 110, 71]: the ability of a matrix to stabilize inclusions over a long period of time or under shear, indeed relates to the existence of a real or apparent yield stress [17, 71], tuning the inclusion's stress within the dynamic to static range therefore allows one to measure the yield

stress. Most of the theoretical and experimental work performed on hard spherical inclusions in yield stress fluids was dedicated to the following purpose: establishing a macroscopic stability criterion to predict stability and flow. A dimensionless yield number for spherical inclusions has been defined theoretically [17, 15] and validated experimentally [149] to define the threshold for sphere stability.
However, the influence of the microscopic sub-elements of the yield stress fluids is often missing from stability or rheological studies of inclusions in yield stress fluids, considered as a continuum [148], due to the large ratio of inclusion to particles in the suspending fluid. It was shown however that yield stress fluids composed of anisotropic particles can hold inclusions significantly larger than what is suggested by the critical yield stress value, hinting at the existence of a local yield stress, higher than the macroscopically defined yield stress [51, 146]. A purely macroscopic description of inclusion stabilization by yield stress fluids thus needs to be enriched by further studies of effects induced by anisotropic particles in the matrix in order to understand the mechanisms at stake. In the case of highly shear-thinning viscoelastic liquids, the complexity of drag enhancement effects of inclusions sedimenting in suspensions composed of flexible chains would also benefit from studies on suspensions composed of model non-flexible chains or particles of which the relaxation mechanisms would be described at a microscopic level.

Another branch of studies has been dedicated to assessing the rheological properties of gels containing inclusions, especially the impact of increasing the inclusion fraction over linear [99] and non-linear properties [99, 3, 50]. As the process of yielding is an interplay between microscopic changes in the material surrounding the inclusion [88] and the sedimentation force exerted by the inclusion [17, 71], it is of interest to have a full understanding of this process using well defined model systems of which we describe the interaction with the inclusions at the microscopic level. It remains in particular to be investigated whether there exists an inclusion fraction threshold, for which combination of inclusion stress with external shear stress can enhance gel recovery [88].

The use of model systems supplies knowledge on how to better control sedimentation of large inclusions in highly shear-thinning dispersions or weak gels, where the matrix is considered as a continuum. The next step is then to assess to which extent this knowledge from the ideal case of model systems which can be described by macroscopic models can be transferred to the situation where the matrix has specific microstructural properties, which can vary significantly e.g. as in the case of foams, and possibly also display finite size effects.

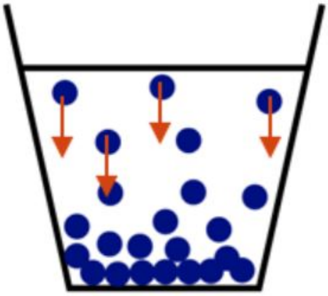

Figure 1.1: Gravity effects of blue spherical inclusions in a white yield stress or shear-thinning dispersion.

1.2 Motivation and aim

This PhD work aims towards increasing the general knowledge of the stabilization and rheological behavior of inclusion loaded highly shear-thinning suspensions and weak gels. We decided to use well defined model colloidal systems in order to provide generic answers to topics relevant for many real systems, and studied jammed systems closer to reality in the last chapter.

As presented in the last paragraph, the influence of anisotropic subelements on inclusions stabilization properties needs further investigation, using suspensions of model stiff colloidal rods. Indeed, in previously investigated model systems composed of anisotropic subunits, the subunits were very flexible or polydisperse. With regards to the rheology of yield stress fluids containing inclusions, the phenomenological models are relevant for a set of yield stress fluids commonly used in litterature. However, those rheological models remain to be tested on dispersions of model colloidal attractive spheres with well defined rheological properties. The influence of non-buoyant inclusions on yield stress fluid recovery of elastic properties following shear has also not been investigated. Lastly, the yielding of inclusions through a yield stress fluid interface has not been investigated in depth, neither with model nor real yield stress fluid experimental systems.

We present an experimental study of non-Brownian spherical inclusions in model colloidal suspensions with or without a yield stress. Fig. 1.2 summarizes the three topics addressed in this thesis: inclusion sedimentation in anisotropic suspensions, rheology of inclusion doped gels, and yielding through foams interface. We contribute to broaden knowledge on the influence of model rod-like colloidal suspensions on inclusions sedimentation: drag enhancement and stabilization, fig. 1.2 a). We then investigate the effects of an increasing inclusion fraction on the linear and non-linear rheology of model weak depletion colloidal gels, fig. 1.2 b) and on their recovery. Finally, we investigate the relevance of the immersed critical yield number for small cylinders to derive yield stresses from the yielding onset of disk stacks at milk foams interfaces, fig. 1.2 c).

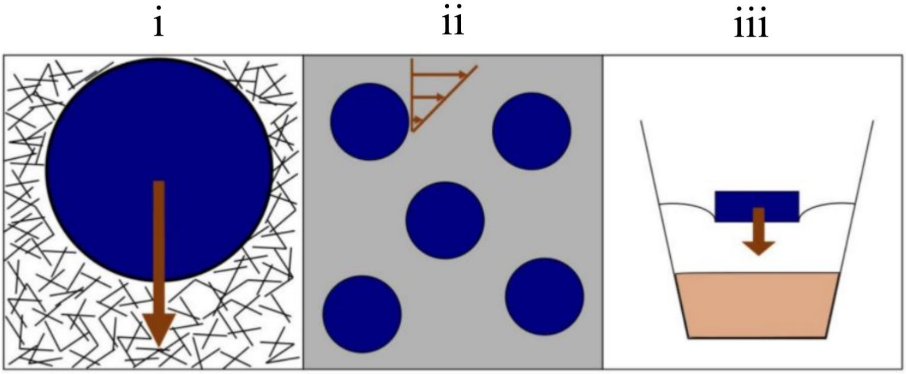

Figure 1.2: Research topics from left to right. The inclusions, depicted in blue, are large enough for the matrix to be considered as a continuum. i: effect of anisotropic colloidal particles, depicted in black, on sedimentation of a large inclusion. The arrow represents the gravity force. The rods are bigger than real for purpose of explanation. ii: effect of the increase of inclusion concentration on gels' linear and non-linear rheological properties, the arrows illustrate the velocity vectors. iii: study of foams yielding by disk sinking, the arrow represents the gravity force.

1.3 Outline

The thesis starts with a general overview of the literature in ch. 2 on yield stress fluids, inclusion stabilization in yield stress fluids and rheology of yield stress fluids containing density mismatched inclusions. Next, an overview of high shear-thinning viscoelastic fluids and inclusion drag reduction and enhancement in high shear-thinning viscoelastic fluids is given. Eventually, the choice of model systems is explained. Next, in ch. 3, a sedimentation study of large spherical inclusions in a network of colloidal rods is presented. The influence of rods concentration, length over sedimentation speeds is assessed and compared with theoretical predictions. The concentration dependance is well described by the prediction, however a length dependant quantitative discrepancy is noticed. The mismatch is attributed to crowding of the rod suspensions front of the inclusions, and the entanglement number could explain the length dependance.

Next, in ch. 4, the rheological study of large spherical inclusions in a matrix of colloidal attractive spheres is presented. In particular, the influence of an increase of the inclusion fraction on the linear and non-linear properties of the gels was studied. The experimental results deviate from the phenomenological model, which is attributed to attraction between the inclusion and the matrix. Lastly, in ch. 5, the yielding of foams by disks stacks set on top of the foam is investigated. Deviations from the immersed inclusion in model yield stress fluids predictions are assessed, and the influence of the test configuration and foam type on sinking studied. A foam and height dependant "on top" critical yield number is defined, lower masses yield the foam than in the immersed case and the complexity of the interstitial fluid may induce extra interfacial effects.

Ch. 6 summarizes the thesis work and an outlook is presented.

Chapter 2

State of the art

In this chapter, the state of the art of inclusion trapping by highly viscous fluids and rheology of complex fluids containing inclusions is discussed. For this discussion it is prerequisite to define what kind of complex fluids are needed to prevent sedimentation. Therefore, the notion of yield stress fluid is first introduced in section 2.1. The most common descriptive laws for yield stress fluids are introduced and the characteristic microstructural features of yield stress fluids are presented. Next, in section 2.2, the stability criterion used to predict the stability of an inclusion in a given yield stress fluid is introduced. An overview of relevant literature on both stable inclusions in yield stress fluids and flowing inclusions in yield stress fluids is presented. Sedimentation of inclusions in visco-elastic shear thinning fluids at vanishingly small sedimentation rates is also presented, as such complex fluids can also sustain inclusions for long characteristic times. Finally, in section 2.3, the relevance and physical properties of the models systems selected for the experimental studies are presented.

2.1 Yield stress fluids

In this section, we first introduce a daily life characterisation of yield stress fluids. The formalism in one dimension is introduced, followed by the characteristic microstructural features of yield stress fluids.

2.1.1 What is a yield stress fluid?

Ketchup [54], yogurt [66], cement [16] are examples of yield stress fluids that can be found in everyday applications. In the down to earth example of pouring ketchup on warm fries, no material flows out of the deformable bottle if the squeezing stress is too low. Upon increasing the squeezing stress above a certain value, the material flows out. More generally, a yield stress fluid is defined as a complex fluid that evolves from a solid like behavior (strain is proportional to stress) to a liquid like behavior (strain is proportional to stress rate) when the applied shear stress is higher than a critical shear stress, called the yield stress [35]. A specific weight bearing microstructure always displays solid-like behavior at rest, while the yielding to a stress causes the structure to flow.

Whether "true" yield stress fluids exist is still a matter of debate [13, 10, 35], as it is a question whether yield stress can be measured regardless of the experimental time and conditions or rather only "apparent" yield stress fluids, for which a yield stress is measured when the sample is probed below a certain experimental time but flows when the experimental time is extended. The yield stress can thus be regarded as a convenient engineering notion, that should be tied to its observation time.

2.1.2 Yield stress fluids: main descriptive models

The target of this subsection is to present the most common descriptive mathematical models for yield stress fluids. First, the models for liquids and solids under simple shear are described [98]. Next, the yield stress fluids models for viscous and shear-thinning behavior above the yield stress are detailed [98]. The validity of the models is discussed, and the definitions for the “yield stress” commonly found in literature are introduced.

Simple shear: Hookean solid, Newtonian and viscoelastic liquids and yield stress fluids

The simplest constitutive equation in the simple shear case is for a Hookean solid probed under a sliding plate rheometer. For this solid, the applied shear stress is proportional to the strain times the shear modulus as

$$\tau = G\gamma \tag{2.1}$$

where τ is defined as the ratio of the applied force F by the surface S, $\tau = F/S$, G is the elastic modulus in shear and γ is the normalized displacement in the shear direction.
For Newtonian liquids, the applied stress is proportional to the shear rate $\dot{\gamma}$ times the viscosity η, as depicted in fig. 2.1 a).

$$\tau = \eta\dot{\gamma}, \tag{2.2}$$

where $\dot{\gamma}$ is defined as the time derivative of γ, $\dot{\gamma} = \frac{d\gamma}{dt}$.
Lastly, in the more general case of viscoelastic liquids, the viscosity is shear dependent:

$$\tau = \eta(\dot{\gamma})\dot{\gamma}. \tag{2.3}$$

For instance, the viscosity of shear-thinning or pseudoplastic liquids decreases for increasing shear rates, as depicted in fig. 2.1 a). One of the most common model for shear-thinning fluids is the power-law model, where the viscosity is equal to a constant, the consistency k, times the strain rate to the power $n-1$, while n is smaller than one $\eta(\dot{\gamma}) = k\dot{\gamma}^{\text{n-1}}$. The power-law model does not, however, account for the viscoelastic properties of some shear-thinning fluids, which corresponds to time dependence effects due to structural relaxation.

Yield stress fluids behave like a solid below the yield stress τ_{Y} and like a liquid above. The formalism is then the following:

$$\tau = G\gamma \qquad \text{if} \quad \tau \leq \tau_{\mathrm{Y}} \tag{2.4}$$

as depicted in fig. 2.1 b)

$$\tau = \tau_{\mathrm{Y}} + h(\dot{\gamma}) \quad \text{if} \quad \tau > \tau_{\mathrm{Y}} \tag{2.5}$$

where h is a function of $\dot{\gamma}$, as depicted in fig. 2.1 c).

Simple shear yield stress fluid models

In this subsection, we discuss different functions $h(\dot{\gamma})$, depicted in fig. 2.1 c), for both viscous flow and shear thinning flow above the yield stress. One of the most common models is the Bingham model: above the yield stress, the Bingham fluid flows with a constant viscosity.

$$\tau = \tau_{\mathrm{Y}} + \eta\dot{\gamma} \quad \text{if} \quad \tau > \tau_{\mathrm{Y}}, \tag{2.6}$$

where η is the Bingham viscosity. This relationship is valid and frequently used for ketchup and some bitumen types [98]. Shear-thinning flow above the yield

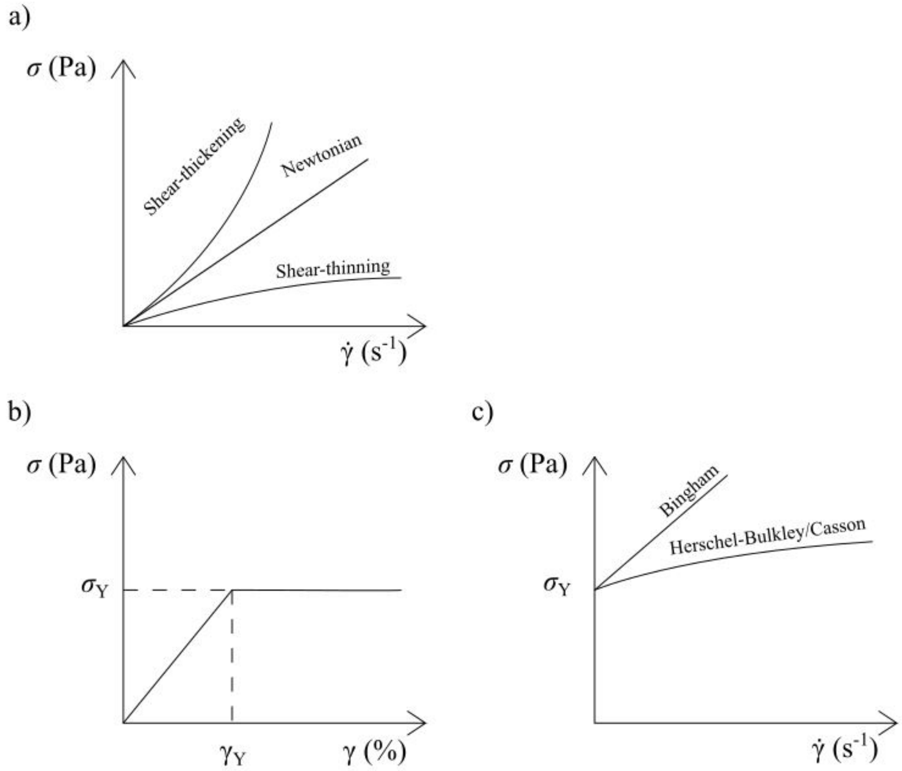

Figure 2.1: Flow curves (Shear stress vs strain) of typical Newtonian and non-Newtonian fluids. a) Shear stress as a function of shear rate for Newtonian, shear-thinning, and shear-thickening fluids. b) The yield stress fluid samples behave elastically until the critical shear strain is reached: the shear stress increases with the shear rate with a slope G until the yield stress is reached. Above that critical strain value, the shear stress is independent of the shear strain. c) Shear stress as a function of shear rate for two types of yield stress fluids. The Bingham fluids flow with a constant viscosity while the H-B or Casson fluids are shear-thinning above the yield stress. For yield stress fluids, below the yield stress, the stress is independent of the shear rate.

stress is encompassed by the Herschel-Bulkley (H-B) and Casson laws. The Herschel-Bulkley law is given by:

$$\tau = \tau_\mathrm{Y} + k\dot{\gamma}^n \quad \text{if} \;\; \tau > \tau_\mathrm{Y} \tag{2.7}$$

where n is an exponent smaller than one, and k the consistency.

The Casson model, especially used to describe the mechanical response of blood [98, 159] and food [98] is given by:

$$\sqrt{\tau} = \sqrt{\tau_{\mathrm{Y}}} + \sqrt{\eta\dot{\gamma}} \tag{2.8}$$

Improvement brought to the simple shear models

The above described constitutive equations describe simple shear flow. In most cases, such as processing cement or yogurt, the complex fluid requires a full three dimensional approach. In that case, the shear value above which the liquid yields is given by the von Mises yield criterion $II_{\tau} \geq (\underline{\tau}_{\mathrm{Y}})^2$ [125], with II_{τ} the second stress invariant and $\underline{\tau}_{\mathrm{Y}}$ the yield stress tensor. The three dimensional Bingham, H-B and Casson models are well described in relevant textbooks such as Macosko's [98].

It is also worth mentioning later improvements to the models that facilitated the implementation of the descriptive equations in computer simulations. Papanastasiou et al. [129] implemented an exponential term in eq. 2.6 that allows for a quick decay of the initial elastic term above the yield stress. In this way, only one constitutive equation is needed and the discontinuity at the yield stress value is suppressed. Here is the one dimensional Papanastasiou equation:

$$\tau = \left[\eta + \frac{\tau_{\mathrm{Y}}[1 - \exp(-a\dot{\gamma})]}{\dot{\gamma}}\right]\dot{\gamma} \tag{2.9}$$

where η is the viscosity of the yielded material and $a \in \mathbb{R}_+$ is the regularisation parameter.

A feature that is absent from the aforementioned laws is the time dependence of a yield stress' physical properties such as aging [65] (i.e. the evolutions of properties with the age of the system) and thixotropy [111] (reversible dependence of microstructural and rheological properties on the flow history). As an example for aging, in laponite gels [65], the elastic modulus keeps increasing over time as the number of interparticles links between the laponite platelets keeps increasing. Thixotropy [111] is a property of fluids where the viscosity decreases under high shear and then increases when submitted to lower shear due to yield stress fluid reversibility. This macroscopic shear dependence of the viscosity is associated to microstructural effects of breakage of interconnected clusters under high shear and reconstruction at rest [109].

Static and dynamic yield stresses

Finally, one should distinguish between two different experimental "yield stresses", namely the static and the dynamic yield stresses. The static yield stress is the stress at which flow is initiated and is experimentally determined by shearing the sample from low to high stresses [51]. The dynamic yield stress is the stress for which flow stops and is determined by shearing the sample from high stresses, where the samples is fluidized, to lower stresses [51].

2.1.3 Microstructural origin of the yield stress

This section addresses the question of the required microstructural features for a material to qualify as a yield stress fluid [115, 35]. Key parameters to obtain a yield stress fluid starting from simple constitutive elements are introduced. Note that only yield stress fluids of physical origin are introduced, that is yield stress fluids where the interactions between the constituting particles are non-covalent.

Generally speaking, yield stress fluids are structurally characterized by a three dimensional, stress bearing percolating network [155], see fig. 2.2. They can be separated in two subcategories according to the nature of the interactions between their constitutive particles: repulsive or attractive [115, 51].

Yield stress fluids of repulsive particles are often called “glasses” [51]. In the case of colloidal suspensions, where colloids are Brownian particles due to sizes generally smaller than ten microns, the colloids undergo a glass transition above a packing fraction of $\phi_{\mathrm{G}} = 0.58 - 0.6$ [19]. Here the yield stress is associated to crowding [132, 155, 19]. On fig. 2.2 a), a crowded structure of hard spheres is depicted, where a single particle is caged by the surrounding particles so that its thermal motion is constrained [19]. Examples of crowded structures are concentrated solutions of particles and concentrated solutions of polymer microgels [115, 99, 51]. The key control parameters to obtain a yield stress fluid starting from repulsive particles are depicted on Liu and Nagel’s [97] crowding diagram, displayed on fig. 2.3 a). The area for which a jammed solid is obtained, is mapped as a function of ρ, the particle density of the system, T the temperature and τ, the stress applied to the suspension.

In the case of non-Brownian suspensions of soft particles, the particles undergo a jamming transition when the concentration exceeds a maximum packing fraction, which is close to the random close packing fraction in the case of repulsive three dimensional monodisperse spheres, $\phi_{\mathrm{J}} = 0.64$ [19]. This is the case for emulsions [115, 33, 34] and foams [139, 34].

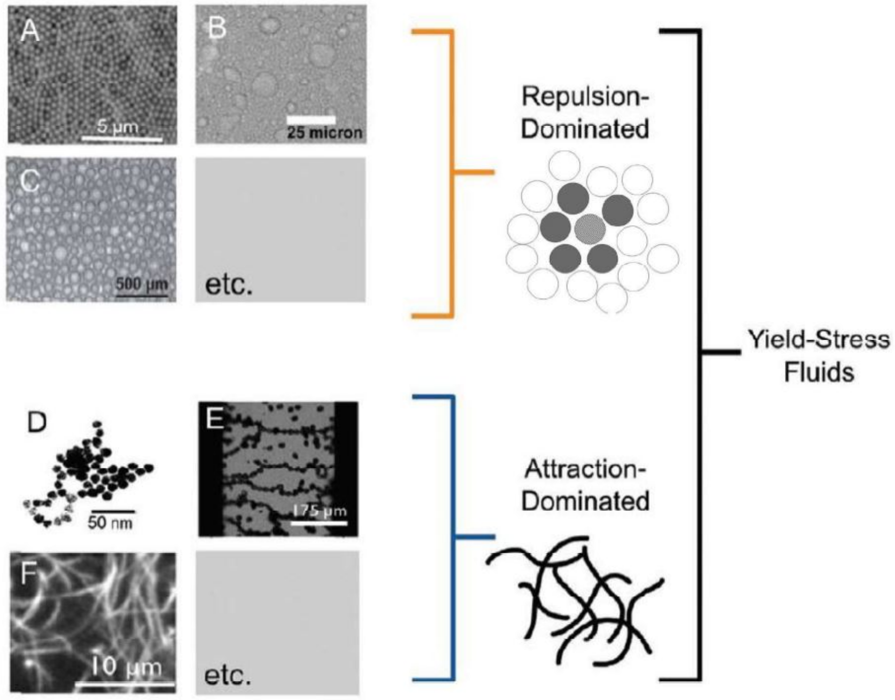

Figure 2.2: Summary of the characteristic yield stress microstructures. Adapted from Nelson et al. 2017 [115] and Mewis et al. 2012 [106]. The yield stress fluids are separated in "repulsion dominated" and "attraction dominated" categories and illustrative pictures are presented for both [115]: A colloidal glasses, B emulsions C foams, D colloidal gel, E electro/magnetorheological fluid, F fiber gel. In the sketch for the repulsion dominated systems [106], the caging notion is illustrated: the grey particle at the center is caged by the surrounding particles in black and white.

Yield stress fluids of attractive particles are often called "gels" [51]. The yield stress is associated to the existence of an attractive three dimensional network. A single particle is binded to its neighboring particles, so that for a single particle to move independently from a theoretical neighbor, the binding energy needs to be overcome. Despite being stuck in a percolating, attractive network, the particles can locally diffuse around their equilibrium position due to Brownian motion [106]. The particle free volume is higher than in the case of crowded suspensions. Examples of yield stress fluids composed of attractive particles are particles gels, polymer gels [115], electro-rheological fluids and magneto-rheological fluids [165]. Liu and Nagel's crowding diagram was adapted by

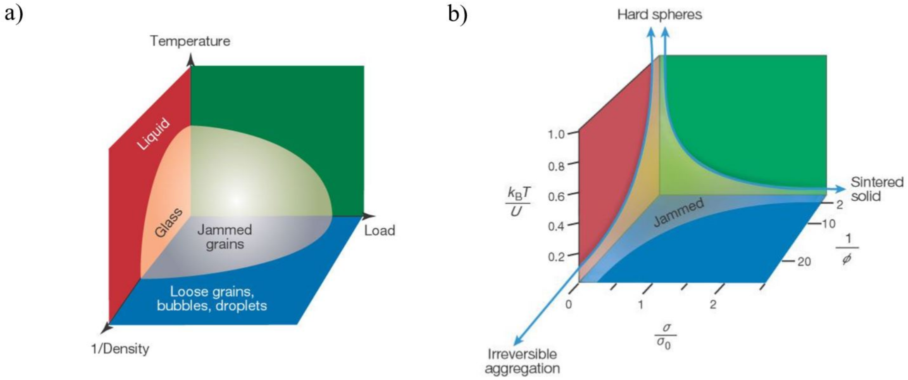

Figure 2.3: a) Jamming diagram for repulsive colloidal spheres (grains, bubbles, droplets etc...). The physical state of suspensions of spheres is mapped as a function of temperature, inverse suspension density and applied load. Inside the clear zone, the grains are jammed. Outside, they can flow past each other. Taken from Trappe et al. 2001 [155]. b) Gelation diagram for attractive colloids. The physical state of the suspension is mapped as a function of the inverse of the scaled attraction energy, the inverse of the volume fraction and the scaled applied stress. Inside the clear zone, the suspension are gelled, outside they have a liquid-like behavior. Taken from Trappe et al. 2001 [155].

Trappe et al. for attractive colloidal suspensions [155], as depicted in fig. 2.3: it summarizes the conditions for obtaining a yield stress fluid starting from attractive particles as a function of the volume fraction ϕ, the attraction energy U, and the applied stress τ. Lastly, it is worth noting that some systems can have both glasses and gels features [115, 19, 116], as both repulsive and attractive interactions coexist on a similar range such as in attractive glasses [87].

2.2 Inclusions suspending abilities

The solid-like properties at rest of yield stress fluids associated to a microscopic structure-bearing network are the reason why such complex fluids can stabilize density mismatched inclusions. In principle inclusions are stable when exactly density matched, however, the situation in which the inclusion is mismatched with the surrounding fluid is more frequent in real life applications. This is the case, for instance, for bubbles in a viscoelastic matrix [83], oil drops dispersed in an aqueous medium [33], or rock or sand aggregates in cement [3].

2.2.1 Predicting stability from macroscopic parameters

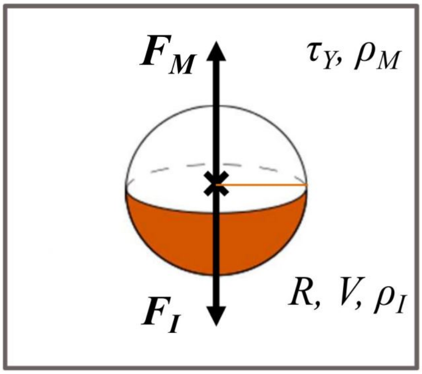

Figure 2.4: Force balance of a spherical inclusion stably immersed in a yield stress fluid. The inclusion, of radius R, volume V and density ρ_{I}, is immersed in a fluid of yield stress τ_{Y} and density ρ_{M}. In this situation, there is a balance between the buoyancy force of the inclusion, $\boldsymbol{F}_{\mathrm{I}}$, and the reaction force exerted by the matrix, $\boldsymbol{F}_{\mathrm{M}}$.

In the case of an inclusion stably suspended in a yield stress fluid, there is a balance between the sedimentation or buoyancy force F_I, and the force exerted by the matrix F_M, as depicted on fig. 2.4. The yield force F_{Y} is defined as the maximum value of F_M and is expressed as the product of the yield stress τ_{Y} of the yield stress fluid with the frontal area S, in orange in fig. 2.4.
A macroscopic dimensionless yield number has been introduced to predict if a given inclusion will settle in a given gel [17]. It predicts spherical inclusions stability on the basis of the yield stress fluid's and the inclusion's macroscopic parameters. The dimensionless yield number is indeed defined as the ratio of the yield force F_Y by the buoyancy force F_I:

$$Y = \frac{\boldsymbol{F}_{\mathrm{Y}}}{\boldsymbol{F}_{\mathrm{I}}} = \frac{S\tau_{\mathrm{Y}}}{\Delta\rho V g} = \frac{2\pi R^2\tau_{\mathrm{Y}}}{\Delta\rho\frac{4}{3}\pi R^3 g} \tag{2.10}$$

with $\Delta\rho$ the density mismatch, V the inclusion volume and g the gravitational constant.

$$Y = 1.5\frac{\tau_{\mathrm{Y}}}{\Delta\rho R g} \tag{2.11}$$

The inclusion is not stabilized in the fluid when the yield stress is too low, the single inclusion too big or density mismatched. That is the case when the yield number is below a critical yield number, see next paragraph. It is worth noting that several similar dimensionless yield numbers coexist in literature, the one aforementioned [17, 51, 149], but also $\mathrm{Y} = 1.5\,\frac{\tau_{\mathrm{Y}}}{\Delta\rho(2R)g}$ [107]. In some references, the value of 3Y is discussed [124, 78]. Its name and notation vary as it is also referred to as yield number [149], stability parameter [78], dimensionless yield stress [51].

The critical yield number for spheres, $\mathbf{Y}_{\text{crit}}$

The critical yield number marks to the onset of the inclusion motion overcoming the yield stress: below this value, the inclusion sediments or rises, according to the sign of the density mismatch. The critical yield number corresponds to the critical values of the triplet $(\tau_{\mathrm{Y}}, \Delta\rho, R)$, in the case of a spherical inclusion. For a specific matrix of yield stress τ_{Y}, the critical yield number is reached for the critical values of the doublet $(\Delta\rho, R)$, as is the case in our experimental work. In the most careful convention, the critical parameters associated to the critical yield number ex: $\Delta\rho$, are written with a "crit" subscript, thus $\Delta\rho_{\text{crit}}$, which is often dropped in literature for the sake of clarity.

The critical yield number value is smaller than unity [78, 107]: this implies that the amplitude of the buoyancy force required to make the inclusion fall is higher than the amplitude of the yield force. This is explained by the fact that sedimentation only starts when the inclusion yields a region of yield stress fluid around it, as shown in fig. 2.7, the inclusion therefore being able to move along the gravity axis. The extent of this critical region depends on the probed yield stress fluid [17, 51] and inclusion parameters [78, 24, 71] as is described in section 2.2.2.

Sphere sedimentation

Mapping the transition between sedimentation and arrested motion of inclusions in yield stress fluids [148, 51] allows the critical yield number to be determined. We now introduce the characteristic numbers and equations associated with the sedimentation of a rigid spherical inclusion in an unbounded matrix, which can be considered as a continuum with respect to the inclusion. The buoyancy force of the inclusion is non-zero when there is a density mismatch with the suspending fluid. The inclusion sediments or rises in the matrix with an average sedimentation speed V_{S} and induces an average shear rate $\dot{\gamma}$. The latter is usually expressed as the ratio of the average sedimentation speed and the diameter of the inclusion [110, 65],

$$\dot{\gamma} = \frac{V_{\mathrm{S}}}{2R}, \tag{2.12}$$

where V_{S} is the terminal speed that is reached after establishment of a steady-state of sedimentation dynamics, averaged over all inclusions, of diameter R.

The absolute stress τ_{I} exerted by the inclusion on the surrounding matrix is then expressed as:

$$\tau_{\mathrm{I}} = \frac{F_{\mathrm{I}}}{S} = \frac{\Delta\rho V g}{S} = \frac{\Delta\rho\frac{4}{3}\Pi R^3 g}{2\Pi R^2} = \frac{2}{3}Rg\Delta\rho, \tag{2.13}$$

where F_{I} is the amplitude of the inclusion buoyancy force exerted on the surface S, V the inclusion volume, $\Delta\rho$ is the density mismatch and g the gravitational constant.

The terminal speed of a spherical inclusion in an unbounded viscous fluid is expressed using the Stokes law:

$$V_{\mathrm{t}} = \frac{2}{9}\frac{\Delta\rho}{\eta_{\mathrm{m}}(\dot{\gamma})}gR^2. \tag{2.14}$$

Here $\eta_{\mathrm{m}}(\dot{\gamma})$ is the shear rate dependent viscosity of the matrix. Using equation. 2.13, the terminal speed can be expressed as a function of the inclusion stress:

$$V_{\mathrm{t}} = \frac{1}{3}\tau_{\mathrm{I}}\frac{R}{\eta_{\mathrm{m}}(\dot{\gamma})}. \tag{2.15}$$

The drag correction factor H [104] is often used in literature on inclusions settling in viscoelastic fluids, to compare experimental speeds with the Stokes law using the zero-shear viscosity $\eta_{\mathrm{m}}(0)$.

$$H = \frac{V_{\mathrm{t}}}{V_{\mathrm{S}}} \tag{2.16}$$

Furthermore, the use of the drag coefficient is commonplace. It is defined as the viscous drag force F_D divided by the characteristic area of the particle s and the kinetic energy per unit volume E_{k}: [82]:

$$C_{\mathrm{d}} = \frac{F_{\mathrm{D}}}{sE_{\mathrm{k}}} \tag{2.17}$$

where F_{D}, the drag force, is equal to the inclusion force at equilibrium, $s = \Pi R^2$ and $E_{\mathrm{k}} = (1/2)\rho_{\mathrm{I}}{V_{\mathrm{S}}}^2$ with ρ_{I} the inclusion density. The drag coefficient thus simplifies as:

$$C_{\mathrm{d}} = \frac{8}{3} R g \frac{\Delta\rho}{\rho_{\mathrm{I}} V^2} \tag{2.18}$$

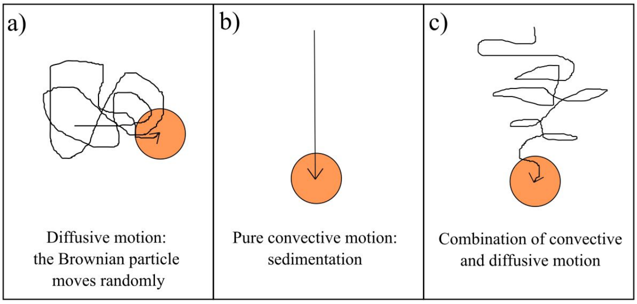

Figure 2.5: Three different trajectories for a spherical inclusion. a) Pure Brownian motion. b) Pure sedimentation motion. c) Combination of Brownian and sedimentation motion.

Generally speaking, the dimensionless numbers relevant to describe viscous sedimentation in a yield stress or shear-thinning dispersions are: the Reynolds number Re, the Deborah number De, the Weissenberg number We and the Bingham number Bn.

The Reynolds number compares the forces due to flow inertia with the viscous forces. For a spherical inclusion of radius R falling at a speed $\mathrm{V_S}$ in a Newtonian fluid, or a fluidized Bingham fluid, it is defined as:

$$Re = \frac{\rho_{\mathrm{S}} V_{\mathrm{S}} R}{\eta_{\mathrm{S}}} \tag{2.19}$$

If the matrix is a power law shear-thinning fluid or a fluidized H-B fluids, Re is defined as:

$$Re = \frac{\rho_{\mathrm{S}} R^{\mathrm{n}} {V_{\mathrm{S}}}^{\text{2-n}}}{k} \tag{2.20}$$

where n is the power law coefficient and k the consistency.

The Deborah number is a dimensionless number of general use, defined as the relaxation time of the system divided by the observation time. A frequent definition is the following:

$$De = \lambda\dot{\gamma} \tag{2.21}$$

where λ is a relaxation time of the system, which can have various origins and $\dot{\gamma}$ can also be attributed to different kind of shear flows.

The Weissenberg number specifically quantifies elastic effects in a system, and is defined as the ratio of elastic forces to viscous force. In steady simple shear flows:

$$We = 2\lambda\dot{\gamma} \tag{2.22}$$

For suspensions of colloidal particles, the Peclet number is the relevant dimensionless quantity, the forces associated to thermal diffusion are compared to the viscous forces. In the case of a spherical inclusion sedimenting in a semi-dilute suspension of colloidal rods, we define the rotational Peclet number as follows [92]:

$$Pe_{\mathrm{r}} = \lambda\dot{\gamma} = \frac{V_{\mathrm{S}}}{2RD_{\mathrm{r}}}. \tag{2.23}$$

where the rotational network relaxation time is defined as $1/D_{\mathrm{r}}$, where D_{r} is an experimentally determined rotational diffusion coefficient associated to rods in the semidilute regime [92].

In the specific case of inclusion sedimentation in yield stress fluids, the Bingham number Bn is used to quantify yield stress effects on sedimentation and compares yield forces with viscous forces. For Bingham fluids:

$$Bn = \frac{\tau_{\mathrm{Y}}}{\eta\dot{\gamma}} \tag{2.24}$$

And for H-B fluids:

$$Bn = \frac{\tau_{\mathrm{Y}}}{k\dot{\gamma}^{\mathrm{n}}} \tag{2.25}$$

where k is the consistency and n the H-B exponent.

The mean square displacement for the inclusion that can be measured experimentally is defined below, for a pure Brownian diffusion as depicted in fig. 2.5 a) then in the case where diffusion and convection coexist, as depicted in fig. 2.5 c). In principle, the mean square displacement in the direction transversal to sedimentation is purely diffusive. It is hence defined as follows [80]:

$$< (\Delta r_{\mathrm{x}})^2 > = 2D_{\mathrm{s,x}}t \tag{2.26}$$

where Δr_{x} is the displacement transversal to the sedimentation direction, $D_{\mathrm{s,x}}$ is the corresponding diffusion constant and t the lag time.

Projected to the sedimentation direction, the mean square displacement of a sedimenting inclusion that undergoes Brownian motion is expressed as such:

$$< (\Delta r_{\mathrm{z}})^2 > = 2D_{\mathrm{s,z}}t + (V_{\mathrm{S}}t)^2 \tag{2.27}$$

where Δr_{z} is now the displacement transversal to the sedimentation direction and $D_{\mathrm{s,z}}$ the corresponding diffusion constant.

2.2.2 Review of theoretical and experimental studies

In this section, the studies on spherical inclusions in yield stress fluids are be presented as a function of the relative value of their yield number as compared to the critical yield number. Two situations are presented. In the first part, "$\mathrm{Y} > \mathrm{Y}_{\text{crit at rest}}$", we introduce studies on inclusions, whose dimensionless yield number in the matrix is higher than the critical yield number, which implies that the inclusions are stable at rest in the matrix. Here one has to distinguish between the properties of yield stress fluids containing density mismatched inclusions, under external shear, "$\mathrm{Y} > \mathrm{Y}_{\text{crit at rest}}$, under shear", and in the absence of external shear, "$\mathrm{Y} > \mathrm{Y}_{\text{crit at rest}}$, in the absence of external shear". In the first case sedimentation of inclusion happens [124] and in the second case the inclusions influence the overall linear and non-linear properties [28, 3, 99] and we showcase both phenomenological laws and experimental works.

In the second part, "$\mathrm{Y} < \mathrm{Y}_{\text{crit at rest}}$", we introduce studies that focused on determining the existence and value of the critical yield value, as well as the shape of the yielded regions. Furthermore, the study of the viscous sedimentation of inclusions inside the yield stress fluid is also detailed. In a first part, the numerical computations that showcased the existence of the macroscopic criterion, as well as help defining the yielded regions surrounding the inclusions are described. Then, the experimental work is detailed, focusing on the inclusions and yield stress fluids properties that influence the value of the critical yield number.

$\mathrm{Y} > \mathrm{Y}_{\text{crit at rest}}$: rheological properties under shear of yield stress fluids containing inclusions

In the case of yield stress fluids containing inclusions that are stably suspended at rest, shear induced sedimentation was reported for flow geometries where the system is sheared in the plane orthogonal to the sedimentation direction. The impossibility to define a stability criterion under shear as all matrices eventually yield is hypothetized for pipe flows [77, 135] then evidenced in simpler shear geometry by studies in coaxial Couette rheometers [61, 124, 126]. As the network is unjammed in the direction perpendicular to shear, inclusions are reported to sediment at all shear intensity, regardless of the microscopic origin of the yield stress, inclusion diameter [123] or static dimensionless yield number [124]. As a consequence, a sedimentation front develops in the Couette cell: in the case of inclusions heavier than the matrix and similarly to what happens in Newtonian fluids, the volume fraction at the upper part of the cell tends to zero, the central part stays at the initial volume fraction and at the bottom

of the cell, the overall inclusion volume fraction increases up to a maximum packing fraction [123, 124].
For dilute inclusion volume fractions, the sedimentation front evolves linearly with time at a speed equal to an individual inclusion's speed. The speed of inclusions sedimenting in sheared yield stress fluids increases with higher shear rates and smaller yield stresses, while a larger inclusion diameter increases the settling speed for non deformable inclusions only [61]. Surfactant stiffened bubbles are also shown to drain quicker than soft bubbles as local viscosity decrease between the inclusions due to strain localization is reported to be more efficient when the inclusion interface is non-deformable [61]. Moreover, drag enhancement effects due to an increased inclusion fraction are less marked than for Newtonian fluids [124], which is explained by the predominance of shear localization effects with regards to inclusion-inclusion interactions [124].
Phenomenological expressions for inclusion sedimentation in sheared yield stress fluids were developped for low [123] and high inclusion fractions [124], in both high Bingham number "plastic" case and in the low Bingham number "viscous" case [123, 124]. It would be interesting to further study whether the onset of sedimentation and the value of sedimentation speeds depend on the usual factors that influence the dimensionless yield number as described in section 2.2.2 and sedimentation speeds in general, such as matrix microstructure and inclusion shape, and roughness.

$\mathbf{Y > Y_{\text{crit at rest}}}$: rheological properties in the absence of external shear of yield stress fluids containing inclusions

In this section, the inclusions are stable at rest in the matrix and the density mismatch is moderate enough to prevent large scale sedimentation during the experiments [124] as described in section 2.2.2. The evolution of linear and non-linear properties when the inclusion volume fraction increases was studied experimentally for solid and deformable spherical particles and a theoretical framework was provided for both situations.

Theory

In the seminal work by Chateau et al. [28], a non-linear micromechanical homogenization method, that is a model that tackles a heterogeneous problem by an homogeneous law, is presented. It quantifies the influence of an increased volume fraction of monodisperse hard spheres on the rheological properties of an H-B fluid. Here it is assumed that the matrix is isotropic, that there are no physicochemical interaction between the matrix and the inclusions, and that a low inclusion fraction rules out shear strain heterogeneities in the matrix [28]. It was shown that solid particles enhance the yield stress fluid's elastic properties for stresses in the linear range [99]. The reduced elastic modulus follows a Krieger-Dougherty (K-D) type of law, similar to what is used to describe the viscosity increase in a viscoelastic fluid [99]:

$$\frac{G'(\phi)}{G'(0)} = g(\phi) = \left(1 - \frac{\phi}{\phi_\mathrm{m}}\right)^{-2.5\phi_\mathrm{m}} \tag{2.28}$$

where $G'(\phi)$ is the elastic modulus of a yield stress fluid loaded with a volume fraction ϕ of inclusions, $G'(0)$ the elastic modulus of the bare yield stress fluid, ϕ_m the maximum packing fraction and $g(\phi)$ the homogenization law.

The reduced yield stress can be expressed as a function of the reduced elastic modulus and is also an increasing function of the inclusion concentration [52, 99, 100]:

$$\tau_\mathrm{C}(\phi) = \tau_\mathrm{C}(0)\sqrt{(1-\phi)g(\phi)} \tag{2.29}$$

where $\tau_\mathrm{C}(\phi)$ is the yield stress of a yield stress fluid loaded with a volume fraction ϕ of inclusions, and $\tau_\mathrm{C}(0)$ the yield stress of the bare yield stress fluid. Lastly, a different homogenization model was developed to describe the decrease of the reduced elastic modulus of an H-B yield stress fluid upon bubbles volume fraction increase [49, 50]. The model accounts for the increase of this trend when bubble deformability increases, characterized by higher capillary numbers, defined as the ratio of the matrix elastic modulus by the capillary pressure. As for the reduced yield stress trend, the homogenization models only take the inclusion fraction as a parameter: one describes a nearly static trend for stiff bubbles [85, 50], and the other describes a decreasing trend for very deformable bubbles [50]. Having introduced the main phenomenological laws in the field, we now discuss the relevant experiments.

Experimental work: $\mathbf{Y > Y_{crit\ at\ rest}}$, no external shear

In this subsection, the key experimental studies dealing with the evolution of linear and non-linear properties of yield stress fluids as a function of their inclusion fraction are first introduced for spherical hard inclusions. Then, the impact of inclusions deformability, mechanical interaction with the matrix, aspect ratio and distribution in the matrix is introduced.

With regards to linear properties, Mahaut et al. report an increase of the reduced elastic modulus for increasing inclusion fractions in the case of H-B yield stress fluids. The experimental results are well described by eq. 2.28 with the maximum packing fraction experimentally fitted to $\phi_\mathrm{m} = 0.57\%$. This is the case irrespective of the microscopic origin of the yield stress [155, 128, 115] and of inclusion size, provided that the inclusion is large enough for the matrix to be considered as a continuum.

There are also cases where an increase in hard or soft inclusion fraction induces a decrease of the reduced elastic modulus [3, 49, 85, 50, 156]. We therefore introduce in this paragraph the distinction between active and passive inclusions, which is frequently used when describing the mechanical properties of soft composite materials, in particular food emulsions [156, 4, 62, 84]. As depicted in fig. 2.6, passive inclusions don't interact mechanically in the sense of an elastic mechanical network with the matrix in opposition to active inclusions. That's the case when there exists an intermediate layer of solvent around a hard inclusion due to geometrical constraints [3] or repulsion at the inclusion surface [31], or due to the presence of an interfacial layer [85]. That implies that the particle network does not touch the inclusion. Under shear, mechanical interactions at the inclusion interface, that is efficient stress transmission, are thus prevented: due to the presence of a mobile layer at the interface of the inclusion, a slip condition applies [50], and most of the gel's stress is dissipated at the inclusion surface. It was noticed experimentally that an increase in the passive inclusion fraction induces a decrease of the elastic modulus for low inclusion fractions [84]. According to section 2.2.2, there exists no generic phenomenological model that describes the influence of passive inclusions fraction. In the specific case of bubbles however, the trend of the reduced elastic modulus as function of both inclusion fraction and interface deformability [85, 49, 50] is well described by the dedicated homogenization law [49, 50]. Eventually, it is worth noting that above a critical passive inclusion fraction, an increase in the reduced elastic modulus is in some cases reported [3, 85, 162]. It is attributed to the formation of an inclusion superstructure.

With regards to yielding properties, an increase of the reduced yield stress upon an increase of the hard spherical inclusion fraction is generally reported [3, 60, 52, 99, 100]. The two publications by Mahaut et al. [99, 100] report a good agreement with eq. 2.29 with $\phi_{\mathrm{m}} = 0.57$ for all yield stress origin, inclusion size [99] and in the presence of thixotropy [100]. In two less generic studies [52, 3], a good correlation with eq. 2.29 is obtained for $\phi_{\mathrm{m}} = 0.6$. Geiker et al. [60] report an increase of the reduced yield stress upon inclusion fraction increase tenfold higher that in the other works, which might come from an overestimation of the yield stress from the H-B fit of the flow curves, while yield stresses deriving from slump tests [52] or step rate tests at constant speed [99] are considered more reliable. Lastly, in the case of inclusion fractions higher than 0.45% [38], the data is well fit by eq. 2.29 with a factor 2.

Shear induced inclusion anisotropy [126], which means that the inclusions acquire an heterogeneous distribution in the yield stress fluid due to shear, was reported both macroscopically thanks to tomography [126] and at level

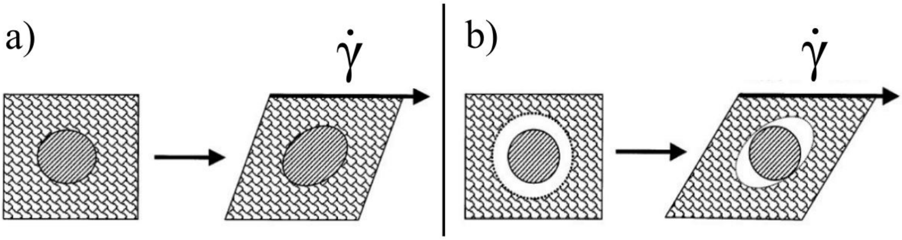

Figure 2.6: a) Active inclusion at rest and under shear, there is a mechanical cohesion between the inclusion and the matrix. b) Passive inclusion at rest and under shear. At rest, there is an intermediate layer, depicted in white, between the matrix and inclusion, either solvent, or interface. Under shear, there is slip at the inclusion interface, energy is dissipated in the mobile intermediate layer. There is no mechanical cohesion between the inclusion and the matrix. Adapted from Chen et al. 1999 [30].

of inclusion pair trajectories [53, 57], evidencing motion out of the velocity gradient plane and thus inducing inclusion distribution heterogeneity. It was shown to influence the inclusion fraction dependent non-linear rheology, as eq. 2.18 fits the experimental data when using a slightly higher maximum packing fraction, $\phi_{\mathrm{m}} = 0.605$, which might explain the results in some aforementioned works [52, 3].

Particle shape also influences non-linear properties as shown by Hafid et al. [69]: when the inclusion aspect ratio increases, the reduced yield stress increase is steeper and higher values are reached. A key point is that the measured maximum packing fraction of bare inclusions decreases when the aspect ratio increases [3]. When inputing these empirical packing fractions in the phenomenological K-D law, eq. 2.29 matches well with experimental data [3].

The last parameter that is discussed in this section is the influence of bubble stiffness on the reduced yield stress trend. For a stiff interface, the yield stress is equal to the yield stress of the matrix [50, 55], which is well described by Kogan et al. homogenization model [85]. An increase [55] is even reported due to physical adsorption of surfactants at the interface, and a dedicated homogenization model was developed. Lastly, a higher deformability of the bubble interface at the yielding point induces a decrease of the yield stress upon an increase in the inclusion fraction [50, 55], Ducloué et al. homogenization law provide with a lower boundary of the decreasing trend [50]. At a critical inclusion fraction, increasing with bubble size, for bubbles which addition is responsible for a static trend of the yield stress, the reduced yield stress increases [85].

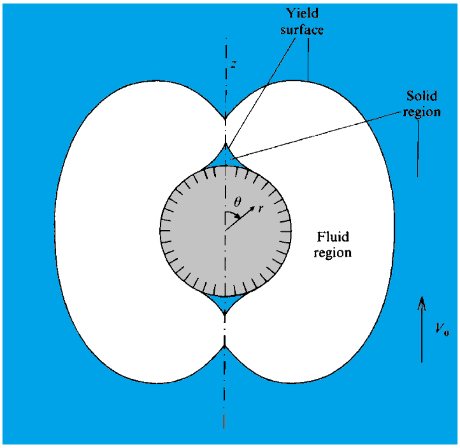

Figure 2.7: Numerical simulation of the yielded region around a smooth hard spherical inclusion sedimenting in a Bingham fluid in the creep limit [17]. The yielded "liquid" region is in white, while the blue zone surrounding it as well as the inclusion's polar cap in blue are unyielded, "solid" regions. Adapted from Beris et al. 1985 [17].

In the next section, we summarize numerical simulations then experimental studies on the trapping and viscous flow of inclusions of yield stress fluids.

$\mathbf{Y < Y_{crit}}$ at rest

Numerical simulations

Beris et al. [17] studied the creeping motion of smooth spheres through unbounded Bingham fluids with finite elements numerical simulations, coupled to the Newton iteration method and using the von Mises yield criterion [124]. They were the first to show that inclusion stability can be predicted using a dimensionless yield number, Y, see eq. 2.11. Moreover they computed the value of 0.143 for the critical yield number [124, 51], see section 2.2.1, which was later experimentally validated by Tabuteau et al. [148]. Fig. 2.7 displays the evidenced yielded region [17], which is axisymmetric with regards to both the gravity axis and to the equatorial plane. Stagnation zones, which are regions of unyielded yield stress fluid inside the yielded region, are located at the sphere poles, in the wake and below the inclusion. An increase in Y induces a shrinkage of the yielded region and an expansion of the polar solid caps, but does not

alter significantly the flow pattern.
Lastly, the drag coefficients for $\mathrm{Y} < \mathrm{Y}_{\mathrm{crit}}$ are displayed on fig. 2.8 a) (ratio 50:1). A significant drag enhancement with regards to the Stokes solution for Newtonian fluids is noticed, even more so as Y gets close to $\mathrm{Y}_{\mathrm{crit}}$.

In the following section, we detail the main parameters influencing the value of the stability criterion, the yielded regions, and the drag coefficient. Interaction effects with walls or neighbors is first tackled, then matrix effects and eventually inclusion parameters such as roughness and shape.

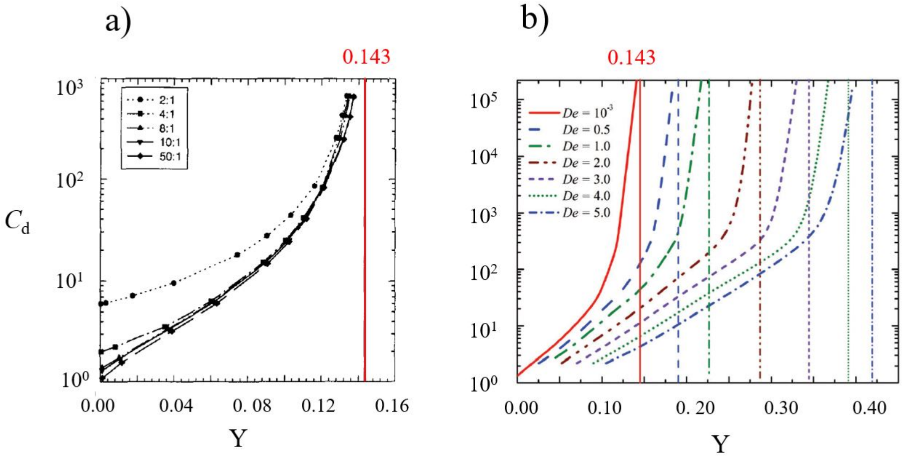

Figure 2.8: Drag coefficient as a function of the dimensionless yield number from finite elements simulations. a) For a bounded Bingham fluid [15] for varying sphere diameter to tube diameter ratios: from the 2:1 benchmark problem to 50:1, which matches unbounded results [17]. Adapted from Blackery et al. 1997. b) Drag coefficient for an inclusion falling in a viscoelastic H-B fluid, expressed as a function of the Deborah (De) number [58]. At low De numbers, elasticity is neglectible and the results agree with Beris simulations [17] for simple Bingham fluids. Taken from Fraggedakis et al. 2016 [58].

The effect of walls or surrounding inclusions on the yielded regions is of high practical relevance. The cylindrically bounded case for creeping spherical inclusions sedimenting along the cylindrical tube symmetry axis was studied both for Bingham [18] and H-B fluids [15], using the Papanastasiou modification in the constitutive equation [15], see section 2.1.2. The stability criterion is unchanged by the presence of walls, however the shape and span of the yielded region are a function of the tube to inclusion diameter ratios. For instance, for high confinement and low Bingham numbers, the yielded region indeed extends to the cylinder walls [18]. In the case of H-B fluids equatorial unyielded regions appear for specific Bn and confinement ratios. Unsurprisingly, the drag coefficients increases with confinement for low Y but all converge towards the same value and eventually diverge to infinity when Y tends towards Y_{crit}, as shown in fig. 2.8 a).

The influence of inclusion fraction is more complex from a computational aspect and was only recently tackled. The yielded regions in the case of inline sedimentation of two inclusions, that is two inclusions sedimenting along the same vertical symmetry axis, was studied by Chaparian et al. [26] and showed that below a critical distance, the yield stress required to hold two identical interacting inclusions is higher than for a single inclusion. For a decreasing inter-inclusion distance, the two yielded regions connect and eventually an unyielded region bridges the two inclusions [26] as depicted in fig. 2.9 a). The study is extended to inline sedimentation of unequal sized inclusion and of three inclusions with different separation sizes, which results in various yielded shapes and heterogeneous settling behavior of the inclusions [26].

The influence of yield stress fluid properties such as elasticity below the yield stress were studied by Fraggedakis et al. [58]. As displayed in fig. 2.8, the critical yield number increases with the Deborah number, which is understood as a delay of inclusion entrapment due to elastic relaxation which implies that higher yield stresses are required to trap a given inclusion. In accordance with this explanation, at fixed Bn number, the yielded regions are reported to expand when elasticity increases. Moreover, elasticity is responsible for the presence of a negative wake, that is local flow in the direction opposite to sedimentation in the inclusions' wake. Contrarily to what was found for purely viscoplastic materials, the yielded regions are therefore assymetric with regards to the equatorial axis and the yielded shape are also different, close to Y_{crit}.

Lastly, we now detail the influence of inclusion properties such as shape and roughness. The inclusion surface roughness, where "rough" implies no-slip condition on the particle, indeed influences inclusion stability [58]. For rough spheres in H-B fluids, Y_{crit} is smaller than 0.143 as the yielded volume is bigger. Moreover, no stagnation cone at the poles is evidenced for rough spheres and the shape of the yielded zone is different.

The influence of inclusion shape was recently studied by Chaparian et al. [24] in 2017 . The so-called "cloaking" effect is introduced: the yielded region of an axisymmetrical inclusion as displayed in fig. 2.9 b), is determined by the dimensions of the unyielded region that surrounds it. Other axisymmetric inclusion of similar unyielded region, an horizontal ellipse of long axis equal to the bat's horizontal spread for instance, or a diamond matching the orientation and dimensions of the unyielded region, will have the same yielded region and critical yield number. This is why the specific shape of the particle is said to be "cloaked".

As a summary, numerical studies proved the existence of a critical yield number, and of complex shaped yielded regions for smooth spherical inclusions. Those properties were shown to be a function of fluids' properties below the yield stress, interaction with walls and particles, and also inclusion shape and roughness. Viscous drag strongly depends on Y, and other parameters such as particle interactions, walls effects.
We now introduce the relevant experimental studies.

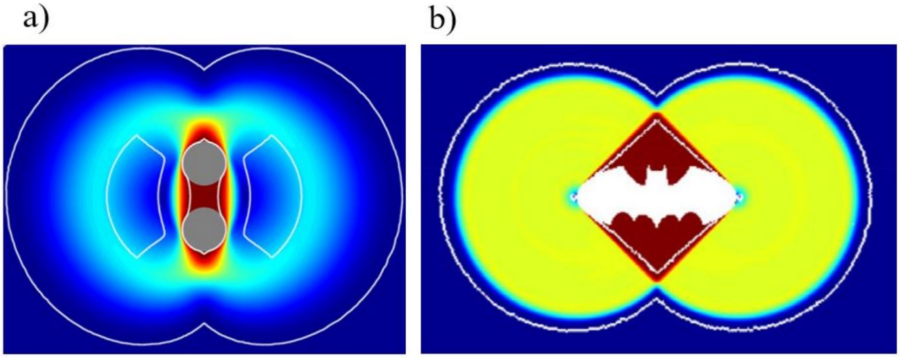

Figure 2.9: Yielded borders in white and velocities colormap for two type of inclusions. The color code correspond to velocity fields where dark blue corresponds to no motion and red is the highest velocity. a) Two spheres settling in the wake in a Bingham fluid. The white line between the inclusions indicates that the inclusions are connected by a plug of unyielded material (although that is not reflected in the color code). Adapted from Chaparian et al. 2018 [26]. b) Axisymmetric bat inclusion. The bat shape is surrounded by a white diamond shape border that contains unyielded material. Adapted from Chaparian et al. 2017 [24].

Experimental work: $\mathbf{Y < Y_{crit}}$ at rest

We first discuss key experimental studies, in relationship with the discussed numerical simulations. Atapattu et al. [6] in 1995 studied spheres sedimenting in Carbopol considered as a H-B fluid, using a laser speckle tracer method to map the flow fields surrounding the spheres. This enabled them to give the first clear experimental proof of existence of the yielded regions, and validate experimentally the predicted yielded shapes [17]. Later, Tabuteau et al. [149] in 2007, studied settling spheres in Carbopol of varying density through direct visualization techniques. He evidenced the existence of a critical density for which inclusion motion is arrested, thereby quantitatively validating the predictions of Beris et al. with respect to the critical dimensionless yield number. Such a finding was validated in later works [107] using a castor oil

fiber suspending fluid.
Using the sphere's terminal velocities, correlation of the drag coefficients as a function of the Reynolds number (Re) and Bn is provided for H-B fluids, similarly to correlations for power law fluids [6, 148, 154]. Although we won't go in details here, theoretical predictions are valid in two of the three studies. Although inclusion shape for instance has an influence on drag coefficients [78], no specific correlation was developed as a function of the parameters that are discussed in the next paragraphs, interface deformation aside [154, 145].
Having introduced these central studies, we now discuss the influence of inclusion shape, roughness, volume fraction and matrix elasticity and microstructure on inclusion stability: the dimensionless yield stress and the yielded region.

The inclusion's shape has been shown to influence the dimensionless yield number, as displayed in fig. 2.10. Magnin et al. [78] described an experimental system according to which particles of different shape and aspect ratio are tied to a rope: the stress exerted by the particle is varied using motors to move the yield stress fluid container along the gravity axis. The plastic drag coefficient is a function of the inclusion's shape, orientation in the fluid, its slenderness and the ratio of the lateral surface over the frontal area. The critical yield number is a simple function of the plastic drag , with coefficients varying with both inclusion shape and orientation. The critical yield number is thus shown to be strongly dependent on the above mentioned parameters, a higher stability seems to be achieved when the frontal area is maximized for a fixed fluid's yield stress and a fixed inclusion volume. For instance it is easier to stabilize a disk than a vertical rod. Those results thus don't match Chaparian et al. [26] simulations as according to those, a horizontal and vertical rod would have the same equivalent sphere and thus the same dimensionless yield number.
The inclusion roughness increases the size of the yielded region and is responsible for lower critical yield numbers [77, 71].

We now discuss the influence of inclusion fraction, as in real systems interparticle interactions are not negligible and would be expected to affect both yielded regions and sedimentation speeds. The influence of the separation length between two inclusions was studied by Merkak et al. [105] in 2007, in Carbopol, both for inclusions in the wake or falling side by side. In the case of inline motion, the inclusions start interacting for distances of four sphere diameter for rough spheres (roughness of approximately 0.25 mm for a diameter of 15 mm [105]) and two spheres diameters for smooth spheres (roughness of 0.01 μm [105]). This interaction range is smaller than in Newtonian fluids, plasticity therefore decreases the interaction range. As for the dimensionless yield number, for a fixed yield stress, yielding two interacting inclusions in the wake is easier than yielding one. The critical yield number indeed gets up to 40% higher when the inclusions separation distance decreases.

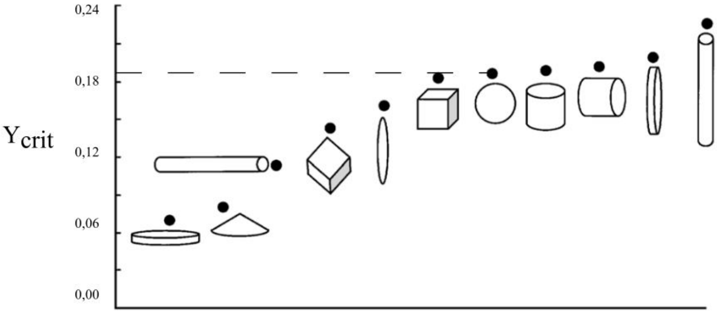

Figure 2.10: Critical yield number as a function of inclusion shape and orientation for adhering inclusions. As a note, the estimate for the spheres critical yield number is indicated by a discontinuous line. It is higher than the 0.143 value in Beris and Tabuteau's works, which is attributed to elastic effects [58]. Adapted from Jossic et al. [78].

In the case of side by side sedimenting inclusions, interaction is neglectible, regardless of the inter-inclusion distance [105]. As a conclusion of this section, we want to stress that in a high inclusion fraction suspension, a single inclusion interacts with more than one inclusion: from Merkak et al. results we can assume that the critical yield number would be only rely on the characteristic distances of inclusions in the wake. The critical yield number for high inclusion fraction would be therefore be reasonably well approximated by the simplified case of a string of particles.

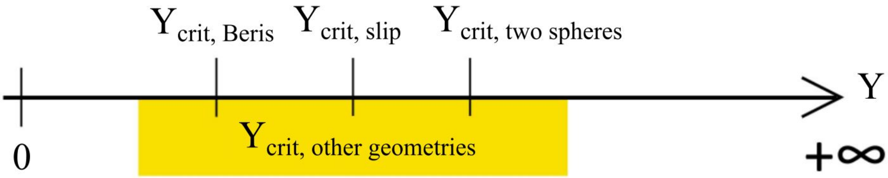

Figure 2.11: Summary of the critical yield numbers as a function of surface properties, shape and the presence of a second inclusion in the wake.

Matrix effects such as elasticity were experimentally evidenced, as negative wake was reported for inclusions settling in Carbopol fluids [134, 71] and a breaking of fore and aft symmetry in the experimental yielded region was first deduced [134] then proved [71]. The agreement with the simulations by Fraggedakis for spheres creeping in viscoelastoplastic fluids [58] is qualitative, however there is a discrepancy between Holenberg et al. yielded region [71] and the simulation based on the von Mises criterion [58]. This is attributed to limitations in the particle image velocimetry technique usually used, and non intrusive technique such as birefringence imaging is recommended although that restrains the study to birefringent samples.

The influence of the matrix's microscopic features is often missing from stability or rheological studies. The suspending yield stress fluid is considered as a continuum, due to the particle to suspending fluid's characteristic size ratio. It was shown however that for fixed inclusion geometry (spherical) and surface properties, the dimensionless yield number is microstructure dependent. At same yield stress values, Carboxymethyl cellulose, which is composed of slender fibers, indeed holds inclusions 3 to 6 times bigger than Carbopol, which is a packed beads microgel [51, 146]. Such an effect is attributed to reorganisation phenomena in the fibers network at moderate concentrations as Song et al. [146] shows that the experimental data converges for those of Carbopol at higher concentrations. Saha et al. [140] also hints at microstructural effects to explain stability against dissolution of bubbles in oleofoams pointing at the small ratio of the inclusion size versus typical fatty crystal size. Mirzaagha et al. experiments in a fibrous structured fluids [107] however match with the continuous approach, which cannot be explained with size arguments in the absence of further information on the fibers size distribution. Lastly, in a recent work, Sgreva et al. [142] show that in a suspensions of packed swollen grains, the critical yield number decreases for sphere to grain diameter ratios below one, which indicates that for this specific system, the continuum assumption only breaks down when the inclusion size is very close to the grain size, which remains to be shown systematically for other systems. A purely macroscopic description could generally speaking be supplemented with studies further investigating the occurence of microstructural effects, and detailing the microstructure dependent extent and shape of the yielded regions, as it is a key tool to understand the general macroscopic picture and the deviation between a macroscopic and a microstructure dependant local yield stress.

Systems with a vanishingly small yield stress, which are not measurable by conventional rheometric techniques are also of interest for our study due to their ability to trap inclusions. Furthermore viscous and entangled fluids that can get structured under shear, or shear thinning systems with a very high zero shear viscosity are able to stabilize creeping inclusions for long times. This short summary of sedimentation of large inclusions in viscoelastic shear-thinning fluids therefore has a threefold interest. First of all, phenomenological models for terminal velocities in viscoelastic fluids allow to assess deviations of experimental creeping flow terminal velocities of the inclusions for a system of interest, and thus to investigate the existence of a yield stress for the considered systems. Second, the understanding of the macroscopic and microscopic phenomena at stake in the sedimentation of inclusions in the shear-thinning yield stress fluid case are enriched by studies of inclusions in shear-thinning viscoelastic liquids. In particular, several viscoelastic shear-thinning fluids among which polymeric liquids and micellar systems, have anisotropic subelements. Their drag enhancement or reduction features may therefore help us understand the reported enhanced trapping of inclusions by yield stress fluids composed of anisotropic subelements [51, 146]: generally speaking viscous reorganisation phenomena are at stake when attractive bonds between anisotropic subunits are broken, especially when such attractive bonds have low magnitude as it is the case for weak gels. Lastly, discussing the parameters for which sedimentation is strongly hindered by viscoelastic fluids is of general interest as depending on the properties of the inclusion and the characteristic times considered, a fluid with only an apparent yield stress with very low inclusion sedimentation times might be satisfying for the desired application, in contexts where the application requires a shear dependant structured matrix rather than a constant high viscosity fluid. In this next chapter, a brief state of the art on sedimentation of slowly sedimenting large inclusions in viscoelastic shear-thinning fluids is thus presented, focusing on the parameters influencing terminal velocities.

2.2.3 Inclusions in viscous, shear thinning fluids

Density mismatched inclusions in viscoelastic fluids at low Reynolds number either have a pure sedimenting behavior and attain a terminal speed, or never reach a terminal speed [110] and instead, oscillate in the direction along the gravity axis [110, 86]. This behavior was attributed to elasticity in the host fluid and microscopic scission and reformation phenomena of the micellar fluid. In the following, we focus on the case where the inclusions purely sediment in the viscoelastic shear thinning fluids.

The experimental terminal velocities, or drag coefficients of large inclusions sedimenting in the creeping flow regime in viscoelastic shear-thinning fluids were less studied than in the Newtonian case and than for inelastic power law fluids [138]. Results diverge from the Stokes law prediction using the zero-shear viscosity, with both drag reduction and enhancement situations (viscosity lower or higher than the zero-shear viscosity) being reported in works at times contradictory [32, 102]. This can be attributed to experimental protocol variations [32] but also varying interplays between elastic effects and shear thinning for each considered experimental systems. The experimental drag correction factor corrected for walls effects [86] therefore generally varies

between 0 to 4 [32, 104, 86]. It is worth noting that the data are rationalized by studying the parameters influencing the drag coefficient or the drag corrective factor. No work uses the alternative approach that consists in adapting the theoretical expression of the viscosity in the Stokes law prediction by separating each viscosity enhancement or reduction factor due to the matrix characteristic elements such as polymer or micellar chains reptation, diffusion. Four main criteria emerge in the related literature to rationalize the drag regime: the characteristic shear rate, using the Reynolds number, the interplay between shear rate and elastic effects, using either the Deborah or the Weissenberg number depending on the system, and lastly walls effects and volume fraction effects as in the Newtonian case. Based on existing drag coefficients-Reynolds numbers experimental datasets, theoretical approximations emerged to predict the settling velocities of inclusions, including in the creeping regime for simple power law, inelastic fluids [138, 82] and viscoelastic power law type fluids [119, 102]. Both Malhotra et al. and Okesanya et al. presents a correlation between elastic and inelastic settling velocities [102] or Reynolds number [119], while computational approaches are presented in the recent work of Garduno et al. [59]. With regards to the role of the system's viscoelasticity, for short relaxation times, drag reduction is generally reported, whereas longer relaxation times are associated to drag enhancement as studied experimentally [104, 102] and computationally [59]. Fig. 2.12 shows however the wealth of different drag coefficient-Weissenberg number relationships for wormlike micelles systems.
Drag reduction is microscopically understood as a shear induced alignment of the fluid's molecules or particles along the sedimentation direction. Drag enhancement, however, is less well understood; simulations [70] and shear profiles mapping around the inclusions in fluids displaying both elastic and shear-thinning fluids characteristics [130] evidenced negative wakes [110, 65] behind inclusions. This phenomenon, which is independant from inclusion deformability [83] is associated to a fluid's increase in viscoelasticity [130] and has an increased geometrical span for high extensional Deborah and Reynolds numbers [157, 110]. Negative wakes are thus used to explain drag increase effects at high Weissenberg number [31, 5], and to explain terminal velocities that sometimes correspond to viscosities that exceed the equivalent zero shear viscosity [59]. In some cases, the opposite effects of shear thinning and extensional thickening cancel each other [104], which explains the general variability of drag behaviors [104]

The influence of the concentration of constitutive elements of the viscoelastic shear-thinning fluid is of interest, as it influences the characteristic relaxation times and the zero-shear viscosity, the relevant literature is however scarce. For micellar systems, Mendoza et al. report that when micellar concentration increases, the critical Weissenberg number above which the transition from drag enhancement to drag reduction happens decreases [104]. Zefeng et al. describes the concentration dependence of drag enhancement for a micellar system, comparing results with the critical shear rate that maps the transition between shear thickening and shear thinning above [160]. Interestingly, drag reduction corresponding to the macroscopic shear-thinning regime is scarcely present. Drag enhancement for low shear rates is associated to the hindrance of settling by the network structure, whereas above the shear rate, is it associated to an settling hindrance due to network elasticity. Furthermore, there exists a critical intermediate concentration for which terminal velocities increase: Zefeng et al. [160] explains the drag enhancement at low micellar concentrations either by the formation of circular micelles at low concentrations or by an initial local increase of concentration front of the inclusions favorized by low concentrations, with a transition to drag reduction at higher concentrations due to higher network entanglement. Quantitative concentration and micellar length dependance of terminal velocities is further reported by Kostrzewa et al. [86], who fit the decrease of terminal velocities with increasing micellar concentrations with a function proportional to the inverse of concentration squared, and attributes the trend to a decrease of the mesh size. The studies also shows that shorter micelles trap less efficiently inclusions, although no explicit relationship between micellar size and terminal velocities enhancement is drawn.

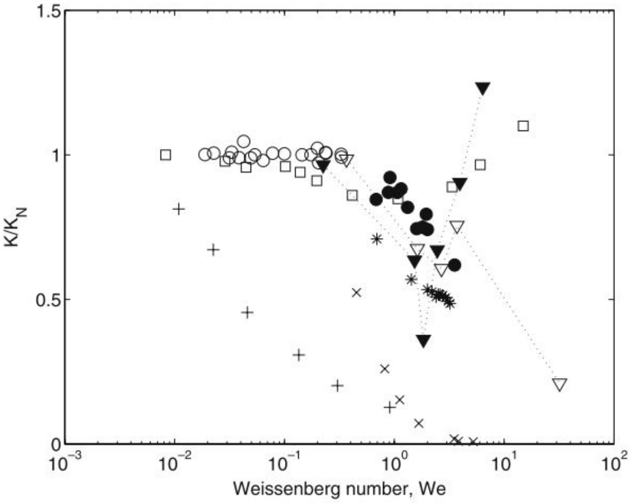

Figure 2.12: For several micellar suspensions, drag coefficient K normalized for wall effects with the coefficient K_N, as a function of the Weissenberg number. Different symbols correspond to different experimental systems, for which the nature of the micellar building block, and electrostatic properties vary. From Mendoza et al. [104].

As for the Newtonian case, the presence of walls interacting with the sedimenting particle induces a decrease of terminal velocities [101, 108]. A wall corrective factor is therefore introduced in the case of cylindrical tubes, when the inclusion falls along the tube long axis [104, 86], or in the case of parallel walls [102]. As an order of magnitude, in the benchmark case of a sphere with a diameter of half the cylinder diameter, the corrective factor is equal to 5.6. Wall effects are however attenuated by elastic effects [102, 147] or an increased shear-thinning [102, 108, 147] as shown by studies on power law fluids.

Lastly, the medium to high inclusion volume fraction case in a viscoelastic shear thinning fluid is of interest as it corresponds to most real-life applications. Terminal velocities therefore decrease above a critical inclusion concentration, as in the Newtonian case. Furthermore, inclusions chaining [157, 150, 112], side by side attraction [67] and cluster aggregation during sedimentation was reported for shear thinning viscoelastic fluids. Inclusions chaining, in particular, happens below a critical distance between closest neighbors [157, 150, 112] that is larger than for Newtonian fluids, and yield stress fluids. While shear thinning memory corridors of reduced viscosity plays a role in aggregation of particles in the wake [41, 130, 112], viscoelasticity is required for spheres to form aggregate or chains in the shear-thinning fluid [130, 73].

As a summary of this state of the art, both stability and rheological properties of inclusions in yield stress fluids were tackled theoretically and experimentally. With regards first to rheological properties of yield stress fluids doped with large hard inclusions, stable at rest, sedimentation of the inclusions under external shear is reported. For low density mismatch, the increase of the reduced linear modulus and yield stress with the inclusion fraction can be described by a K-D law when physical interactions between the matrix and inclusions are neglected. With regards to inclusion stability studies, the value of the critical yield number predicted from numerical simulations was validated experimentally and yielded regions were mapped. The dependence of the dimensionless yield stress and yielded region on inclusion shape, surface roughness, inclusion fraction and matrix effects such as elasticty and microstructural features was described. We concluded this review with detailing drag enhancement and reduction properties of inclusions in structured viscoelastic shear-thinning fluids due to the relevance of such fluids for stabilizing inclusions.

This PhD work tackles separately the topics of microstructure, inclusion fraction and inclusion configuration with regards to the matrix in the context of stability and rheological studies. We used well-defined model colloidal systems in order to provide generic answers to topics relevant for many real systems, and studied jammed systems closer to reality in the last chapter.
In the process of understanding why sparser gels composed of fibers trap

inclusions better than their denser counterparts, the viscous fall of large inclusion in a system of model colloidal rods is studied. Then, the influence of inclusion volume fraction on rheological properties of a model suspension of attractive colloidal spheres is investigated. Lastly, the yield stresses determination through the fall of a shape anisotropic object through foams is carried on, using a model and are more complex foam.
Since our strategy was to use model systems, we detail in the last section of the state of the art the selection criteria and the properties of the chosen model systems.

2.3 Model systems: criteria and selection

In this section, the selection criteria for model systems of large inclusions in yield stress fluids or viscoelastic shear-thinning fluids are detailed. In the first part we focus on the matrix and present the most common model yield stress fluids used to trap inclusions, the selection criteria and the selected matrices. Then, in the second part the selection criteria for inclusions and the selected inclusion type for each specific study are detailed.

2.3.1 Matrix selection

Experimental model systems: state of the art

There are few available experimental model systems to study the stability or the influence on rheological properties of inclusions in yield stress fluids. Carbopol yield stress fluids, made from crowded microspheres, are the most extensively used matrices [148, 6, 134] as model simple H-B fluid. However recent works [71] evidenced elastic effects above the the yield stress. Clays such as laponite [7, 76] are also used [130, 65]. Laponite suspensions are made from attractive clay platelets, and have aging effects well described by descriptive laws [130]. Their batch to batch reproducibility can however be a limitation for systematic studies. Carboxylmethylcellulose [51, 146], composed of attractive cellulose fibers is also sometimes used.
The selection criteria for the matrix are now detailed.

Model systems: selection criteria

We targeted matrices that would help understanding the possible influence on the critical yield number of the fluid's reorganization at the particle level

[51, 146]. We therefore looked for systems composed of well characterized colloidal particles. Those systems are of interest since colloids are ubiquitous building blocks for yield stress or highly shear-thinning dispersions, and that model colloidal particles which physics are well understood, are tool to provide generic answers to the stability and rheology questions introduced.
We looked specifically for systems composed of anisotropic particles to show the influence of anisotropy on inclusion trapping [51, 145, 146] and systems composed of isotropic particles to provide with a reference system.
From the point of view of rheological properties, we selected fluids with known linear and non-linear properties when possible and ideally with a measurable yield stress. We were also interested in yield stress fluids with sufficient partial reversibility, that is a partial recovery of the elastic modulus or the yield stress following yielding events. That is promoted by an intermediate magnitude of interactions between particles or by high amplitude yielding protocols [109].
From the microscopic imaging standpoint, a requirement is that the inclusions can be imaged in the matrix. When considering conventional imaging techniques, this restricts the choice to transparent enough matrices. The use of optical coherence tomography could be considered in further works for rheologically relevant, although opaque matrices. In addition, we chose matrices composed of micrometer sized constitutive particles to pave the way for potential imaging at the single particle level in further studies.

Selected model systems

The selected model systems are: fd and pf1 bacteriophages suspensions and a depletion gel composed of attractive PMMA spheres. We explain in the following paragraphs the motivations for choosing each system, as well as further details on the system's physics. A non-colloidal model jammed system, was used in the third chapter, milk foams and is therefore described in ch. 5 and complex factors are discussed.

Model system composed of anisotropic particles

We focused our search on model systems composed of the simplest anisotropic particles: suspensions of colloidal rods. The Tobbaco Mosaic virus [120], silica rods [168, 40] were used in previous studies, and more recently hollow polymer rods of small aspect ratio are used as model systems [23, 56]. Fd and pf1 virus bacteriophage [43] are however, the best fit for this study, as is explained below. Their most important feature is that they are monodisperse in length and thickness. They have a high aspect ratio and are relatively stiff. The colloidal rods can be produced in high quantities and are density matched with their dispersing solvent. This provides an exact batch to batch reproducibility of

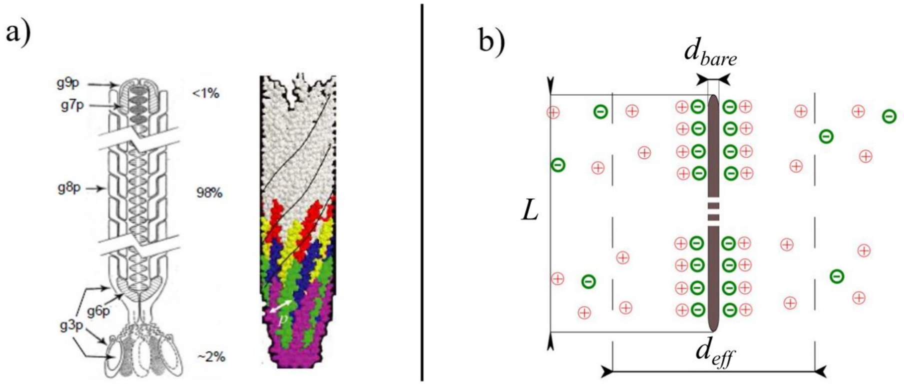

Figure 2.13: a) Structure of fd virus: a DNA strand at the middle is covered by coat proteins: g3p, g6p, etc...Proteins functional groups can be used to graft chemicals on the surface of fd virus, and the overall charge of the biological colloidal rods is negative. b) Sketch of a charged fd rod of length L and diameter d_{bare} and effective diameter d_{eff} in an ionic solvent.

the samples and allows for a systematic study of sedimentation as a function of anisotropic particles concentration. Structurally speaking, the rods are composed of a DNA strand coated with proteins, see fig. 2.13 a). This negatively charged surface allows for polymer or fluorescent molecules grafting. The interaction between the rods can be described by the DLVO theory [27], which accounts for the interactions between charged colloids in an ionic solvent, making the sum of a Van der Waals and a double layer potential. The rods have an effective diameter larger than the bare rods diameter as sketched in fig. 2.13 b), due to the presence of negative charges at the rods surface. The effective diameter which can be tuned by ionic strength, where higher ionic strength results in a smaller effective diameter, due to partial screening of the negative charges. The rods can undergo transitions to a cascade of liquid crystalline phases [63], see fig. 2.14. In isotropic suspensions of rods there is neither orientational nor positional order, the rods' directions and positions are random. In nematic suspensions of rods, there is orientational order but no positional order. The isotropic-nematic transition of charged rods is well described by Onsager's theory for hard rods [121], and can be tuned by the ionic strength [64] and by grafting with polymers, see fig. 2.14, for instance to synthesize model systems of attractive anisotropic particles [166, 136].

Fd virus and pf1 flow curves display a strong shear-thinning behavior at moderate concentrations (<1 wt %), the shear rate dependant viscosity is well described by Lang et al. modification to the Doi-Edwards-Kuzuu theory [93]. The zero-shear viscosity expression can be found in ch. 3. As further explained in ch. 3, the effect of electrostatic interactions can be neglected in the expression of the viscosity of the suspension at zero shear. Fd and pf1 solutions are transparent, which allows for imaging of inclusions in fd solutions. The dimensions guarantee that they can be imaged at the single particle level [2, 64].

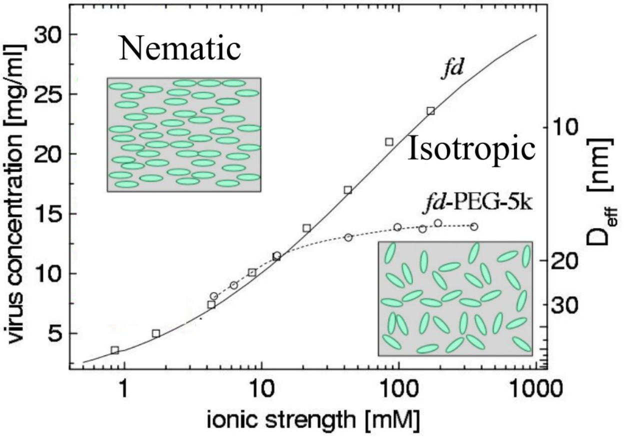

Figure 2.14: Phase diagram of fd virus as a function of concentration, ionic strength, and grafting of PEG polymer. The sketches illustrate the phases' characteristics, and for illustrational purpose the aspect ratio is smaller than for fd. For high concentrations and ionic strengths, the colloidal rods are in the nematic phase. Below the experimental points, where the line is a guide for the eye, the colloidal rods are in the isotropic phase. The phase diagram is adapted from Grelet et al. [64], and the rods sketches from Stephen Lower's work, http://chemwiki.ucdavis.edu/.

Model system composed of attractive colloidal spheres

We looked for gels composed of attractive spherical colloidal particles. Two strategies exist to induce attraction between colloidal particles: one is the addition of non-adsorbing linear polymer chains, responsible for depletion attractive interactions between the colloids [122, 88]. The other possibility is the grafting of targeted polymers at the surface of the colloids: stimuli such as temperature in the case of poly(N-isopropylacrylamide) can switch on low polymer affinity with the solvent, therefore inducing attractions [47].

We chose depletion gels of Poly(Methyl Methacrylate) (PMMA) microspheres as the linear and non-linear rheological properties were extensively studied [87, 90]. The commercially available PMMA spheres are monodisperse and solvent matched. The gels are therefore stable against gravity and their strength

can be tuned by both the colloidal volume fraction [90] and the depletion potential [94]. Such parameters are in favour of a detailed rheological study of depletion gels doped with inclusions. In the following, the depletion interactions between the colloids are defined, then key rheological and optical properties are detailed.
Fig. 2.15 illustrates the attraction between two colloids induced by coils of linear non-adsorbing polymers. The coils centers cannot enter a corona around the sphere of height equal to the coil radius, the corona is thus a "depletion" zone. Below a critical inter-colloid distance, the colloids depletion zones overlap and as a consequence no coil can enter the overlap zone. An imbalance in osmotic pressure is hence created between the coil free overlap volume between the spheres and the rest of the colloids surface on which coils collide. This induces an attraction potential between the colloids, strong enough to overcome electrostatic repulsive interactions. The attraction potential from the classic Asakura and Oosawa law is given by the following expression [122]:

$$\frac{U_{\mathrm{dep}}(r)}{k_{\mathrm{B}}T} = \begin{cases} +\infty & r \leq 2R \\ -\frac{P}{k_{\mathrm{B}}\cdot T} V_{\mathrm{overlap}}(r) & 2R < r \leq 2R(1+q_{\mathrm{s}}) \\ 0 & r > 2R(1+q_{\mathrm{s}}) \end{cases} \tag{2.30}$$

where $U_{\mathrm{dep}}(r)$ is the Asakura and Oosawa potential, r is the distance between the spheres centers, R is the radius of the sphere and $q_{\mathrm{s}} = r/R$ the distance between the spheres centers scaled by the radius of the sphere. k_{B} is the Boltzmann constant, T the temperature, P the polymer pressure and $V_{\mathrm{overlap}}(r)$ the overlap volume. Further details on the Asakura and Oosawa interaction potential can be found in Koumakis' PhD thesis [91].

At moderate PMMA colloids volume fractions, $\phi_{\mathrm{col}} \in$ [0.2;0.4], a transient percolated network is formed, the gels display measurable yield stresses and behave as H-B fluids. Low volume fraction gels form more heterogeneous, weaker structures and are prone to slip at low Peclet numbers [9]. That happens when there is a solvent "slip" layer between the gel and the rheometer geometry; in the absence of adherence, the applied stress cannot be efficiently transmitted from the geometry to the gel. Slip therefore needs to be calibrated, and roughened geometries used in order to perform reliable rheological experiments. A characteristic feature of the considered gels is that they yield in two steps, as displayed in fig. 2.16, which is attributed to intercluster bonds breakage followed by cluster breakage. The gels can be rejuvenated upon application of high shear protocols [88].

Imaging of inclusions suspended in these suspensions is also possible, as the suspensions are only moderately opaque. Additionally, commercial fluorescently labelled PMMA colloids can be used for rheo-imaging purposes [88].

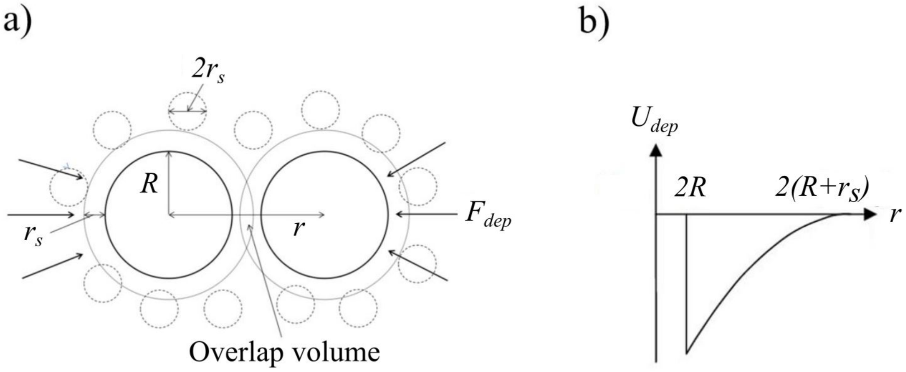

Figure 2.15: a) Sketch for the depletion interaction induced by polymer coil of radius r_S around two colloids or radius R separated by a distance r. Adapted from Guu [68]. b) Depletion potential as a function of the distance r between the two colloids. Adapted from Koumakis [91].

2.3.2 Non-Brownian inclusions

Criteria

Hard sphere inclusions were used in this study as it is the simplest choice for inclusions from both theoretical and experimental point of view. Bubbles and drops in yield stress fluids or viscoelastic shear thinning fluids are indeed commonplace in literature and applications, as already mentioned but are however more complex to deal with than the hard sphere counterpart due to their deformability, and potential rupture under shear. As detailed in section 2.2.2 some "hard inclusions" results can be applied to non-deformable soft inclusions.

The spherical inclusions were selected according to the following criteria with respect to size, density and refractive index:

a) The size ratio $2R/l$ of the inclusion diameter with regards to the suspension's characteristic length, as depicted in fig. 2.17 , should be big enough for the matrix to be considered as a continuum. Since we however want to determine whether microstructural effects matter, $2R/l$ should also be small enough to increase potential sensitivity to microstructural effects [142].

b) The inclusion diameter $2R$ can thus be as small as 20-10 µm with regards to the size of the constitutive particles of the selected suspending fluids, which is

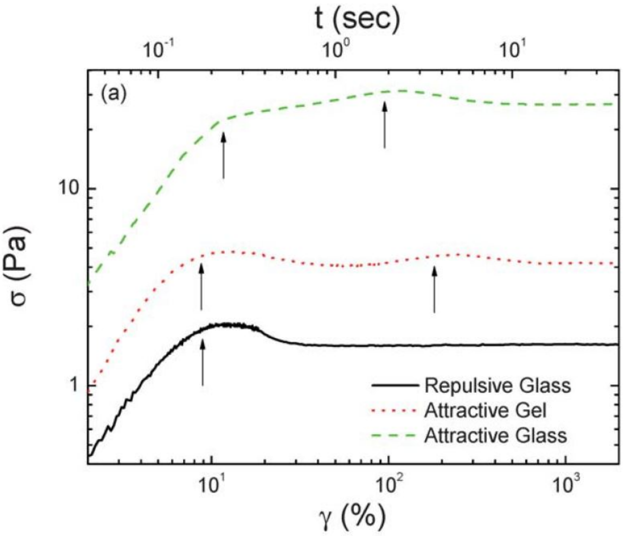

Figure 2.16: Two step yielding of an attractive PMMA colloids depletion gel. The stress first increases elastically when the stress increases, until a stress overshoot peak is reached, which marks the onset of plastic deformation. For higher strains, a second stress overshoot is reached. The graphs on glasses and attractive glasses also display stress overshoot peaks which are a signature of structural yielding. From Koumakis et al. 2011 [88].

low with regards to previous studies [6, 148]. Those diameter values allow the use of cone plate geometries to perform rheological experiments, which choice is motivated by their homogeneous shear rate in the gap.

d) The density difference between the inclusion and the matrix for each system is chosen according to the goal of the study: assessing the existence of a yield stress in ch. 3 , having stable inclusions at rest and under shear in a gelled matrix in ch. 4 , determining the yield stress fluid in ch. 5.

c) For imaging purposes, the inclusions should have a sufficient contrast with the matrix.

Chosen systems

Extensive information on the selected inclusions can be found in the dedicated "materials" section of each results chapter. We however summarize here some key points. In ch. 3, commercial polystyrene spherical inclusions are used. The

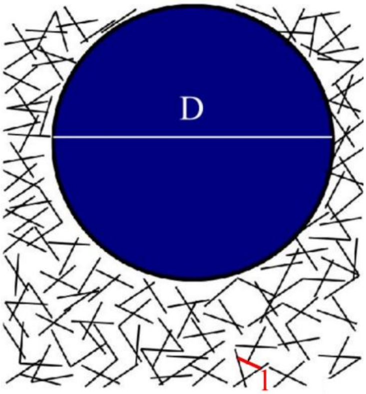

Figure 2.17: Characteristic features: inclusion of diameter $2R$ in a background composed of anisotropic particles (not to scale) of characteristic dimension l.

inclusions have a mean diameter of 10.0 μm, the $2R/l$ ratio using the mesh size at the lowest rod concentration as the characteristic length for the matrix, is thus ranging from 17 to 50. The density mismatch is small in order to study sedimentation in the creep range, and assess the potential existence of a yield stress. The inclusions are black and are easy to image in the biological rods suspensions.

In ch. 4, 20 μm commercial glass spheres are used. The $2R/l$ ratio is of 25, where l is the colloids size. The density mismatch is small in order to limit shear induced sedimentation [124]. The inclusions are transparent but can be well resolved in the gels.

In ch. 5, custom disk-shaped inclusions are designed 5, with $2R/l = 67$ where l is the bubble size. The density mismatch is sufficient to observe disk sedimentation through the foam. The disks cannot be imaged directly in the foam, however the black color allow a good visualization when looking from above.

Chapter 3

Stability of beads in suspensions of rod-like viruses

3.1 Introduction

Studies on the stability and rheological studies of inclusions in yield stress fluids mainly consider the macroscopic yield stress [148, 28]. As we pointed out in section 2.2.2, recent studies evidenced, however, that a matrix composed of anisotropic nanofibers can trap heavier inclusions than a Carbopol suspension, even though both fluids had the same yield stress [51, 146, 145]. This suggests that it is a prerequisite to have a full understanding of the interplay between microscopic changes in the material surrounding the inclusion [88] and the sedimentation force exerted by the inclusion [17, 71], in order to fully understand the yielding process. Furthermore, as also pointed out in section 2.2.3, the sedimentation of inclusions in viscoelastic shear-thinning fluids is commonly described using macroscopic drag coefficients [32, 104]. Both drag enhancement and reduction are reported as a function of the fluids elastic properties and linear macromolecule concentration [104, 86, 161, 160] thus underlying the need to understand macromolecule level reorganization mechanisms.

We report in this chapter an experimental study of sedimentation speeds of large non-interacting spherical inclusions sedimenting in a suspension composed of rod-like viruses, which can be considered as quasi-ideal colloidal rods. We show that using colloidal rods as host medium facilitates comparison between theory and experiments, as the rheological behavior of rods suspensions is by now well described by theory [93]. Although in principle these systems do not show a yielding behavior, the zero-shear viscosity is strongly dependent on the length and concentration of the rods, so that a yielding-like behavior of inclusions in highly concentrated dispersions of anisotropic particles cannot be excluded. Sedimentation studies of inclusions in yield stress fluids composed of anisotropic particles were performed on cellulose suspensions [51, 145, 146], castor oil colloidal fibers in a surfactant suspension [107], laponite suspensions [65, 130], viscoelastic polysaccharide solutions [157, 113] and wormlike micellar fluids [31, 110, 160, 86, 164, 161]. The latter do not possess true yield stresses, but only an apparent yield stress, see section 2.1.1, when excited above the characteristic relaxation time of the matrix. Characteristic features of inclusions falling in shear-thinning fluids were evidenced, as detailed in section 2.2.3. For high extensional Deborah numbers, spheres and bubbles are found never to reach a terminal speed and oscillate in the direction along the gravity axis for high extensional Deborah numbers [110, 86, 161], when the system has only one relaxation mode [161]. In the pure sedimentation case, both drag reduction and enhancement as compared to the Stokes law prediction using the zero-shear viscosity was reported [32, 104], depending on the Reynolds [119] and the Weissenberg or Deborah number [104]. For several of those shear-thinning fluids, negative wake [110, 65], i.e. local flow in the direction opposite to sedimentation in the inclusions' wake, was reported, which is among possible explanations for drag enhancement [104]. It is associated to a fluid's increase in visco-elasticity [130] and has an increased geometrical span for high extensional Deborah and Reynolds numbers [157, 110]. In the case of wormlike micelles, an increasing concentration of these anisotropic particles shifts the transition between drag reduction and enhancement to lower Weissenberg values [104]. Terminal velocities for wormlike micelles [86] generally decrease with an increased concentration similarly to what is reported for stiff fibers [107], however for flexible micelles, a jump in velocities is reported [161, 160]. This is explained by a transition between a semi-dilute state where restructuring and densification is favored [160] similarly to what was recently imaged for cellulose fibers [146, 145] to an entangled state, which favours shear alignment [160]. The length of anisotropic particles was indirectly shown to cause a decrease in terminal speeds [86], but a quantification and theoretical understanding is missing. Additionally, inclusions chaining was reported for shear-thinning viscoelastic fluids such as xanthan, below a critical distance between closest neighbours [157, 150].

Although these studies exemplify the effect of anisotropy in the microstructure, they do not allow for a direct link with the relaxation process of the single anisotropic particles, as the studied systems were polydisperse and relatively flexible. The scope of our study is to stay in the creeping motion regime for non-interacting inclusions at Reynolds numbers lower than 10^{-6}. For the model systems considered, only a classical monotonic sedimentation behavior is expected, excluding negative wake, oscillatory settling, and particles' chaining effects. We consider a model composed of the simplest anisotropic particles: suspensions of slender colloidal rods. We use fd and pf1 as model systems, see also section 2.3. Fd virus has been used earlier to study the dynamics of relatively small inclusions, that is, smaller than the length of the virus [80, 81]. For these inclusions sedimentation effects are not present, and the fd matrix cannot be considered as a continuum. These studies show that diffusion is already strongly hindered for relatively small inclusions especially when the rod concentration increases. Here we use a large enough ratio of the inclusion size to the matrix's constitutive particle length, such that the dispersed rods can be considered as a continuous matrix. Moreover, we work at very low volume fractions of inclusions, as self assembly of colloidal inclusions due to depletion interaction induced by fd virus, has been reported [68], and could thus also appear for larger inclusions.

In the following, the dependence of the sedimentation speed on inclusion stress is investigated in the semi-dilute regime for two different rod lengths at least five times smaller than the inclusions. The targeted question we ask is whether a network of ideal rods possesses an apparent yield stress behavior, which would arrest sedimentation at low inclusion stress, and whether the sedimentation speed can be understood on the base of the known rheological behavior of the host system.

3.2 Theory

In this theory section, we introduce the equation for the sedimentation of an inclusion in creeping flow conditions for a matrix that is a colloidal suspension of rods. In Newtonian fluids, the viscosity η_{m} is a constant. However, in non-Newtonian fluids $\eta_{\mathrm{m}}(\dot{\gamma})$ can strongly depend on the shear rate. In the case of semidilute colloidal rods, as depicted in fig. 3.1 b), the viscosity is constant for low shear rates, then steeply decreases with increasing shear rate [93] as shown in fig. 3.2.

For the stresses used in this work, the resulting sedimentation rates are so low that we only need to take the zero-shear viscosity into consideration, as is shown later. The zero-shear viscosity strongly depends on concentration as well as length, as has been recently shown for fd and pf1 [93]. It can be derived from the Doi-Edwards theory and can thus be quantitatively predicted as [93]:

$$\eta_{\mathrm{m}} = \eta_{\mathrm{S}} + \frac{\nu k_{\mathrm{B}} T}{30 {D_{\mathrm{r}}}^{0}} + \frac{\nu k_{\mathrm{B}} T}{10 \overline{D_{\mathrm{r}}}}, \tag{3.1}$$

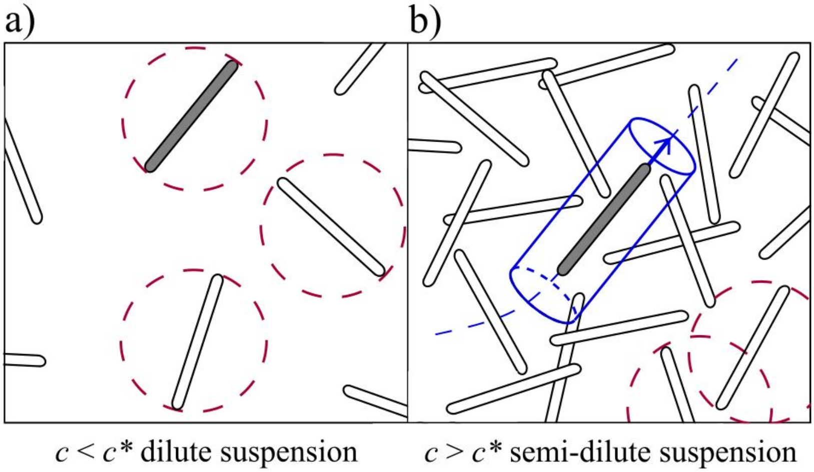

Figure 3.1: Sketches of dispersed colloidal rods in two concentration ranges, which affects the viscosity of the dispersion. On the left, rods are so dilute that they can freely rotate, where the tips of the rods describe a sphere of diameter equal to the rod length, which is the rod's excluded volume. In the dilute state, these sphere do not overlap, $c < c*$, and the associated viscosity is defined as the sum of the solvent viscosity and the viscosity associated with the rotational diffusion of each rod inside the excluded volume. On the right, the concentration is so high that the spheres overlap, so $c > c*$. According to the tube model [44], a single rod diffuses out of a confining tube formed by the surrounding rods, which size is a function of the rods concentration. The viscosity in this semidilute state is defined as the sum of the solvent viscosity, the viscosity associated to rotational diffusion in the dilute state and a term taking into account the concentration dependant tube reptation.

with η_S the solvent viscosity, ν the number density, k_B the Boltzmann constant, T is the temperature. ${D_\mathrm{r}}^0$ is the rotational diffusion coefficient in the dilute case ${D_\mathrm{r}}^0 = 3k_\mathrm{B}Tln(\frac{L}{2d_\mathrm{bare}})/\pi\eta_\mathrm{S}L^3$. L and d are the length and diameter of the rod. $\overline{D_\mathrm{r}}$ is a modified diffusion coefficient, which accounts for the tube reptation dynamics: $\overline{D_\mathrm{r}} = A{D_\mathrm{r}}^0(\nu L^3)^{-2}$. Here ν is the colloidal rods' number density, η_S the solvent viscosity and A a constant.

The first term in eq. 3.1 corresponds to the contribution of the solvent viscosity and the second term is the contribution of rotational diffusion to the viscosity for a non-interacting rod, their sum is the viscosity of a rod suspension as in the dilute case, as on fig. 3.1 a). The third term takes into account the constrained movement of a colloidal rod in the semidilute case. Its expression is similar

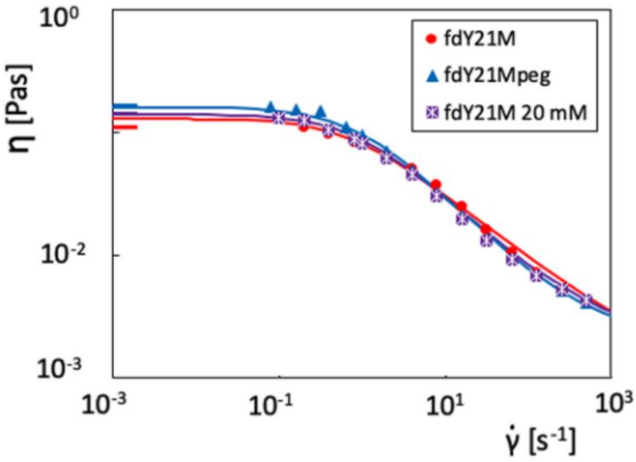

Figure 3.2: Viscosity as a function of shear rate for fd virus Y21m bare, grafted with PEG polymers at an ionic strength of 100 mM and Y21m bare at 10 mM (20 mM Tris), at a concentration of $c = 6.8$ mg/mL. The marks on the ordinate axis are theoretical calculations for the zero-shear viscosity, as detailed in eq. 3.1. Adapted from Lang et al. [93].

to the second term, however a modified diffusion coefficient is used, $\overline{D_\mathrm{r}}$. The sum of the three viscosity terms is the viscosity of a rod suspension as in the semidilute case, as on fig. 3.1 b). After replacing the diffusion coefficient by their expression as a function of L and D, eq. 3.1 now reads

$$\eta_\mathrm{m} = \eta_\mathrm{S}\left[1 + \nu\frac{\pi L^3}{90ln(\frac{L}{2d_\mathrm{bare}})} + \nu^3\frac{\pi L^9}{30Aln(\frac{L}{2d_\mathrm{bare}})}\right]. \tag{3.2}$$

We see a dependence of the zero-shear viscosity with the number density and thus, with rod concentration. One can also note the strong dependence on the rod length.

Using the zero-shear viscosity from the Doi-Edwards theory in the Stokes terminal speed expression, a predictive expression for the inclusion's terminal speed can be derived. This is further referred to as the Stokes-Doi-Edwards (SDE) prediction:

$$V_\mathrm{S}(\nu) = \frac{1}{3}\tau_\mathrm{I}\frac{R}{\eta_\mathrm{S}\left[1 + \nu\frac{\pi L^3}{90ln(\frac{L}{2d_\mathrm{bare}})} + \nu^3\frac{\pi L^9}{30Aln(\frac{L}{2d_\mathrm{bare}})}\right]}. \tag{3.3}$$

Terminal speeds are scaled with the terminal speeds of the inclusions when rods concentration c is equal to zero:

$$\frac{V_S(\nu)}{V_S(\nu=0)} = \frac{\eta_{\mathrm{S}}}{\eta_{\mathrm{m}}} = \frac{1}{\left[1+\nu\frac{\pi L^3}{90ln(\frac{L}{2d_{\mathrm{bare}}})}+\nu^3\frac{\pi L^9}{30Aln(\frac{L}{2d_{\mathrm{bare}}})}\right]} \tag{3.4}$$

This expression is used to compare with the actual data in the following. Note that replacing the diameter by the effective diameter in the expression for the zero-shear viscosity expression, thus taking into account the electrostatic interactions, does not modify significantly the zero-shear viscosity [93].

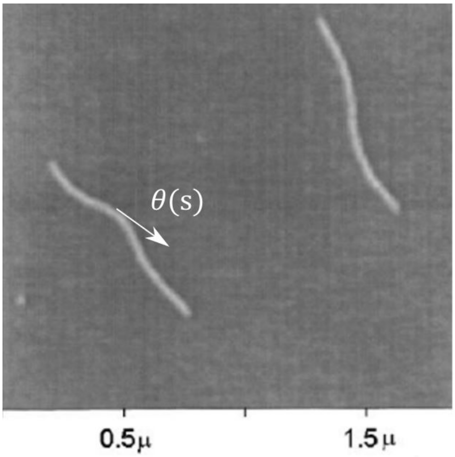

Figure 3.3: AFM picture of fd virus [74]. The contour length is the length of the fully stretched virus [14], while the persistence length is directly proportional to the rod's bending rigidity [151, 14] and is calculated using the function $\theta(s)$ represented on the picture, where s is the position around the contour length and $\theta(s)$ the orientation of the tangent at this position [14].

3.3 Materials

3.3.1 Sedimentation experiments

Rods suspension

Suspensions of fd wild type (fd virus) and pf1 bacteriophages were prepared at the Forschungszentrum Jülich (FZJ). Fd and pf1 viruses are rod-like colloidal particles composed of a DNA single strand coated with a protein layer. They are negatively charged in the dispersing solvent at a pH of 8.15 and an ionic strength of 10 mM. Fd virus, depicted on fig. 3.3, has a molecular weight of $M_\mathrm{W} = 1.64 \times 10^7$ g/mol, a contour length [151] of $L = 880$ nm, a persistence length [151] of $L_\mathrm{P} = 2.2$ μm and a diameter of $d_\mathrm{bare} = 6.6$ nm. The preparations steps are described elsewhere [80]. Pf1 has a molecular weight of $M_\mathrm{W} = 3.75 \times 10^7$ g/mol, a contour length of $L = 2$ μm, a persistence length of $L_\mathrm{P} = 2.2$ μm and a diameter $d_\mathrm{bare} = 6.6$ nm. Protease free pf1 phage for NMR analysis were bought from Asla Biotech, Latvia.

The virus particles were dispersed in a 20 mM tris-HCl buffer at pH 8.15, which corresponds to an ionic strength of 10 mM. We use here mass concentration, which is linked to number densities by $c = \nu M_\mathrm{w}/N_\mathrm{a}$ and also scaling with the overlap concentration $c^* = 3M_\mathrm{w}/4\pi N_\mathrm{a}(\frac{L}{2})^3$ see also fig. 3.1, which is 0.076 mg/ml for fd and 0.013 mg/ml for pf1. We focus on semidilute suspensions of rods between $10 \times c^*$ and the isotropic-nematic transition: from 1 mg/ml to 9 mg/ml for fd virus and from 0.1 mg/ml to 3 mg/ml for pf1. Virus concentrations were determined by UV-visible spectrometry using a Varian Cary® 50 UV-Vis Spectrophotometer, and NanoDrop 2000/2000c Spectrophotometer, Thermo Scientific. The concentration was determined from the absorption peaks in the UV-visible, after substracting the background from the solvent, and using the Beer-Lambert law at the wavelength of 269 nm: $c(269) = A(269)/\epsilon_{269} \cdot e$, where $c(269)$ is the virus concentration at a wavelength of 269 nm, $A(269)$ the absorption coefficient at a wavelength of 269 nm, ϵ_{269} the extinction coefficient at 269 nm, and e the length of the spectroscopic cell.

It is also instructive to calculate the mesh size for the concentration range used. The mesh size, as defined in fig.3.4 a), is calculated according to $\xi = L\left(\frac{c^*}{c}\right)^{0.5}$. Fig. 3.4 b), shows the mesh size value as a function of concentration for pf1 and fd. Note that at a fixed mass concentration, the ratio between pf1 and fd mesh size is the following: $\frac{\xi(fd)}{\xi(pf1)} = \frac{L(fd)}{L(pf1)} \cdot \left(\frac{c^*(fd)}{c^*(pf1)}\right)^{0.5} \approx 1$.

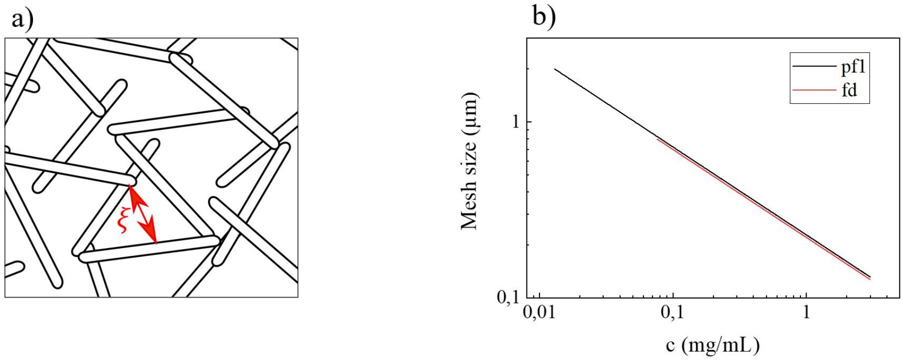

Figure 3.4: a) Sketch illustrating the notion of mesh size for an isotropic suspension of colloidal rods. b) Mesh size as a function of rods concentration for pf1 and fd.

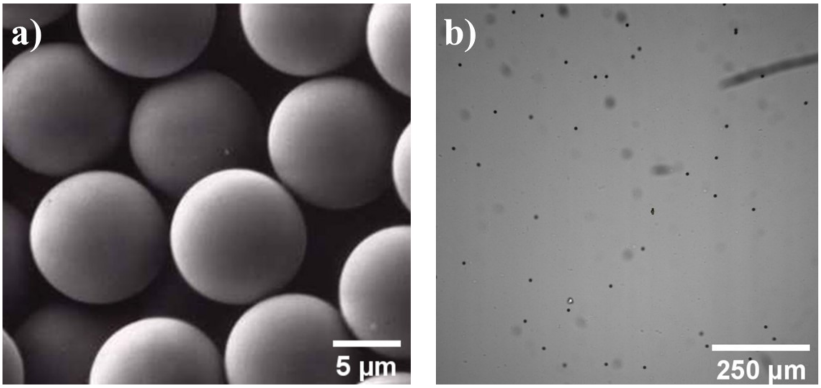

Figure 3.5: a) Scanning Electron Micrograph of the polystyrene inclusions. Adapted from Polysciences Inc. website. b) Polystyrene inclusions, in black, in a fd virus solution at $c(\mathrm{fd}) = 7$ mg/mL, inclusion stress of 1.6 mPa.

Inclusions

Fig. 3.5 a) depicts the polystyrene spherical inclusions that were used in the experiments, as purchased from Polysciences Inc., Polybead® Microspheres . The inclusions have a mean diameter of 10.0 μm, with a variance coefficient of 10%. We determined the density of the beads by tracking their sedimentation speeds in buffers of varying densities, from 1 to 1.055 g/mL. After extrapolation to the 0 sedimentation speed value, the density was estimated at 1.0494 g/mL.

In order to tune the stress applied by the inclusion on the surrounding matrix, the inclusion's density difference with the solvent was tuned. Buffers of densities ranging from 1.000 g/mL to 1.049 g/mL were prepared by mixing 20 mM Tris-HCl buffer with deuterated water, Acros Organic, keeping ionic strength fixed at I = 10 mM. This corresponds to buoyancy forces ranging between $F = 0.25 \times 10^{-12}$ N for the least matched inclusion and 2.05×10^{-15} N for the closest matching. This corresponds to stresses ranging from 0.0013 to 1.6 mPa, using $\tau = F/S$. The final sample was prepared by vortexing the stock virus suspensions, the spherical inclusions suspensions and buffer for approximately 1 minute. This ensures a random distribution of the inclusions in the sample at t = 0, when the rectangular capillaries of dimensions 2.0 mm × 0.2 mm were loaded. The volume fraction of beads in the final samples is $\phi_\mathrm{I} = 0.07\%$ so that we can neglect interactions between the beads. The mixtures of virus and inclusion are considered to be mixtures of rigid bodies, as used earlier in the study of the phase diagram of rod-sphere mixtures [68]. Flexibility of the rods however, affects the results to some extent, as is discussed below.

Imaging.

Sedimentation of inclusions in bacteriophage suspensions was imaged at the middle of the capillary see fig. 3.5 b) with two setups. At the FZJ a home-build horizontal microscope, based on Olympus components (BX-KMA-ESD imaging revolver) a) and equipped with a Hamamatsu ImagEM X2 EM-CCD camera and a polarization filter was used, see fig. 3.6 a). Adapters, holders and capillary holders were made by the FZJ JCNS-PGI workshop. The sample holder includes stages that allow scanning through the sample in the horizontal direction (positional stage) and vertical direction (positional stage combined with rougher tuning). Furthermore, the holder design is adapted to the objective characteristics to optimize illumination conditions. The microscope is calibrated with a TEM grid, Plano-EM brand, 200 square mesh. At the Nestlé Research Center, images were recorded on a Keyence digital microscope, VHX-6000, see fig. 3.6 b), equipped with the VHX-S650 free angle observation system, a polarization filter, and operating with a Keyence software. Both microscopes used a 10× objective and recorded for one hour with a frame rate of 1 image per minute. In addition, smaller timelapses (4 frames per minute) were used to increase resolution of both trajectories and mean square displacements for slowly sedimenting inclusions. Higher magnifications were also used for slow sedimentation speeds.

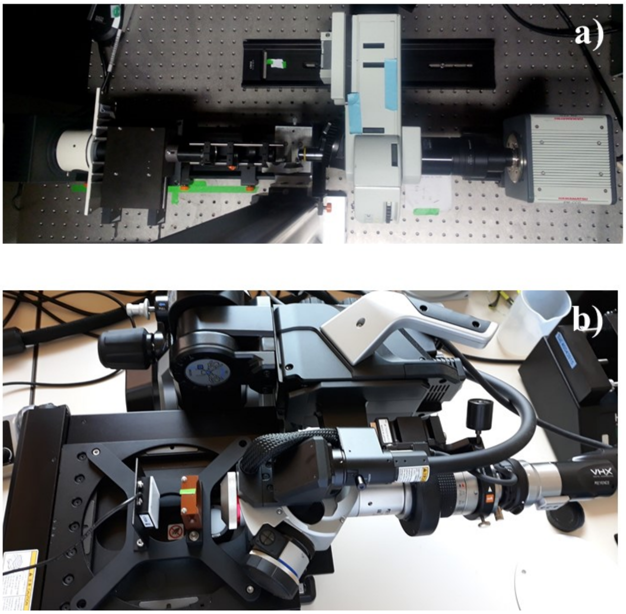

Figure 3.6: a) Home-built horizontal microscopy setup used at the FZJ. From left to right, the white light source and corresponding lenses set and polarization filter, the slot for the sample holder, microscope objective, revolver, tube and camera. b) Keyence digital microscope used at the Nestlé Research Center. From left to right, the planar white light source on which a polarizing filter can be adapted, the sample holder, and the microscope objective. The microscope head is tilted of 90°, which allows for horizontal imaging.

Particle detection and tracking

The inclusions positions were tracked using the particle tracking package Trackpy, which is the python adaptation of the Weeks and Crocker image analysis IDL code [75] for Brownian motion tracking. The raw images are first converted from the tiff format, 16 bits to jpeg, 8 bits using Fiji [141]. The rest of the operations is performed within the adapted trackpy routine. The pictures are thresholded for further image analysis, using the *skimage* package. An adaptative thresholding, *adaptive_thresh* is used, compensating for global variations in the illumination conditions. In the resulting binary image, see fig. 3.7 b), only particles meeting the size criterion, *blocksize* are kept. The out of focus, blurred particles are more gray than the focused particles, and are suppressed using the *offset* feature of *adaptive_thresh*.

The particles detection was made according to two procedures. When the inclusions appear as black spheres on a white background, which is the case for the images from the FZJ setup, the built in trackpy particle detection for picture batches, *tp.batch*, is used. Afterwards, particles are selected according to size and intensity.
The inclusions detected with *tp.batch* are shown in fig. 3.6 c). When the inclusions appear as black circles with a white center, which is the case for the images recorded with the Nestlé Research Center setup, the function *skimage.measure* is used, and the particles are sorted according to a size range criterion, *region.area*. The inclusions detected with *skimage.measure* are shown in fig. 3.6 d). Finally, the particle positions are linked, using the built-in function *tp.link*, regardless of the detection technique. Spurious trajectories are then filtered out with *tp.filter_stubs*.

The original purpose of the Trackpy package is to track down particles Brownian motion. As we want to access the inclusion's average sedimentation speed, we supplement the code with a routine to track the inclusion's sedimentation length as a function of time.

For each inclusion, the downwards trajectories, l_{s} of the inclusions are plotted as a function of the experimental time, t, see fig. 3.8 a). The trajectories evolve linearly with time in case of a classical convective sedimentation. Traces are then selected see fig. 3.8 b), using speed histograms, see fig. 3.8 c). Spurious traces, that correspond to lower speeds are filtered out as they correspond to inclusions close or stuck to the wall. Furthermore, the traces that correspond to higher speeds are also filtered out as they are attributed to dust of two inclusion stuck together. The remaining traces are then averaged and a linear regression is carried out to extract an average sedimentation speed, see fig. 3.8 b). The standard deviation of the slope is a measure of the experimental error.

For slowly sedimenting inclusions, this approach is combined with the additional analysis of the mean square displacements, see fig. 3.8 d). The mean square displacements contributions along the gravity axis and its perpendicular direction are fitted separately. The fits are first performed on the logarithm plots, to determine the slope. For a slope of one, indicating pure diffusion, the mean square displacement (MSD) is fitted linearly in linear coordinates, to extract diffusion coefficients. For a slope of two, indicating pure convective behavior, the MSD is fitted by a second order power law in linear coordinates, which gives the sedimentation speed. When the slope is in between 1 and 2, the MSD is fitted by a second order polynomial law.

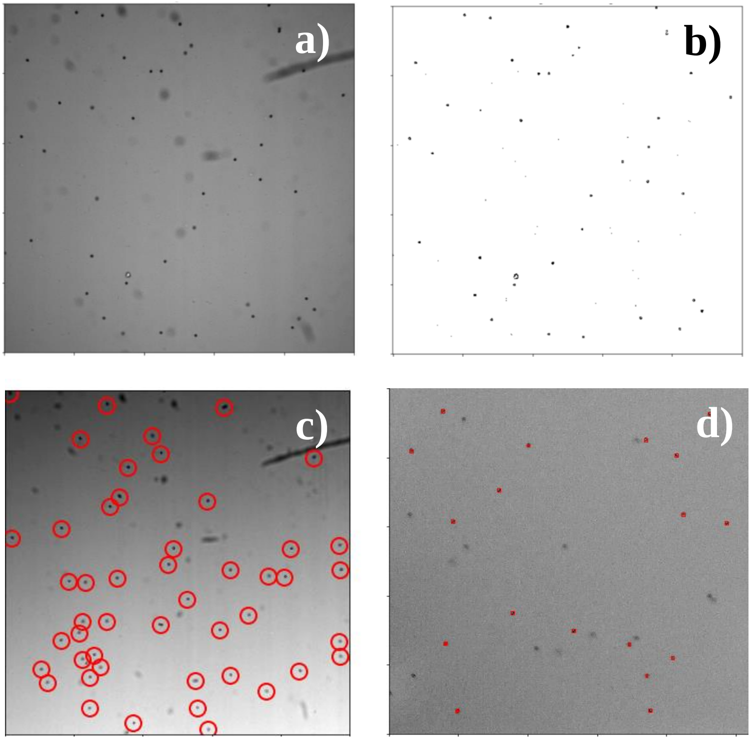

Figure 3.7: Image processing. a) Raw picture b) Thresholded picture. c) Example of inclusion detection for the pictures from the FZJ setup, see fig. 3.6. The initial raw picture (fig. a)) is overlayed with red detection circles centered on the inclusions. The latter were detected with the *tp.batch* command on the thresholded, binary pictures. d) Example of inclusion detection for the pictures from the Nestlé Research Center setup. The initial raw picture is overlayed with detection squares centered on the inclusions. The latter were detected with the *label* command on thresholded, binary pictures.

3.3.2 Diffusion experiments: orientational and translational tracking of fd viruses

Translational and rotational diffusion coefficients of virus particles in virus suspensions were obtained from mean square displacements and mean square angular displacements. These are obtained from fluorescence microscopy on tracer amounts of fluorescently labeled tracer viruses (Alexa Fluor from

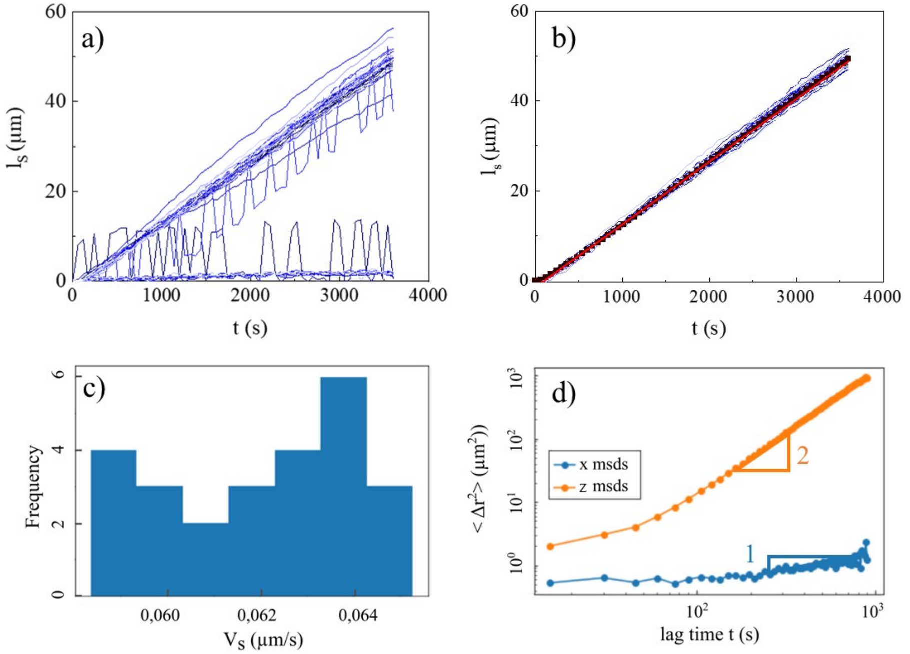

Figure 3.8: Filtering process for $c(\mathrm{fd}) = 7$ mg/mL, $I = 10$ mM and $\tau_\mathrm{I} = 1.6$ mPa. a) Unfiltered sedimentation lengths as a function of time. The sedimentation length is the sedimentation height of the inclusions, minus the height in the first frame. b) Sedimentation length as a function of time, post filtering using the speeds histogram. Scatter: averaged trace. Red line: linear regression of the averaged trace. c) Speeds histogram. d) Mean square displacement (MSD) in the direction transversal to sedimentation, x and in the direction parallel to sedimentation, z as a function of the lag time. Above lag times of some seconds, the MSD in the x direction has a slope of 1, and the MSD in the z direction has a slope of 2.

ThermoFischer) [96]. A Zeiss Axiovert equipped with a 100x NA oil immersion objective, a Prizmatix LED lamp and an Andor sCMOS camera was used for the imaging at frame rates between 10 and 100 fps, depending on the concentration. In order to properly extract the angular diffusion information, a length filter was applied to the traces, so that only particles which diffuse parallel in the plane are tracked. The rotational dynamics follow the Doi prediction, where D_r is proportional to the scaled number density νL^3, see fig. 3.9. The pf1 data deviate more as the rod is effectively more flexible.

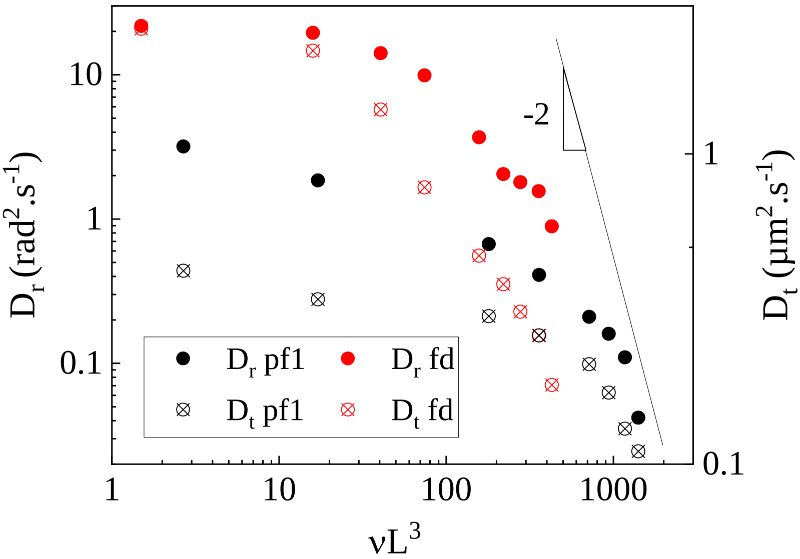

Figure 3.9: Rotational and translational diffusion constants for fd and pf1 virus as a function of number density times the cubed virus length. The diffusion constants were obtained from fluorescent imaging experiments.

3.4 Results

We assessed how inclusion stress, rod concentration and length influence the sedimentation speed. Fig. 3.10 a-c) display an overlay of absolute sedimentation speeds as a function of inclusion stress for the different considered fd rod concentrations. Using the maximum experimental sedimentation speeds for pf1 and fd, we computed maximal inclusions shear rates of 0.05 s^{-1} for pf1 and 0.006 s^{-1}, according to eq. 2.12. The fact that those shear rates lie in the Newtonian plateau of the flow curves in fig. 3.2 motivates the use of the zero-shear viscosity in the SDE prediction. We performed a linear fit of the increasing sedimentation speed with an increase in the inclusion stress and compared the resulting slopes $\langle V_\mathrm{S}/\tau\rangle$ with the SDE prediction, eq. 3.3. The results are plotted in fig. 3.11 d). This prediction gives the correct functional dependence of $\langle V_\mathrm{S}/\tau\rangle$ on the rod concentration. Nevertheless there is a remarkable and unexpected shift of a factor 2.5 between the experimental data and the SDE prediction over the studied concentration range. Note that for the pure solvent the slope corresponds with the Stokes-Einstein prediction.

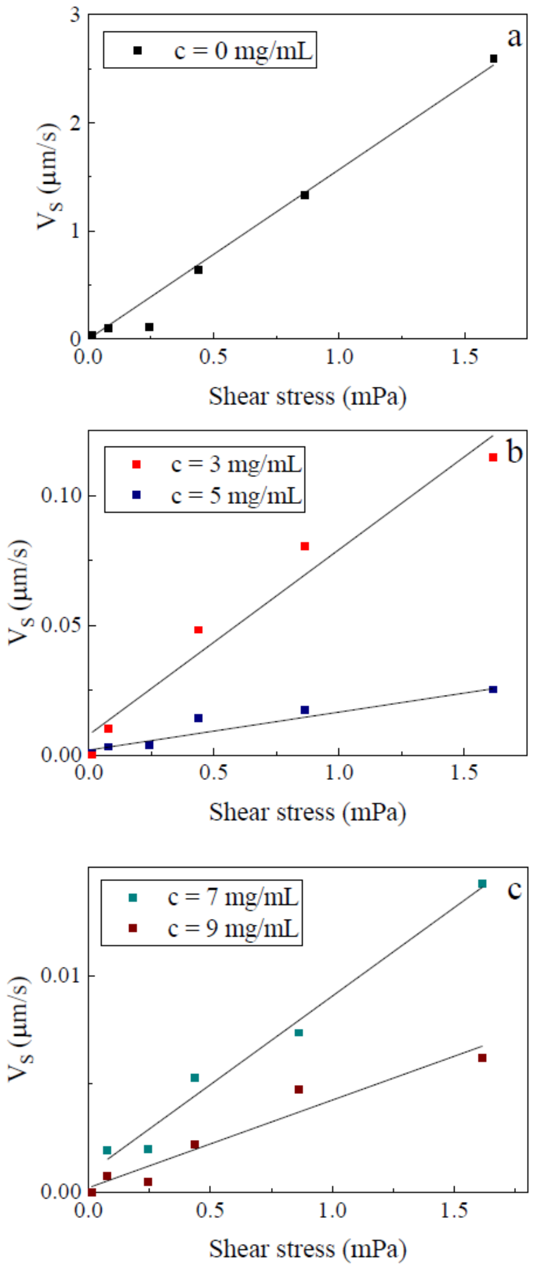

Figure 3.10: Raw sedimentation speed as a function of inclusion stress, with linear regression fits (full lines) for different concentrations of fd virus: a) 0 mg/mL b) 3 and 5 mg/mL and c) 7 and 9 mg/mL.

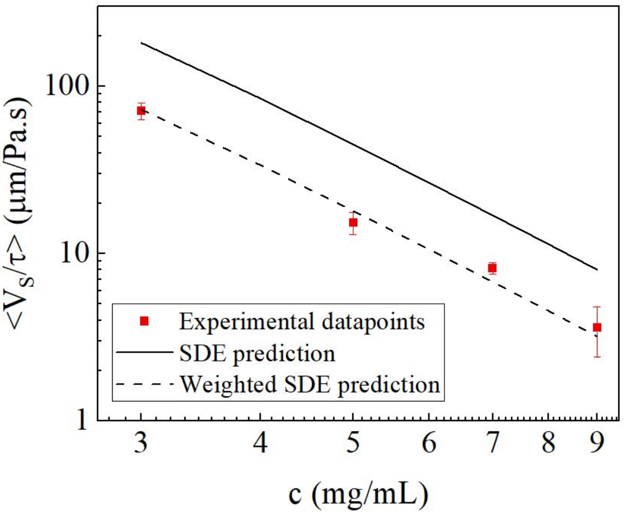

Figure 3.11: Slopes obtained from fig. 3.10 a)-c) as a function of fd rods concentration. The solid line is the SDE prediction, and the dashed line is the SDE prediction divided by a factor 2.5.

Fig. 3.12 a) displays the reduced sedimentation speed versus the concentration for fd and pf1 at a fixed inclusion stress of 1.6 mPa. As expected, a deviation from the SDE prediction for stiff rods is also observed in this representation. It is similar for both rods, but more pronounced for the longer pf1 system than for the shorter fd. Furthermore, the deviation for pf1 is even more pronounced when using the SDE prediction accounting for pf1 flexibility. Again, we can fit the data by correcting the SDE prediction for fd with a factor 2 and the SDE prediction for pf1 with a factor 4 when the rod is considered stiff. The SDE prediction for pf1 accounting for flexibility can be scaled with a factor of 7. This scaling is obviously only valid for the high concentrations. The more pronounced slowing down for pf1 is in accordance with eq. 3.3, which states that the longer rod length results in an overall higher viscosity for an undisturbed isotropic network of rods and therefore in slower sedimentation speeds for pf1. In order to take into account the very different overlap concentrations of both systems, we scale the concentration with c^*, see fig. 3.12 b). Remarkably, the experimental values for pf1 and fd collapse on one master plot.

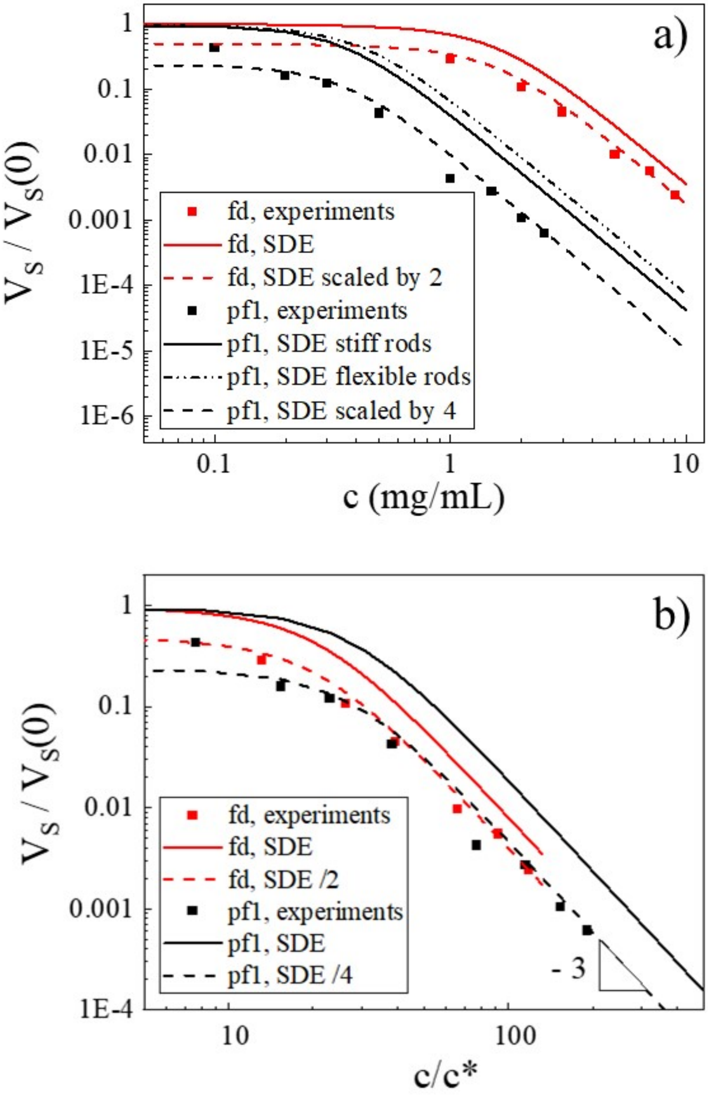

Figure 3.12: a) Reduced sedimentation speed for fd and pf1 at an inclusion stress of 1.6 mPa with the SDE prediction. In the case of pf1, the flexibility of the rods was taken into account by using two values of the constant A, which is a coefficient in the modified diffusion coefficient expression [93], see section 3.2. b) Reduced sedimentation speed as a function of reduced rod concentration c/c*, for both systems fd wild type and pf1.

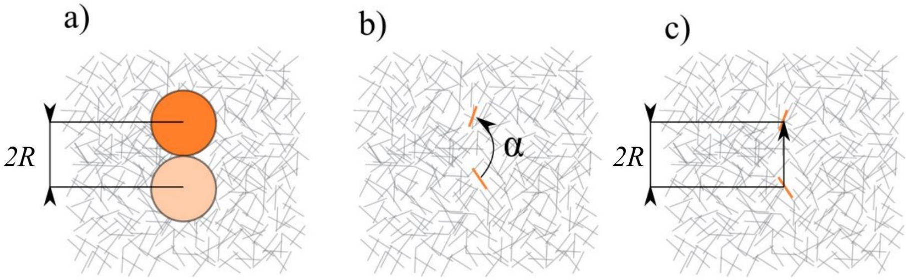

Figure 3.13: Sketch illustrating the definition of the characteristic sedimentation, translational and rotational times. a) The characteristic sedimentation time is the time needed for an inclusion to fall of one inclusion diameter. b) The network rotational relaxation time is defined as the time for a colloidal rod to change its orientation by an angle α. c) The network translational relaxation time is the time needed for a rod to translate of one inclusion diameter.

3.5 Discussion

3.5.1 Absence of a yield stress

The first conclusion we can draw from our experiments is that the existence of an apparent yield stress for dispersions of semidilute ideal slender rods cannot be claimed. Indeed, the data shown in fig. 3.10 in principle all extrapolate to zero. The analysis of the mean square displacement in the direction transversal to sedimentation evidences diffusive motion, as expected. Most of the mean square displacements in the sedimentation direction are convective; for the lowest studied stresses, however, a transition from convective to diffusive motion can be noticed. For those specific datapoints, the amplitude of the extracted diffusion constant in both direction are comparable. The absence of convective motion for the lowest stresses, as reported, is attributed to the very low density mismatch between the inclusions and the medium.

3.5.2 Discrepancy between experimental and theoretical speeds

We do observe a substantial slowing down of the sedimentation, which displays the same concentration dependence as predicted by the SDE prediction based on the rotational relaxation of the rods. However, the SDE underestimates the slowing down by a factor that seems to depend on the rod length. To interpret

the results, we start by validating the assumption that the relevant viscosity is the zero-shear viscosity, see eq. 3.2. To this end, we need to compare the sedimentation-induced shear rate with the relevant relaxation time per system: the time associated to the rotational diffusion in the case of rods.
As illustrated on fig. 3.13, the characteristic sedimentation time is defined as the time needed for an inclusion to fall over a distance of one diameter, $\lambda_\mathrm{S} = 2R/V_\mathrm{S} = 1/\dot{\gamma}$.
For the suspension of colloidal rods, we define a rotational network relaxation time, $1/D_\mathrm{r}$, where D_r is an experimentally determined rotational diffusion coefficient associated to rods in the semidilute regime [92].

As detailed in section. 2.2.1, eq. 2.23, the corresponding rotational Peclet number is defined as:

$$Pe_\mathrm{r} = \frac{V_\mathrm{S}}{2RD_\mathrm{r}}. \tag{3.5}$$

Fig. 3.14 a) displays the experimental rotational Peclet number for fd and pf1 as a function of rod concentration rescaled by c^*. For both rods, the rotational Peclet number is always much smaller than 1, so the sedimentation is slower than network relaxation, and no shear thinning takes place for the considered systems, as experimentally confirmed by the absence of birefringence during sedimentation [130], see fig. 3.15. This validates the use of the zero-shear viscosity in the Stokes-Doi-Edwards prediction.

The fact that the experimental speeds are smaller than computed from the macroscopic SDE relation rather implies that the inclusions sense a higher viscosity than the zero-shear viscosity obtained from the bulk rheology, as reported for other viscoelastic shear-thinning systems [104, 59] as mentioned in ch. 2.2.3. The drag correction factor [86] between the SDE prediction and experimental speeds is within the reported range for viscoelastic shear-thinning fluids [104, 86]. We want to further understand whether a local flow-induced shear thickening could develop in front of the inclusion, as opposed to the shear thinning discussed above. In bulk rheology a homogeneous shear flow is exerted on all the probed fluid. In contrast, a falling inclusion exerts an heterogeneous, localized stress on the medium, so that local microscopic effects around the inclusions need to be considered. Indeed, complex velocity patterns around inclusions were evidenced by particle tracking velocimetry in the vicinity of large inclusions falling in yield stress fluids [134, 130], and for shear-thinning fluids composed of anisotropic-like particles [110, 157] in the creeping flow regime. For small inclusions diffusing in fd virus networks, Kang et al. [80, 81] assumed a local density variation below (higher rods density in the sedimentation front) and above (lower density in the sedimentation wake) inclusions. This may

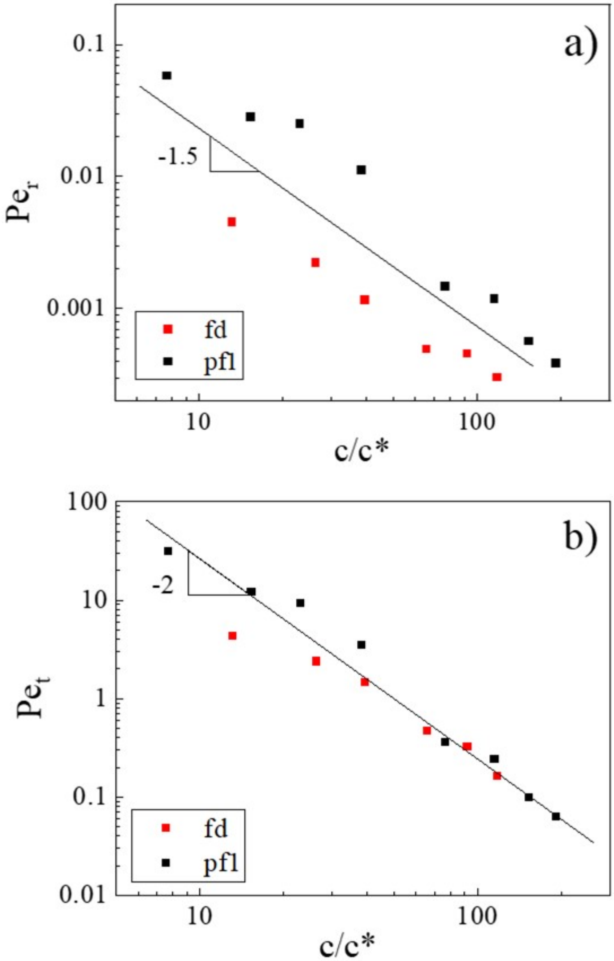

Figure 3.14: a) Rotational and b) translational Peclet number for fd and pf1 as a function of rod concentration rescaled by c^*. The Peclet numbers are calculated using sedimentation rates from experiments. The characteristic diffusion times at the corresponding rod concentrations are extrapolated from fig. 3.3.2.

explain discrepancies between the viscosity in the vicinity of the inclusion, and the one measured with macroscopic rheometry.

We showed above that in our experiments, the sedimentation of the inclusion does not affect the local orientational order. However, it could indeed be that there is a densification in the front of the sedimenting inclusion, which would lead to a higher local viscosity. As detailed in section 2.2.3 such a restructuring mechanism has been mentioned for inclusions sedimenting or creaming in sparse wormlike micelles [160] and cellulose suspensions [51] and recently evidenced at low concentrations in cellulose [146] at which restructuring is favoured, see section 2.2.2. Our results on rods could therefore support the densification hypothesis for low concentration micellar systems [160], see section 2.2.3, rather than the formation of circular micelles at low shear [160]. As the relevant relaxation mechanism for concentration gradients is translational diffusion, we introduce the experimentally defined translational relaxation time. It is defined as the time needed for a rod to translationally diffuse over the diameter of the inclusion, equilibrating local concentration gradients $(2 \cdot R)^2/D_{\mathrm{t}}$, where D_{t} is the parallel diffusion coefficient associated to rods.
The corresponding translational Peclet number is now defined as:

$$Pe_{\mathrm{t}} = \lambda\dot{\gamma} = 2R\frac{V_{\mathrm{S}}}{D_{\mathrm{t}}} \tag{3.6}$$

Fig. 3.14 b) displays the translational Peclet number for fd and pf1 as a function of the rescaled rod concentration. Over the full concentration range, Pe_{t} is about two orders of magnitude higher than the rotational Pe_{r}. This does indicate that the translational reorganization is not instantaneous as it is the case for the rotational reorganization. We hypothesize that a crowding effect in front of the inclusion is at the origin of the slower sedimentation speed observed, in comparison with the SDE prediction. However, the continuous decrease in Pe_{t} contradicts the observed constant deviation from SDE, especially at high concentrations. Moreover, at fixed concentrations Pe_{t} is lower for pf1 than for fd, which cannot explain the larger discrepancy between experimental and theoretical speeds for pf1.

3.5.3 Note on the overlap concentration

The larger difference between experimental points and SDE theory, when comparing the pf1 data to the fd data, could imply that microscopic reorganization effects, unaccounted for in the hypothesis of the undisturbed isotropic network, are even more pronounced for longer rods. Decrease in the mesh size is reported to cause drag enhancement [86] however, this cannot explain discrepancies between fd and pf1 experimental speeds as the mesh size is similar for fd and pf1 at a fixed concentration. As the overlap concentration is a key difference between both systems, we also plotted the results as a function of the concentration rescaled by the overlap concentration. Interestingly, the data for fd and pf1 superimpose when doing so, which suggests that the sedimentation speed also depends on the number of entanglements per rod. This is not the same as the tube diameter that is the base of Doi's theory as reflected in eq. 3.2. Although the relaxation of entanglements is still correctly described by Doi, given the correct concentration dependence of V_S and results from rheology [93], there seems to be an extra contribution to the viscosity when dragging an inclusion through an entangled medium. Assuming that there is a densification in front of the falling inclusion, there is a resulting imbalance in the osmotic pressure between the wake and the front of the inclusion. This imbalance would drive the inclusion in the direction opposite to the sedimentation direction. This extra contribution would be concentration and length dependent. In order to adjust the SDE prediction in the context of inclusion sedimentation, in future work, the use of fluorescently labelled rods could provide with an estimate of the local rod concentration and diffusion front of the inclusion.

The overlap concentration is also key to explain the increased discrepancy for pf1 between experimental speeds and the SDE prediction when accounting for flexibility. Flexibility causes on the one side a lower macroscopic zero shear viscosity [93] due to the extra relaxation mode but hardly affects the overlap concentration. On the other side, the sedimenting inclusion is not sensitive to this relaxation as it does not affect the overlap concentration. This is an important notion, considering the many semi-flexible systems used in applications. When flexibility increases further, the overlap concentration is at some point affected, as is the case for linear polymers, for instance.

3.5.4 Outlook: feasibility of pnipam-coated fd gel

So far we have discussed the sedimentation of spheres through a network of rods, where the rods always relax and do not exhibit a yield stress. It is, however, also possible to make a network of rods, that forms a gel, exhibiting a true yield stress. Indeed, fd virus suspensions grafted with Poly(N-isopropylacrylamide) were shown in previous works to display gel like properties above a critical temperature [166, 136]. Upon heating the pnipam grafted fd suspensions, water is no longer a good solvent for the polymer and as a consequence, the polymer undergoes a sharp coil to globular conformation transition [166]. It is therefore thermodynamically favorable for single rods to form contacts with the neighbouring rods to minimize polymer contact with the solvent. This is the driving force for the attraction between the rods and the resulting

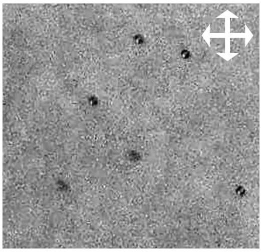

Figure 3.15: Birefringence image of sedimenting 10 μm polystyrene spherical inclusions in a pf1 virus solution at c(pf1) = 2.8 mg/mL, inclusion stress of 1.6 mPa. Although the contrast is enhanced, and light intensity maximized in crossed polarized configuration, no birefringence around the falling inclusions is observed.

gelation above the critical temperature. The gel strength can be tuned as a function of the operation temperature, ionic strength, and virus concentration. Pnipam grafted fd virus gels are therefore adequate model systems to widen the understanding of the mechanisms at stake in stabilizing inclusions by attractive anisotropic particles [51, 146, 12]. Yield stress fluids composed of castor oil fibers indeed have the same stabilizing efficiency as Carbopol [107] as predicted by the macroscopic critical yield number [17], whereas cellulose suspensions [51, 146, 145] hold heavier inclusions than the critical yield number predicts [17], due to restructuring effects happening essentially at low concentrations [146]. Similar sedimentation experiments as the one presented in this chapter could therefore be carried out, where the rheological properties of inclusion loaded pnipam grafted fd gels [136] are compared to the rheological properties of inclusion loaded gels composed of isotropic particles [90]. Such an experiment would show whether the continuum approach for the matrix is valid when considering linear, non-linear and recovery properties [99, 51, 146], or possible restructuring effects of the anisotropic particles during shear have a significant influence on one of the aforementioned properties. Indeed, we started such a study, the results which are discussed in the appendix A, but it could not be finished.

3.6 Conclusion

Sedimenting, inert spherical inclusions suspended in semidilute dispersions of ideal monodisperse rod-like particles, of lengths 0.88 and 2.1 μm, were tracked. The influence of rod concentration, rod length and inclusion stress on the sedimentation speed was investigated. We report a strong decrease of the reduced sedimentation speed as a function of rod concentration, and no apparent yield stress could be identified for the system. Using a theoretical prediction for the zero-shear viscosity of these systems, we find the correct concentration dependence of the sedimentation speed. Hence, the effect of the rod length is very pronounced so that a two-fold increase in the length of the rod slows down the sedimentation speeds by two orders of magnitude at a fixed concentration. The results for both rod lengths superimpose, however, when scaling the concentration with the overlap concentration and there is a constant difference between experiment and theory of a factor 2 and 4 for the shorter and longer rods, respectively. When flexibility is taken into account, the difference with theory is even larger. We infer that crowding in front of the inclusions, causing an increased viscosity, is not sufficiently equilibrated by translational diffusion of the rods. This phenomenon still needs a theoretical underpinning.

3.7 Acknowledgements

The JCNS-PGI workshop, FZJ, is acknowledged for assistance in design and realization of the capillary holder and other items on the home-build horizontal microscopic setup. Harmut Kriegs is acknowledged for general discussions on the setup. Karin Sellinghof is acknowledged for the preparation of fd virus suspensions. Last but not least, Sergei Abakumov is acknowledged for colloidal rods rotational and translational diffusion data.

Chapter 4

Rheology of doped gels

4.1 Introduction

The rheology of doped gels, that is gels in which inclusions are stabilized at rest [17], is of interest for practical and theoretical use, because of the omnipresence of inclusions in viscous matrices, in natural systems and industrial applications, as detailed in ch. 2.

Casting or shaping gels requires knowledge of rheological properties: it is indeed of practical use to know what range of shear stresses is required to spread cream on skin or whether a brick of pasty material can sustain its own weight, parameters that can be predicted using the materials's yield stress. Adding inclusions in such gels potentially influence the rheological properties and therefore the processing steps parameters or the product end properties, as explained in section 2.2.2, which is why the influence of inclusion addition on rheological properties needs to be predicted. Further to that, the rheology of large inclusion suspensions in yield stress fluids sets experimental and fundamental challenges [28, 126].

A prerequisite to study the rheology of large inclusions suspensions in yield stress fluids is that the inclusions are stabilized at rest in the matrix. As detailed in section 2.2, inclusion stability can be predicted according to macroscopic parameters of the matrix and the inclusion, using the dimensionless yield stress [17, 18, 15, 124, 134, 149]. Shear flows were shown to induce the sedimentation of inclusions stable at rest in the yield stress fluids [17] for all density mismatch [124, 61].

Gel elasticity and yielding according to non-deformable inclusion volume fraction has been predicted for inclusions that are stable at rest in the matrix as the density mismatch is moderate enough to prevent large scale sedimentation during the experiments [60, 52, 99, 28, 69, 3, 50]. As further detailed in section 2.2.2, a first trend is reported when inclusions mechanically interact with the matrix in the sense of an elastic mechanical network, and no direct physicochemical interaction takes place between the inclusion and the matrix [28]. In that case, as predicted by phenomenological laws [28], density mismatched inclusions enhance linear properties [28, 99] and the reduced yield stress [99, 52, 3] irrespective of the microscopic origin of the yield stress [99, 115, 35]. In the case when the inclusions do not interact mechanically with the matrix, the yield stress [3, 156] decreases upon inclusion addition for low inclusion fraction, then rises again for higher inclusion fraction due to the formation of an inclusion superstructure.

Yielding is an interplay between microscopic changes in the material surrounding the inclusion [88] and the sedimentation force exerted by the inclusion [17, 71]. Therefore it is of interest to use systems in which the connection of yielding with microstructural features is well understood [88, 109].
With respect to the aim of this work, the previous chapter focus point was on assessing the stabilization properties of large inclusions in a benchmark suspension of model rods, in order to understand better the role of the suspension's single particles on the mechanism of inclusion trapping. In this chapter, we use a model system composed of attractive spherical particles in order to study a benchmark reference system composed of attractive model isotropic particles. The aim of the present study was to investigate linear and non-linear rheological properties for a well characterized doped yield stress fluid, as well as the influence of inclusions on the yielding mechanism of the matrix. As inclusions impose a local stress on the matrix, it is of interest to know whether the combination of inclusion stress and external stress promote yielding and/or how it affects matrix recovery upon shear stress removal [109, 111]. To elucidate this phenomenon, we report here a systematic rheological study of large non-Brownian inclusions in model systems of attractive colloidal particles. Among studies of large inclusions in colloidal suspensions, results belong to both aforementioned trends with regards to inclusion fraction impact. Inclusions in a system of bentonite and kaolin clays were shown to enhance the linear elastic modulus [99] and the yield stress [99, 3]. A system of glass inclusions in kaolin colloidal clays was studied by Ancey et al. [3], the decrease of the elastic modulus at low inclusion fraction is attributed to the formation of a depletion layer at the inclusion interface.
Our choice for a model system was a suspension of attractive PMMA spheres, as the sample can be rejuvenated by a well defined pre-shear protocol [109] and rheological properties in the linear and non-linear regime are well characterized [87, 90, 88] as is further explained in section 2.3. A key feature observed in such depletion gels during nonlinear shear is its two step yielding attributed to

attributed to bond breaking and restructuring at short length scales and cluster breaking and rearrangements at larger length scales [90, 109].

In this work, we investigated whether the influence of an increase in the inclusion fraction matches the Krieger-Dougherty trend that describes the increase of the reduced elastic modulus with an increasing inclusion fraction, as reported for previously studied generic systems using low amplitude oscillatory tests. Furthermore, we assessed whether the inclusion stress due to the density mismatch influences the yielding characteristics of the gels, that is the two step characteristic yielding of the system, which we investigated by dynamic strain sweep and step rate tests. Lastly we investigated the influence of inclusion on gel formation and recovery under shear.

4.2 Depletion interaction notion and volume fraction dependence phenomenology

The matrix is a gel at rest as the individual subcomponents, colloidal spheres are attracted to each other due to depletion interactions. As further explained in section 2.3, coiled polymers in the solution are responsible for the occurence of such depletion interactions [122], that is the attraction of two colloids in their overlapping zone depleted of coiled polymers.

As detailed in section 2.2.2, literature [28, 99] shows that the linear elastic modulus of an inclusion loaded matrix divided by the elastic modulus of the bare matrix was shown to follow a Krieger-Dougherty rule.

$$\frac{G'(\phi)}{G'(0)} = g(\phi) = \left(1 - \frac{\phi}{\phi_\mathrm{m}}\right)^{-2.5\phi_\mathrm{m}} \tag{4.1}$$

where $G'(0)$ is the elastic modulus of the bare gel, $G'(\phi)$ the modulus of the inclusion doped gel, $g(\phi)$ an inclusion fraction dependant function, and ϕ_m an experimentally determined maximum packing fraction equal to 0,57 [99], which was derived from the least square fit of Mahaut et al. reduced elastic moduli experimental data.
Similarly, the yield stress can be predicted [28, 99]:

$$\frac{\tau_\mathrm{C}(\phi)}{\tau_\mathrm{C}(0)} = \sqrt{(1-\phi)g(\phi)} \tag{4.2}$$

where $\tau_\mathrm{C}(0)$ is the yield stress of the bare gel and $\tau_\mathrm{C}(\phi)$ the yield stress of the doped gel.

4.3 Materials

4.3.1 Matrix

Polymethylmethacrylate (PMMA) colloidal particles dispersed in an octadecene solvent, are considered as hard spheres. Their surface is stabilized through the covalent grafting poly-hydro-stearic acid (PHSA) chains (of an approximated length of 10 nm). The microspheres have a diameter $D = 0{,}267\ \mu$m and a polydispersity of 10%, as to avoid crystallisation [90]. The stock solution of PMMA colloidal spheres dispersed in octadecene, has a volume fraction of $\phi_{\text{col}} = 46\%$, which was experimentally verified from dynamic time sweep measurements. The sample was first carefully vortexed to ensure sample homogeneity, while taking care that the sample is bubble free. The elastic modulus at the frequency of $\omega = 0.1$ rad.s^{-1} was determined from dynamic time sweeps and compared to the reference $G' = h(\phi)$ graph, fig. 4.1 [89].

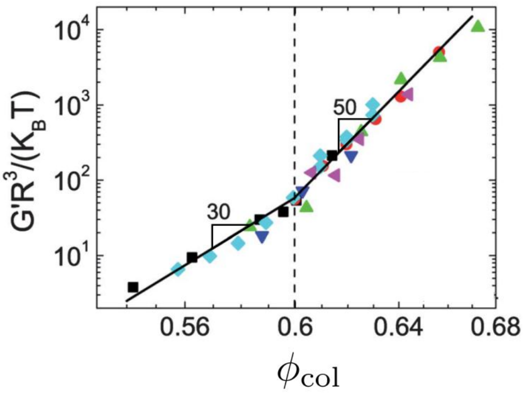

Figure 4.1: For a stock solution of PMMA colloidal spheres, linear elastic modulus scaled by the cubic colloids radius and by thermal energy k_BT as a function of colloids volume fraction. The experimental points correspond to PMMA colloids of radius ranging from 130 to 300 nm, dispersed in various organic solvents. The slope is of 30 below the glass transition, and 50 above. Adapted from Koumakis et al. 2012 [90].

4.3.2 Depletant

Coiled linear polybutadiene polymer chains are responsible for nanometric scale depletion interactions between the colloids in the matrix as explained in section 2.3. The solution of depleting polymer, was obtained by diluting the reference polybutadiene (P1841-Bd, Polymer Source) stock solution, in octadecene. The polybutadiene has a molecular weight, M_{w}=323000 g/mol, a polydispersity index of $M_{\mathrm{w}}/M_{\mathrm{n}} = 1.13$ with M_{n} the number average molar mass and a radius of gyration, $R_{\mathrm{g}} = 19$ nm. Due to the high viscosity of the stock polymer solution, the solution was magnetically stirred during one full day to optimize sample homogeneity. The polymer colloid size ratio was $\xi = R_{\mathrm{g}}/R = 0.11$, the polymer concentration, c/c* = 0.35, with c* the polymer overlap concentration defined as $c^{*} = 3M_{\mathrm{w}}/4\pi N_{\mathrm{a}}(R_{\mathrm{g}})^{3}$, where $\mathrm{N_a}$ is the Avogadro number. This gives a Asakura and Oosawa [122] interaction potential at contact of $U_{\mathrm{dep}}(2R) = -10k_{\mathrm{B}}T$ [122], see section 2.3 for more details on the interaction potential.

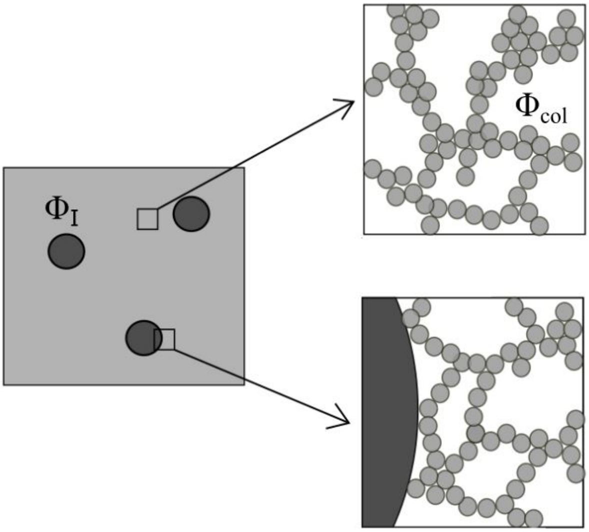

Figure 4.2: Sketch of the inclusion doped colloidal gel. Above, magnification of the colloidal solution, below, magnification of the colloidal solution next to the inclusion. The colloids as well as the characteristic cluster size are larger than in reality.

4.3.3 Inclusions

Fused hollow non-porous borosilicate glass spheres, Sphericel 110P8, of diameter of 12 μm, and of a density of 1.1 ± 0.05 g.mL^{-1} were purchased from Potters Spheres. The density mismatch corresponds to a buoyancy force of $F_{\mathrm{I}} = 9.94$ pN and, using $\tau_\mathrm{I} = F_\mathrm{I}/S$, where S is the surface of the sphere, an inclusion stress of $\tau_\mathrm{I} = 4.4$ mPa.

4.3.4 Sample preparation

PMMA colloidal suspensions with a fixed final volume fraction of $\phi_\mathrm{col} = 20\%$ were prepared, with inclusions volume fractions up to $\phi_\mathrm{I} = 10\%$.

The solid content volume fraction is defined as follows:

$$\phi_\mathrm{sol} = \phi_\mathrm{col} + \phi_\mathrm{I} \tag{4.3}$$

where $\phi_\mathrm{I}, \phi_\mathrm{col}, \phi_\mathrm{sol}$ are respectively, the inclusion, colloids, and total solid content volume fraction. In Fig 4.2, the notion of inclusion fraction in the sample as well as the colloidal fraction are illustrated, giving a microscopic picture of the colloidal structure in the sample as well an approximation of the characteristic size of the colloidal structures with regards to the inclusion size.

The polymer solution prepared as described in section 4.3.2, the colloids stock solution, the inclusion solutions as in section 4.3.3 and the octadecene solvent were poured together with the proper ratio to go the desired position of the colloid-polymer-inclusions phase diagram. The vial was then vortexed at 3500 rpm for 1 min, to ensure that all material is at the bottom of the vial. The high viscosity sample was then magnetically stirred overnight to ensure full homogeneity. Lastly, the sample was visually checked for homogeneity by dipping a spatula inside the vial and seeing whether large agglomerates of sample were present in the liquid phase, then further homogenized if that was the case.

4.3.5 Analysis techniques: Rheology and Imaging

Imaging

Stability of suspensions was checked using the home-made setup at the Forschungszentrum Jülich (FZJ), see ch. 3 for more details. Custom microscopy cells designed at the glass workshop were used, with dimensions preventing confinement with regards to both inclusions and clusters size; bubble trapping is prevented due to the addition of a dedicated cylindrical trap on top of the imaging cell. The samples are imaged at the center of the cell on fig. 4.3.

Furthermore, rheo-imaging experiments were carried out to assess inclusion sedimentation under shear, as well as potential gel microstructural evolution.

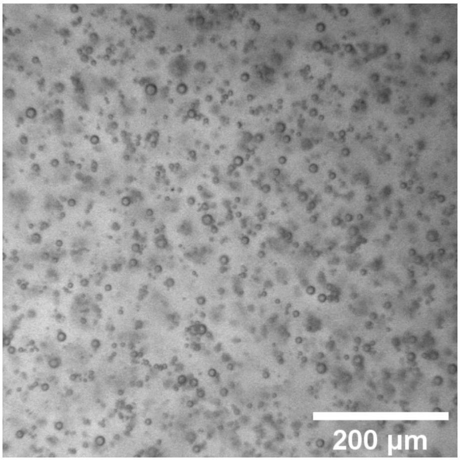

Figure 4.3: Optical microscopy image of the inclusions in the colloidal gel obtained using the FZJ's home-made setup.

An Anton Paar MCR 302 WESP rheometer was equipped with a glass bottom plate and an upper metallic plate to allow for darkfield imaging in reflection mode. Macroscopic rheological results were compared with those on the ARES rheometer and were found to be similar. Dark field imaging was performed during shear. Imaging during oscillatory pre-shear is a challenge, as only a good synchronization between the photo sampling rate and the shear rate allows for the sharp observation of the same sample location on each picture. However, comparison of inclusion density and overall gel microstructure is possible before and after pre-shear.

Rheology

The macrorheological tests were performed in FORTH (Crete) on a ARES (TA Instruments) strain controlled rheometer. The cone-plate geometry was selected as it ensured a homogeneous shear rate in the gap; furthermore, roughened surfaces (serrated and randomly patterned cone and randomly patterned plate) prevent slip with such low and intermediate volume fraction gels. This was needed as the appearance of a layer of solvent at the interface with a smooth geometry, is indeed often encountered for these systems. We used an upper cone of diameter 25 mm, of angle 0,047 rad, and of gap height 47 μm. The geometries were calibrated by a reference silicon oil (96 mPas, Brookfield). The absence of slip was verified by recording flow curves and time sweeps using a reference 20% colloids sample with U = -10k_BT [9]. The flow curve follows a

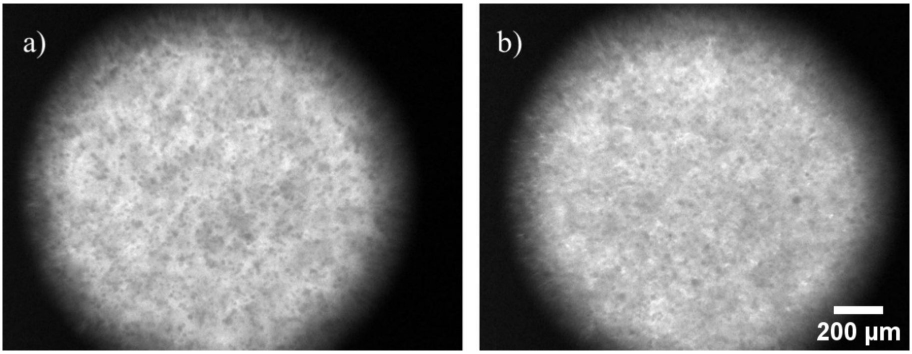

Figure 4.4: Optical microscopy darkfield imaging of the PMMA colloidal gel doped with 5% inclusion fraction a) before b) and after pre-shear. The inclusion are in dark grey on a lighter gray background.

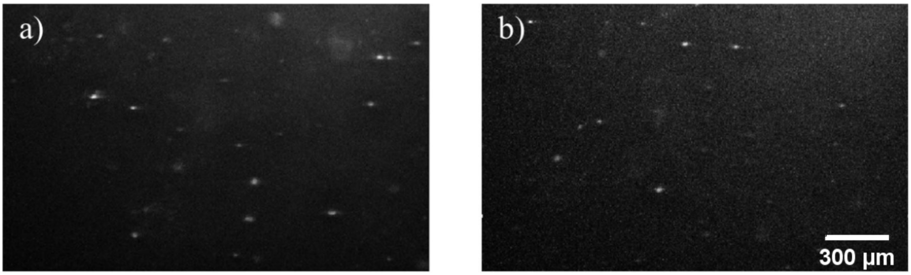

Figure 4.5: Laser reflection images of the colloidal gel with 5% inclusion fraction, at different steps of the pre-conditioning tests. The inclusions appear white on a dark background. The samples are imaged just above the bottom plate. The left picture was taken after the pre-conditioning test at 300% strain, the right picture was taken after a later test, the pre-conditioning test at 800% strain.

single curve, there is no curve inflection for lower strain rate values. The probed samples were disposed on the bottom plate using a pipette and changing the deposition orientations to curb sample alignment effects.

As shown in fig. 4.6, all test protocols are based on a sequence of three blocks: rejuvenation, recovery, test. *Block 1* is a rejuvenation block, which consists of a high strain amplitude oscillatory shear at a strain amplitude of 800% and an angular frequency $\omega = 10$ rad.s^{-1} for 188 s, which is long enough to ensure a full breakage of the initial structure and therefore an efficient rejuvenation. Through the rejuvenation step, pre-alignment effects due to sample loading were suppressed, hence ensuring that each test was performed for the same

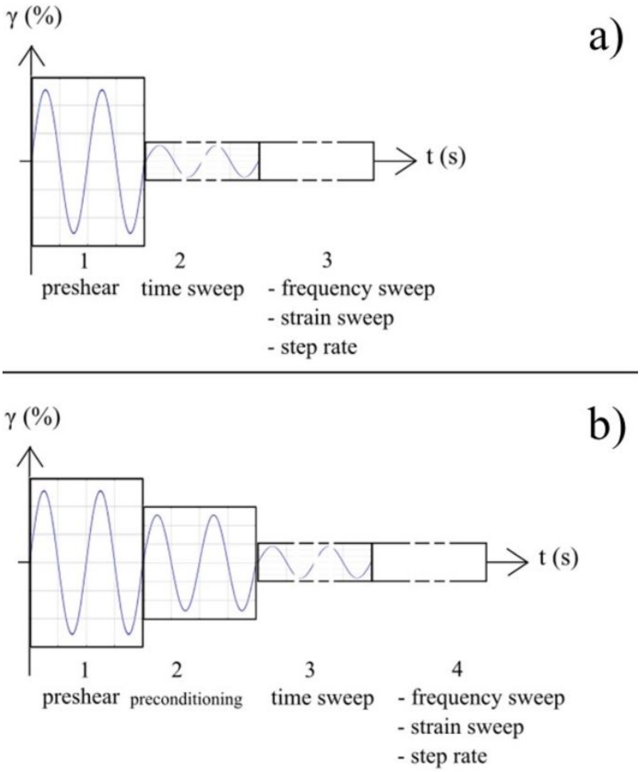

Figure 4.6: Schematics of the test protocol. a) Pre-shear at high oscillation amplitude is followed by recovery, followed by the actual test: linear properties and their evolution are probed using dynamic frequency sweeps or time sweeps, while non-linear properties are assessed using strain sweeps and step rates. b) A preconditioning step is inserted between pre-shear and recovery: the sample undergoes oscillatory shear at specific amplitudes in order to tune the sample's properties [109].

reproducible initial state of the sample [88]. Following the pre-shear step, sample recovery was monitored over time in the linear range for a duration of 700 s, *Block 2* at a strain amplitude of 0.9% and a frequency of 10 rad/s. During this block, the yielded gel reforms and the elastic and loss modulus increase until stabilization: the elastic modulus reaches a plateau value of G'_{pl}. *Block 3* is the actual test. This test was chosen depending on the property that needs to be probed: linear (frequency sweep) or non-linear (strain sweeps, step rate). Linear properties were probed by assessing the value of G'_{pl} as a function of the inclusion volume fraction. Furthermore, the linear properties for a wide range of frequencies were determined by dynamic frequency sweeps in block 3. Non-linear properties of the system were explored by performing strain sweeps at various frequencies, i.e. $\omega = 0.1$, 1, 10 rad/s as well as step rate tests at a shear rates of 0.05 s^{-1} in *Block 3*.

As discussed in section 4.4, it turned out that the protocol of successive pre-shear, recovery and test as depicted in fig. 4.6 a) needed to be modified to highlight differences between the reference undoped gel and the gel with inclusions. Thus, a so-called pre-conditioning step was inserted in between pre-shear and recovery, as depicted in fig. 4.6 b). It is an oscillatory time sweep where the amplitude of the oscillation is the pre-conditioning parameter that allows to obtain gels of different initial microstructure: the liquefied gel recovers either freely or under different strain amplitude values, which gives rise to several microstructures. The oscillation amplitude was taken in the set $\gamma = [5;\ 25;\ 50;\ \ 100;\ \ 300;\ \ 800]\%$, and the oscillation frequency was of 10 rad/s. This was followed by a dynamic time sweep to ensure full stabilization of mechanical properties. The last step is a frequency sweep. The pre-conditioning step generates 20% volume fraction colloidal gels of varying microstructure [88], which allowed us to probe whether the presence of inclusion hindered recovery for specific microstructures.

4.4 Results

4.4.1 Imaging

The inclusions were stable at rest in the gels during at least two days, with an exact match of the images at the beginning and at the end of the stability tests. The dimensionless yield stress value is approximated to Y = 20, the absolute yield stress being extracted from flow curve experiments, see section 2.2 for more details. As the dimensionless yield stress is higher than the critical yield number for spheres, 0.143 [17], stability at rest is indeed expected.

In fig. 4.4, the 5% inclusion sample before and after pre-shear is displayed. Inclusions can still be seen after the pre-shear step and are in focus, which implies that no significant sedimentation is observed during the high shear amplitude yielding event. Similarly, no sign of sedimentation was observed by comparing the inclusion profile before and after the recovery steps or the test steps including the dynamic strain sweeps and the step rate tests, for the considered inclusion contents. In fig. 4.5, the laser reflection images of the inclusions are displayed, during several steps of the pre-conditioning tests. The inclusions are imaged near the bottom plate, and the inclusion number in both pictures is compared. No significant increase of the inclusion fraction is reported between the two pictures, as we would expect if sedimentation took place. As a summary none of the technique used showed inclusion sedimentation during the test protocols.

4.4.2 Linear tests

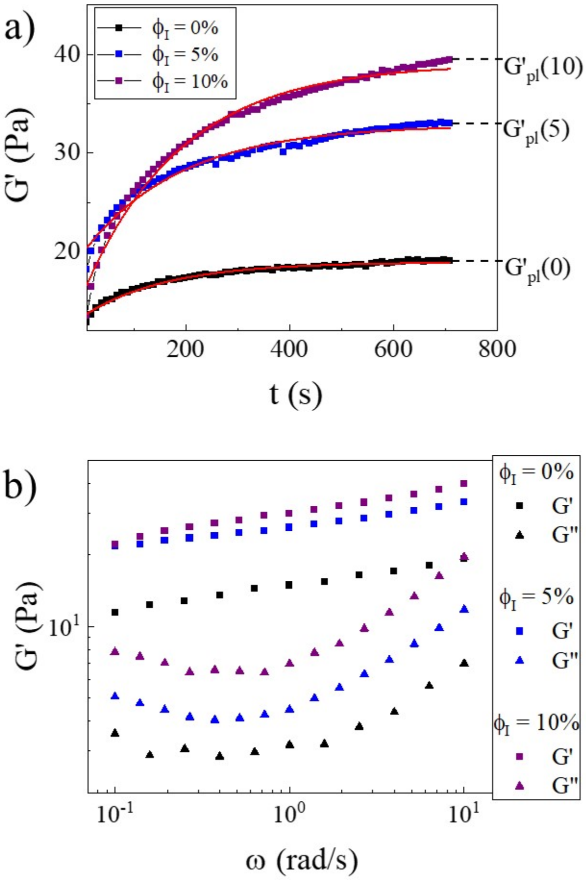

Figure 4.7: Linear properties of weak PMMA gels doped with density mismatched glass inclusions. (a) Second *Block* of the protocol: gel coarsening after rejuvenation for 0, 5, 10% of inclusion as probed by G'. The plateau values of the elastic modulus, G'$_{\text{pl}}$ were used to assess the influence of inclusion fraction on linear properties. The red lines correspond to exponantial fits performed in order to compare the gel structuration properties as a function of inclusion fraction. (b) Dynamic frequency sweeps corresponding to *Block 3* of the protocol, for several inclusion fractions.

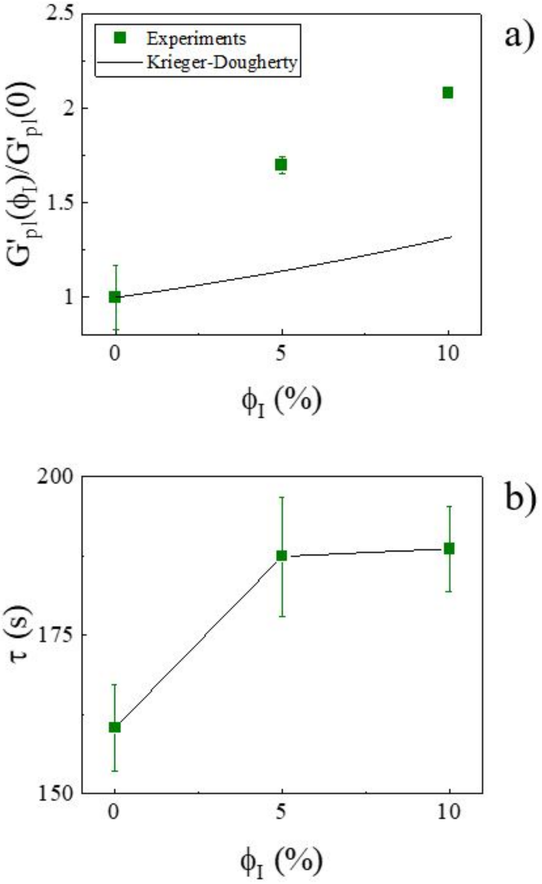

Figure 4.8: Linear properties of weak PMMA gels doped with density mismatched glass inclusions. (a) Reduced plateau elastic modulus as a function of inclusion fraction. The trend for experimental points is up to 1.6 higher than predicted by the Krieger-Dougherty model. (b) Characteristic time obtained by an exponential fit of the dynamic time sweeps, for the three inclusion fractions.

Fig. 4.7 a) displays the increase of the elastic modulus over time following the pre-shear step, as a function of inclusion volume fraction ϕ_I. The plateau value of the elastic modulus ${G'}_\mathrm{pl}$ following pre-shear and recovery increases when the inclusion fraction is increased. From the last dynamic frequency sweep step, the elastic modulus is shown to be an increasing function of the inclusion fraction for all considered frequencies, fig. 4.7 b). Fig. 4.8 a) displays the normalized equilibrium elastic modulus as a function of inclusion fraction, that is the elastic modulus per inclusion divided by the elastic modulus of the undoped gel. We compare the evolution of the normalized equilibrium elastic modulus as a function of the inclusion fraction ϕ_I with the Krieger-Dougherty prediction [99] for the evolution of properties of yield stresses loaded with density matched inclusion, see section 2.2.2. The increase of the normalized elastic modulus with an increase in the inclusion fraction is at the most a factor 1.6 higher than what the Krieger-Dougherty law predicts. A similar discrepancy is obtained when using the elastic modulus from the dynamic frequency sweeps in fig. 4.7 b).

Furthermore, the characteristic recovery time of the elastic modulus following pre-shear is studied as a function of ϕ_I. The recovery curves in Fig 4.7 a) are fitted with a good correlation coefficient by an exponential function $G' = B \ e^{-t/\tau} + E$, where B and E are two constants. In fig. 4.8 b) the evolution of the characteristic time τ as a function of ϕ_I is displayed. It shows that an increase in ϕ_I causes an increase in the characteristic recovery time.

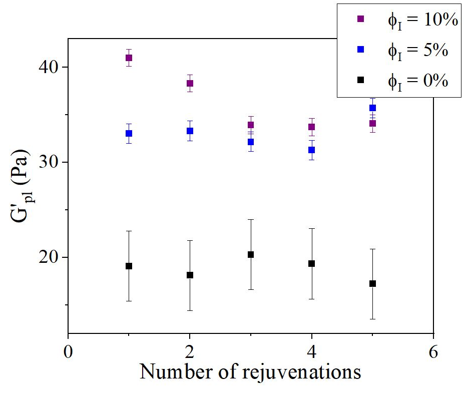

Figure 4.9: Linear properties of weak PMMA gels doped with density mismatched glass inclusions. Evolution of the plateau modulus ${G'}_\mathrm{pl}$ as a function of the number of rejuvenations for different inclusions fractions ϕ_I.

Fig. 4.9 displays the evolution of ${G'}_\mathrm{pl}$ after several repetitions of the test protocol as a function of inclusion content. While ${G'}_\mathrm{pl}$ remains constant for $\phi_\mathrm{I} = 0\%$ and 5%, for $\phi_\mathrm{I} = 10\%$, ${G'}_\mathrm{pl}$ significantly decreases after several rejuvenation steps.

This implies that high concentrations of large inclusions induce an irreversible weakening of the host matrix under shear.

4.4.3 Non-linear tests

Fig. 4.10 a) displays the LAOS tests for three inclusion fractions, at a frequency of $\omega = 1$ rad/s. The first and second strain [90] are faint and no trend can be drawn, regardless of the frequency. Fig. 4.10 b) displays the crossover strain values determined at the crossover of G' and G" from the dynamic strain sweep tests, as a function of the inclusion fraction, for three considered frequencies. The trend of the crossover strain as a function of inclusion concentration is non-monotonical. Lastly, fig. 4.10 c) displays the crossover stress as a function of inclusion fraction, for the three considered frequencies. The crossover stress generally increases as a function of the inclusion fraction, which is more marked when the frequency increases. We also notice that the increase of the reduced crossover stress is higher than what the Chateau's phenomenological model for the reduced yield stress predicts [28], see section 2.2.2, by an increasing factor of the inclusion fraction. Lastly, we see that the homogenization law $\sqrt{(1-\phi_{\mathrm{I}})g(\phi_{\mathrm{I}})}$ [28], see section 2.2.2, using the experimental reduced elastic modulus for g(ϕ_{I}) results in a closer match with the data, especially at a frequency of 1 rad/s.

Strain sweeps and step rates

Moroever, fig. 4.11 a), b), c) depicts step rate tests for the three considered gels at different step rates. For all considered step rates, we report the amplitude of the stress overshoot to be an increasing function of the inclusion fraction ϕ_{I}. The strain corresponding to the stress overshoot also seems to shift towards higher values upon inclusions addition. Fig. 4.12 a) displays the increase of the reduced peak stress as a function of inclusion fraction for different strain rates. The reduced peak stress increase is more marked for higher strain rates, with some fluctuations. Moreover, the increase of the reduced peak stress is higher than the increase described in Mahaut et al. work [99] for the reduced yield stress, by an increasing factor of the inclusion fraction. We also compare experimental results with the homogenization law $\sqrt{(1-\phi_{\mathrm{I}})g(\phi_{\mathrm{I}})}$ [28] using the reduced experimental elastic modulus for g(ϕ_{I}): the match is closer but still smaller than the experimental data. Fig. 4.12 b) displays the increase of the reduced peak strain as a function of inclusion fraction increase, which is less marked for higher strain rates. Other interesting features are displayed in fig. 4.13 a), b) c) each of them displaying the step rate tests at a fixed inclusion

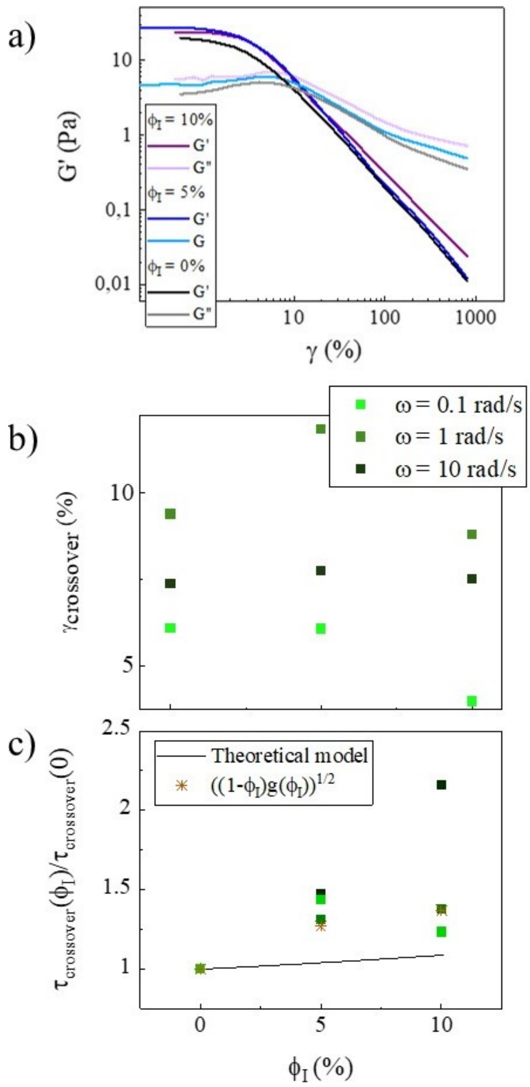

Figure 4.10: Yielding properties of weak PMMA gels doped with density mismatched glass inclusions. a) LAOS at $\omega = 1$ rad/s as a function of the inclusion fraction. b) Crossover strain from LAOS tests as a function of inclusion fraction and angular frequency. c) Crossover stress from LAOS tests as a function of inclusion fraction and angular frequency. Chateau's model for the reduced yield stress is a function of the reduced elastic modulus g(ϕ_I), and is depicted as a black line when the K-D type theoretical expression for g(ϕ) is used, and using brown symbols when the experimental plateau elastic modulus is used.

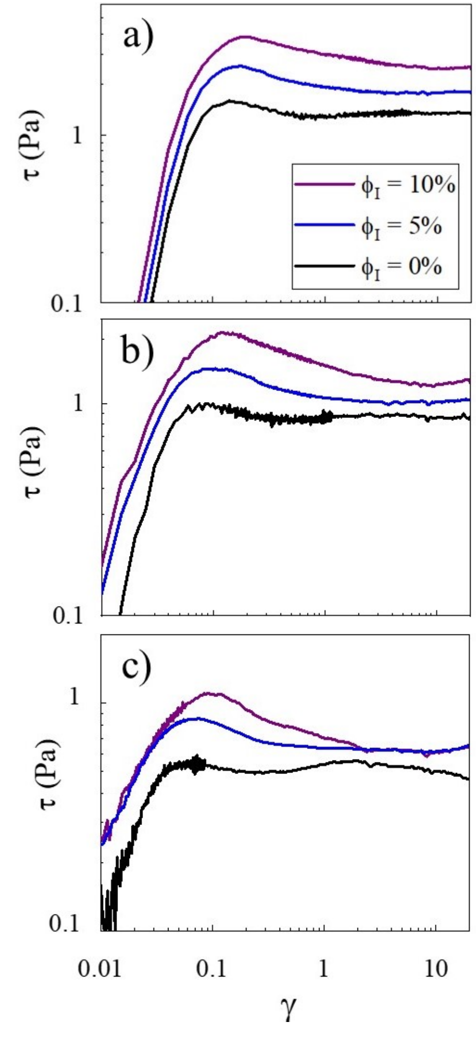

Figure 4.11: Yielding properties of weak PMMA gels doped with density mismatched glass inclusions. Step rate tests at shear rates of a) 2 s^{-1}, b) 0.5 s^{-1}, c) 0.05 s^{-1}.

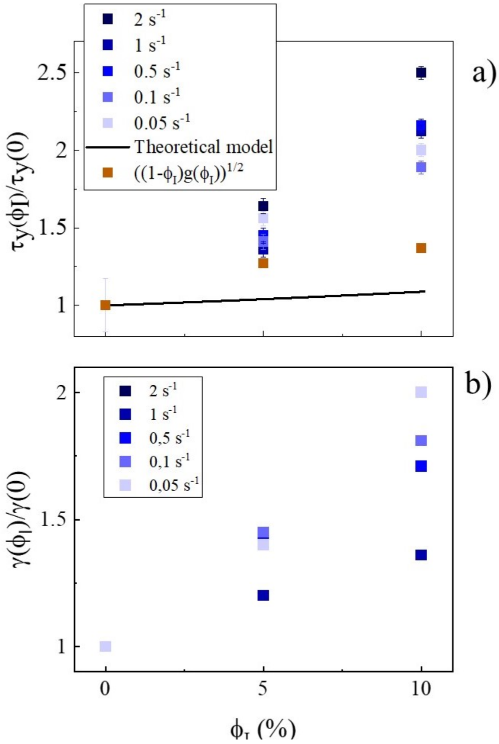

Figure 4.12: Yielding properties of weak PMMA gels doped with density mismatched glass inclusions: step rate tests. a) Reduced peak stress, experimental data extracted from the stress overshoot at rates of 2, 1, 0.5, 0.01, 0.05 s^{-1}. Chateau's model for the reduced yield stress is a function of the reduced elastic modulus g(ϕ_{I}), and is depicted as a black line when the K-D type theoretical expression for g(ϕ) is used, and using brown symbols when the experimental plateau elastic modulus is used. b) Reduced peak strain, experimental data extracted from the stress overshoot at rates of 2, 1, 0.5, 0.01, 0.05 s^{-1}.

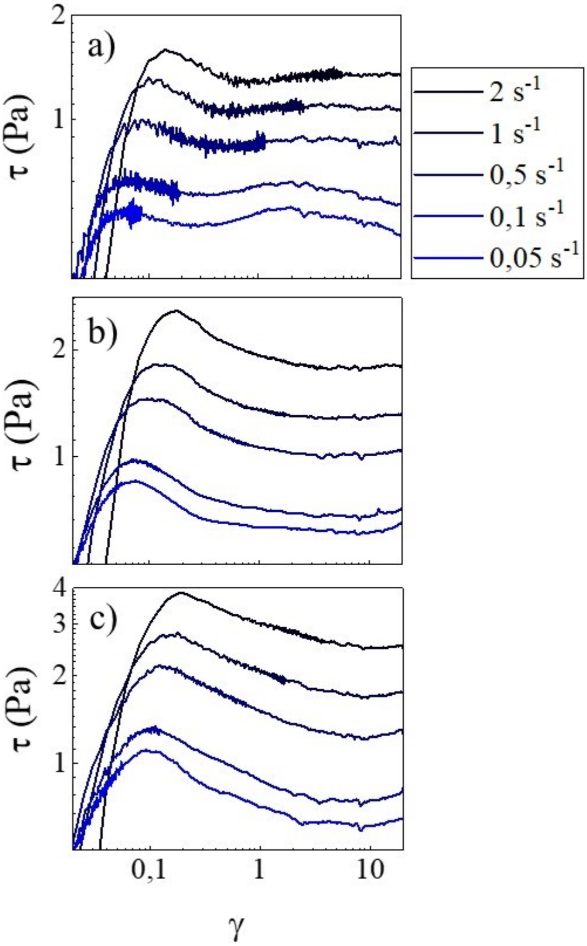

Figure 4.13: Yielding properties of weak PMMA gels doped with density mismatched glass inclusions. Step rate tests at various strain rates for a) $\phi_\mathrm{I} = 0\%$ b) $\phi_\mathrm{I} = 5\%$ c) $\phi_\mathrm{I} = 10\%$.

fraction, at different strain rates. We report a deepening and broadening of the overshoot peak, with a shoulder feature in c) for an increased inclusion fraction. Moreover, although two yielding peaks are seen for the bare gel, the second yielding peak is absent for the inclusion loaded samples, while a second rise in the shear stress can be noticed for large strains: if existing, the second yielding peak seems to be notably shifted in strain values, for inclusion loaded samples.

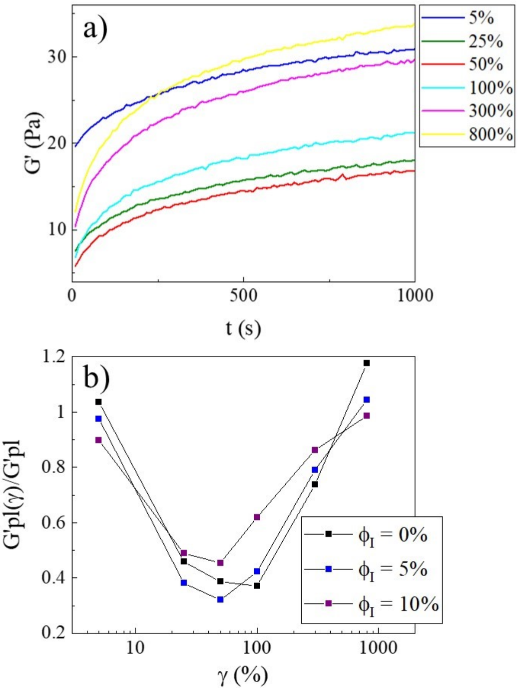

Figure 4.14: Pre-conditioning tests for the 10% inclusion sample. a) Dynamic time sweep following the pre-conditioning step for different pre-conditioning amplitudes. The plateau linear modulus is taken as the value of linear modulus at the end of the time sweep. b) Scaled plateau linear elastic modulus as a function of the pre-conditioning amplitude for three inclusion fractions.

Pre-conditioning tests

In fig. 4.14 b), the time sweeps following the pre-conditioning steps for the 10% inclusion content are displayed. Upon increasing the pre-conditioning strain, the equilibrium elastic modulus first decreases and reaches a minimum value G'_{min} at a strain γ_{min}, then increases again. This is similar to observations by Moghimi et al. [109] for the bare gels. In fig. 4.14 b), the evolution of the equilibrium modulus is displayed as a function of the inclusion fraction. The shape of the reduced elastic modulus curve as a function of pre-conditioning amplitude is similar for all inclusion content. γ_{min} is lower for the doped samples than bare gels.

4.5 Discussion

With regards to the linear properties of our system, we observe a steeper increase of ${G'}_{\mathrm{pl}}$ with ϕ_{I} as compared to the K-D prediction [99, 28]. This cannot be explained by modifying the value of the maximal packing fraction [126, 3, 69], see section 2.2.2, hence taking into account beads polydispersity [3] or shear induced anisotropy [126], as the K-D function is not modified by a change of the maximal packing fraction from $\phi_{\mathrm{m}} = 0.57$ to 0.6 in the studied inclusion fraction range. One assumption of the K-D model is the absence of physical or chemical interaction between the inclusion and the matrix [28]. However, for our system, depletion interactions at the inclusion' surface might take place, with a different attraction strength: the inclusions are indeed 25 times bigger than the colloidal spheres and can be modeled as a wall to which the beads would aggregate [20, 131] as depicted in fig. 4.15. Such interactions are stronger than between spheres as the excluded volume provided by the wall is bigger [131]. We can then assume that the high strengthening of our gel upon inclusions addition can be attributed to a strong cohesion between the matrix and the inclusion, due to depletion interaction at the inclusion's surface.
With regards to the non-linear properties, the influence of the inclusions fraction increase depends on the definition taken for gel yielding: the crossover strains from LAOS are insensitive to inclusions addition but the amplitude of the crossover stress from LAOS, stress overshoot and associated strain from the step rate tests increases with increasing inclusion content. The increase of the crossover stress and the stress overshoot amplitude as a function of the inclusion volume fraction is again linked to the increase of the reduced elastic modulus with an increasing inclusion volume fraction [28]. The fact that the increase of experimental reduced stresses increase upon inclusion addition is steeper than what predicts the theoretical model from Chateau et al. can be attributed to the strong cohesion of the gel with the inclusion as discussed for the experimental reduced elastic modulus. It is worth noting that the homogenization law [28] for the reduced yield stress using our experimental reduced elastic modulus provides with a closer match with experimental reduced crossover or peak stress. The steeper increase of the reduced crossover stress at higher oscillation frequencies may indicate that the crossover stress value depends on whether a steady state of the gel structure was reached for all experimental points. The steeper increase of the reduced peak stress for higher strain rates can be explained by a similar arguments [90]. According to the step rates profile, the yielding is not sensitive to inclusion-colloid breakage on one side, intercluster bond breakage on the other side [90], the information is averaged in the overshoot peak. Looking only at the yielding stress it is unclear whether the inclusions contribute to intercluster bonds or are nested in clusters, an information that only microscopic experiments or Brownian

dynamics simulations [88] can provide. The broadening and deepening of the stress overshoot peak upon inclusion addition can be attributed to a more gradual breakage of the intercluster bonds and of the cluster/inclusions bonds. In order to understand the increase upon inclusion addition of strains associated to the peak stress overshoot to higher peak strains, we refer to the existing theory by Chateau et al. [28], which states strain rate localization due to the presence of inclusions. For a given macroscopic strain rate, the inclusions act as a "dead volume" and the strain rate applied on the interstitial matrix increases. This suggests as in Kogan et al. [85], strain localization between the inclusions, and therefore that the yielding macroscopic strain should decrease upon inclusion addition. Our outstanding result, may result from a competing effect between strain localization and network cohesion at the inclusion surface. Furthermore, the smaller reduced peak strain increase at higher strain rates may be attributed a more efficient dislocation of the network at higher strain rate, including the gel-inclusion bonds, which may decrease the overall contribution of the matrix-inclusion interactions. The shift of a possible second yield strain at higher strain values could be attributed to a higher flexibility of the gel network upon inclusion addition.

With regards to the influence of inclusions on the gel structuration kinetics, we report that the presence of inclusions increases the time required for the formation of an equilibrium structure. This feature is not only linked to the higher final moduli at higher volume fraction as more crowded gels form quicker due to lower free volumes and smaller characteristic diffusion time before colloids form bonds. The presence of inclusions decreases the free volume, the inclusion contribute to the network through bonds but doesn’t diffuse in the network. It may thus be that the inclusions delay the formation of a strong structure spanning network due to the local shear exerted around the inclusion during gel coarsening.

As for the pre-conditioning tests, the effect of inclusions on the system rejuvenation under different strain values is minor within the studied inclusion range. The shift of the critical pre-conditioning amplitude γ_{min} upon inclusion addition is an interesting feature that might indicate that the presence of density mismatched inclusions, translated to an additional stress on the matrix, might enhance the breakage of intercluster bonds [109] and mediate the formation of a stronger equilibrium structure for lower shear amplitudes. However this phenomenon would require more extended studies to be validated. Further imaging at the colloidal level would provide interesting insights on the mechanisms at stake.

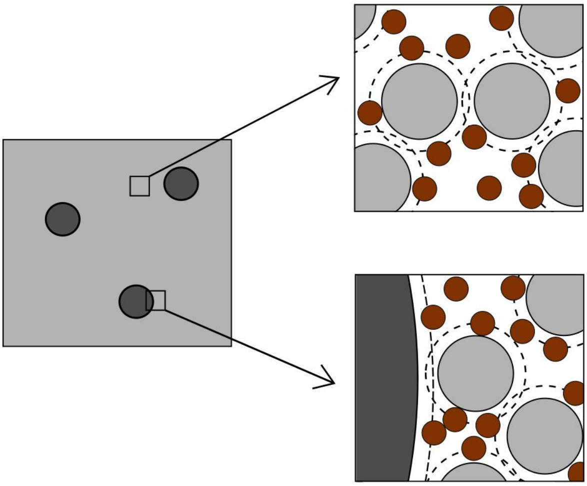

Figure 4.15: Magnification of the colloidal suspension and the colloidal suspension at the vicinity of the wall. Upper figure: inspired by fig. 2.15, the depletion attractions between colloids are represented. The coils of linear polymer chains are modeled by brown disks. The depleted zones around the grey colloids, where the centers of the disks cannot penetrate, are depicted by a discontinuous line. Lower figure: also inspired by fig. 2.15, the depletion interactions at the wall between colloids and the inclusion is depicted. A depleted zone is depicted around the inclusion, depicted in darker gray than the colloids.

4.6 Conclusions and outlook

In this chapter, we investigated the influence of large inclusion with a low density mismatch on the linear, non-linear and recovery properties of model depletion gel composed of attractive nanometric spherical colloidal particles.

As a conclusion of this study we state that an increased inclusion content slows down the formation of an equilibrium structure. Moreover, for $\phi_\mathrm{I} = 10\%$, the elastic modulus decreases irreversibly after 4 rejuvenation steps. Increasing the inclusion fraction in a gel of attractive colloidal spheres induces an increase of the equilibrium elastic modulus. The deviation from the phenomenological Krieger-Dougherty type model may be attributed to depletion interactions at the inclusions' surface.

The non-linear properties of the gels are also influenced by inclusion fraction increase. LAOS tests indeed evidence an increase of the crossover stress that is steeper for higher oscillation frequencies, while step-rate tests evidence an increase of the overshoot stress that is steeper for higher strain rates with an increased inclusion content: depending on the frequency or step rate, the structure may not have reached a steady state before yielding. The increase in the reduced crossover stress as well as the peak stress with increasing inclusion fraction is higher than what is predicted by the phenomenological homogenization model. We attribute this behavior to the physical interactions between colloids and inclusions at the inclusion surface. Moreover, the step rate tests show that upon addition of inclusions, there is a shift from a two step yielding behavior to yielding profiles displaying a broader first peak and potentially a shift of a second peak at larger strain values. Assumptions of a more gradual breakage of the structure for a higher inclusion content, and a higher network flexibility upon inclusion addition need to be complemented by imaging. Lastly, pre-conditioning tests evidence that the role of inclusions on the structure recovery under shear is not minor in the studied inclusion range.

4.7 Acknowledgments

Prof. G. Petekidis is acknowledged for the fruitful collaboration and the opportunity to carry rheological experiments on the system of attractive PMMA spheres in the FORTH Polymer & Colloid Science group as part as a Distruc secondment. Dr. E. Moghimi is acknowledged for the scientific collaboration, and Mohan Das and Antonis Mavromanolakis for the technical support.

Chapter 5

Critical sinking stress of disks through a foam

5.1 Introduction

Foams are present in many consumer products such as foods [169] and detergents [117]. They are also widely studied from a theoretical viewpoint as an example of complex jammed fluids [19] that, depending on the applied stress, behave as elastic fluids, while they display a plastic yielding towards viscous behavior. Thus, they can be described by visco-elasto-plastic models [42, 29]. Spherical inclusions suspended in foams can be found in different applications, for instance to design food mousses with innovative textures, or spheres flotation in industrial processes [37]. The so-called Stokes experiment [21, 36], that consists in letting a circular probe fall in a foam in a two or three dimensional design, is also of fundamental interest as it allows to assess the domain of validity of the visco-elasto-plastic model [29] and the mechanism of yielding of a foam by a heterogeneous shear profile.

The yielding or stabilization process of inclusions by foams is highly dependant on the characteristic bubble to particle size ratio. When the foam bubbles are small with respect to the probe, the matrix can be considered as a continuum and general knowledge on inclusions sinking in yield stress fluids [17] can be used to predict inclusion stability and to derive an expression for the average drag force [72]. Therefore, the continuum approximation allows for an experimental determination of the yield stress, using inclusions stability in the bulk foam or at the foam interface [95], as the yield stress can be approximated by the critical inclusion mass at which sinking at a foam interface occurs. Such values can be compared to a rheometrically obtained yield stress for foams, such as the dynamic yield stress from zero shear extrapolation of flow curves, LAOS tests [34, 139], or curve inflection techniques [163].

For intermediate inclusion to bubble ratio, sedimentation mechanisms are affected by bubbles characteristics and interstitial fluid nature. The drag force indeed decreases when bubble size increases [45] and negative wakes associated with elastic effects [110] are more marked for dry foams [29]. Contrarily to the large yielded region picture in the continuum case, Cantat et al. showed that plastic yielding of foams is restricted to some bubbles layer below the inclusion [21].

While yielding a yield stress fluid interface with spheres of fixed frontal area requires the use of many materials of increasing density, a practical option is to stack disks of the same frontal area at the yield stress fluid interface. It is then an open question whether the sinking behavior of large disks in real, complex milk foams can be correlated with yield stress rheological measurements. In that case a critical yield number of a disk on top of a generic foam could be provided. However, if the fluid microstructure influences the sinking behavior, we need to investigate whether each different type of foam would have a characteristic critical yield number.

Here we report an investigation of the stability of hydrophilic stacks of disks at the interface of milk foam for a bounded experimental setup within a fixed experimental time frame. Although the stability of non-buoyant spheres in yield stress fluids considered as a continuum has been extensively studied experimentally [149, 134, 107] and numerically [17, 58], the literature on stability of complex shaped inclusion in yield stress fluids is scarce. Cylinders with circular section with respect to the flow have been more studied [152, 79, 127] than their counterparts with square cross sections. The two dimensional yielded regions for a square [118] and for a rectangle [25] were mapped using computer simulations. An experimental approach to derive the stability criterion of buoyant disks and cylinders of varying height to diameter ratio from plastic drag coefficients was presented by Jossic et al. [77]. Ahonguio et al. presented further theoretical developments and data for slender disks [1] and mapped the corresponding yielded regions. They found that the stability criterion is nearly constant for height to diameter ratio smaller than one [78] and smaller than for spheres [78, 1]. The sinking mechanism of a non-buoyant disk at a Newtonian fluid interface has been shown to depend on the disk hydrophobicity. Sinking therefore occurs for higher critical masses due to interfacial effects [144], which has to be taken into account when assessing the yield stress from sinking tests. However, the sinking mechanism of non-buoyant inclusion at the interface of yield stress fluids has not been studied in depth. For spheres set on a foam, the critical spheres parameters for which sinking occurs has been linked to the

yield stress [95] and correlated with rheological measurements. As working with disks is more practical and controlled than working with spheres, we choose to study in this work disk stacks set on foams.
In this work, we test the continuous matrix approximation and correlate critical stresses derived from the onset of disk sinking from the top of a foam surface with apparent yield stresses obtained by rheometric vane tests. In this scope, we probe foam of different heights, for two foams types which differ in liquid fraction and interstitial fluid composition.

5.2 Theory

In this section, we first introduce the relevant theory on the stability of disks and cylinders immersed in yield stress fluids. Then, we explain how calculate the critical sinking stress.

The stability of a disk or cylinder of radius R and height h can be predicted using the dimensionless yield number [17, 1], see section 2.2:

$$Y = \frac{F_\mathrm{Y}}{F_\mathrm{I}} = \frac{S\tau_\mathrm{Y}}{\Delta\rho V g} = \frac{\Pi R^2 \tau_\mathrm{Y}}{\Delta\rho \Pi R^2 h g} = \frac{\tau_\mathrm{Y}}{\Delta\rho h g} \tag{5.1}$$

where F_Y is the yield force defined in section 2.2.1, F_I the inclusion force, $\Delta\rho$ the density difference, V the cylinder volume, g the gravitational constant, and τ_Y the yield stress.

In the scope of the experimental procedure described by Jossic et al. [78, 1] the maximum drag force F_dp exerted on the inclusion is equal to the critical buoyancy force $F_\mathrm{I,crit}$. Contrarily to eq. 5.1, the triplet $(\Delta\rho, h, \tau_Y)$ has a critical value. In the case of a yield stress fluid of known yield stress τ_Y, that would imply using the notations $\Delta\rho_\mathrm{crit}$ and h_crit, as explained in section 2.2.1. We however drop the index "crit" here for the sake of clarity. The critical yield number, Y_crit, that is defined as the ratio of the yield force by the critical buoyancy force that marks the onset of inclusion viscous motion in the yield stress fluid, see section 2.2.1, can thus be expressed as a function of the plastic drag coefficient C_dp [105, 1, 133]:

$$F_\mathrm{dp} = F_\mathrm{I,crit} \iff C_\mathrm{dp}\Pi R^2 \tau_\mathrm{Y} = \Delta\rho \Pi R^2 h g \iff C_\mathrm{dp} = \frac{\Delta\rho h g}{\tau_\mathrm{Y}} \tag{5.2}$$

where F_{dp} is the plastic drag force and C_{dp} the plastic drag coefficient. From eq. 5.2 it follows that:

$$Y_{\mathrm{crit}} = \frac{1}{C_{\mathrm{dp}}} \tag{5.3}$$

The h/2R range of the critical disk stacks associated to foam yielding in our experiments ranges from 0.15 to 0.4. In this range, the experimental plastic drag coefficients from Jossic and Ahonguio's studies are constant at fixed inclusion mass [78, 1]. The relevant stability criterion is therefore constant and we take $\mathrm{Y}_{\mathrm{crit}} = 0.1$.

We now discuss Jossic and Ahonguio's critical yield number for an adhesive sphere [78]. Similarly to what was discussed above for cylinders, and using Jossic's convention for the drag surface of a sphere [78]:

$$F_{\mathrm{dp}} = F_{\mathrm{I,crit}} \iff C_{\mathrm{dp}}\Pi R^2 \tau_{\mathrm{Y}} = \frac{4}{3}\Delta\rho\Pi R^3 g \iff C_{\mathrm{dp}} = \frac{2}{3}\frac{\Delta\rho(2R)g}{\tau_{\mathrm{Y}}} = \frac{2}{3}\frac{1}{Y_{\mathrm{max}}} \tag{5.4}$$

where $\mathrm{Y}_{\mathrm{max}}$ is the stability criterion used by Jossic et al. [78]:

$$Y_{\mathrm{crit}} = 3 * Y_{\mathrm{max}} = \frac{2}{C_{\mathrm{dp}}}. \tag{5.5}$$

The resulting critical yield number is equal to 0.17, which is 1.2 higher than Beris et al. prediction for spheres under no-slip conditions [17, 148]. This discrepancy is attributed to elastic effects by Fraggedakis et al. [58]. We therefore decide to use a corrective factor of 1.2 to account for elastic effects and to facilitate comparison with Beris et al. predictions. Ultimately, the critical yield number used for cylinders in the described h/2R range is $\mathrm{Y}_{\mathrm{crit}} = 0.1/1.2 = 0.083$.

In the previous paragraphs, we detailed the calculation of the relevant critical yield number for disk stacks of small height, with square section orthogonal to the flow. We know give the formula used to calculate the yield stress of a yield stress fluid, knowing the critical mass m_{crit} of the cylinder that marks the onset of motion, and the value of the surface orthogonal to the flow, and the frontal area S.

$$Y_{\mathrm{crit}} = \frac{S\tau_{\mathrm{Y}}}{m_{\mathrm{crit}}g} \iff \tau_{\mathrm{Y}} = \frac{m_{\mathrm{crit}}g}{Y_{\mathrm{crit}}S} \tag{5.6}$$

5.3 Materials and methods

5.3.1 Sample preparation

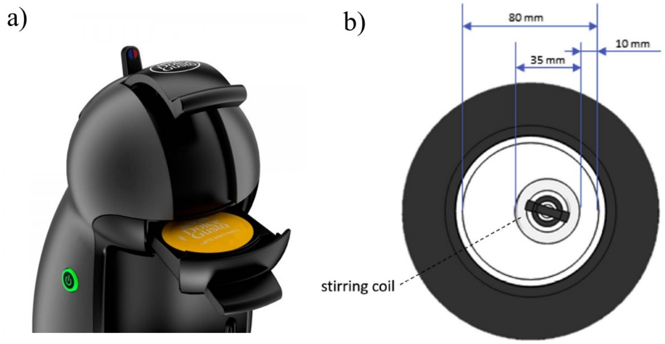

Figure 5.1: Foaming machines. a) Example of NDG machine with a capsule. Adapted from NDG website. b) Sketch of Aeroccino foaming device, top view displaying the stirring coil. Adapted from Völp et al. [158].

The production of the probed foam relies on two different foaming techniques, capsule extraction for foam A and whipping for foam B.

Milk foams of type A were prepared by extracting with an NDG machine, see fig. 5.1 a), commercially produced whole milk powder capsules (Nescafé Dolce Gusto, NDG, provided via Nestlé Research, Switzerland) and mineral water containing 255.7 mg/L monovalent ions and 234 mg/L divalent ions, Ca^{2+}, Mg^{2+}. The extraction involves an initial step of powder dissolution within the capsule by injection of hot water (T = 85°C). This step creates a coarse foam by mixing the air and the powder within the capsule, with the injected hot water. The coarse foam is then turned into a fine foam when passed through the capsule fine outlet. At the foaming temperature, the proteins contained in the foam's interstitial fluid phase aggregate and form a weak gel [153, 46]. Milk foams of increasing heights were prepared by extracting several capsules and only keeping the foam part of the beverage.

Milk foams of type B where prepared by dispersing 15 g of a commercially produced milk powder (provided via Nestlé Research, Switzerland) in 100 mL of MilliQ water. Warm foaming was done using an Aeroccino commercial whipping device (Nespresso Aeroccino 4, Nespresso S.A., Lausanne, Switzerland), see fig. 5.1 b). The device is designed to heat up the sample while whipping, and stop the whole process once the temperature in the liquid milk reached 60°C.

Foams of different heights were obtained by pouring different volumes of foamy liquid in the measurement beaker, 100mL, 150 mL, 200 mL and 225 mL. The foam height was then measured with a ruler.
For both foams, the average bubble diameter 1 minute after foam creation is in the order of 0.3 mm.
A milk solution to calibrate interfacial forces was prepared by mixing 15 g of commercially produced milk powder with 150 g of mineral water containing 255.7 mg/L monovalent ions and 234 mg/L divalent ions, Ca^{2+}, Mg^{2+}, at 60°C until complete dissolution.

5.3.2 Test setup

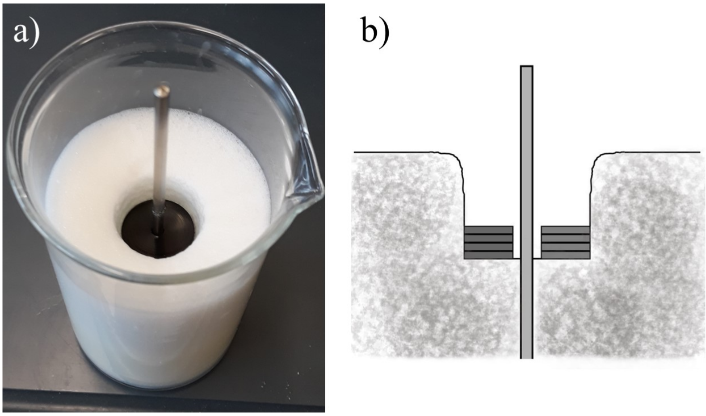

Figure 5.2: Sinking disk in the foam. a) Upper view of a stack of black disks falling in a white milk foam. The foam is placed in a specifically designed beaker equipped with a centering rod glued to the bottom of the beaker: the disks are therefore well centered and stacked on the foam. b) Sketch illustrating the "Side view" of the stack of disks sinking in the foam along the centering rod.

Fig. 5.2 a) displays the test beaker, 250 mL, VWR, that was specifically modified at the Nestlé Research workshop for the disk sinking tests. A 3 mm large centering rod is tightly set at the bottom of the beaker, which ensures that the disks are properly stacked and are set on the foam at a repeatable contact angle. No significant friction of the disks of the rods was noticed during the tests.
Custom black polyoxymethylene (POM) disks of height 1 mm and diameter of 20 mm with a concentric hole of 3 mm of diameter were designed at the Nestlé Research workshop. The size of the disks is a compromise between a

small enough diameter to limit piston effects and a large enough size to easily see the disk on the foam and its interface. We expect piston effects to have neglectible effects on the foam's yielding by disks set on its surface. The surface of the disks is rather hydrophilic, with a contact angle on a flat POM surface estimated to be 66° in literature [11]. For high foam strength, stainless steel disks of controlled mass and dimensions were stacked on POM disks. The overall critical disk stacks height therefore ranges roughly from $h/2R = 0.15$ to 0.4. The milk foams density is approximated by taking into account that the jamming density if of $\phi = 64\%$. The upper bound for the milk foam density is therefore less than one third of water density so 0.26 mg/mL. As the density of POM is 1.412 mg/mL, the buoyancy force is obtained from the weight by applying a corrective factor $\Delta\rho/\rho_{\mathrm{I}}$ equal to 0.82%. The size ratio of the POM disks diameter with regards to bubbles diameter is $d/l = 67$. The size ratio of the single POM disk height with regards to bubbles diameter is $h/l = 3$ and the size ratio of the POM disk critical heights ranges from $2R/l = 17$ to 27.

The vane rheometry tests were carried out with an unmodified 250 mL VWR beaker.

5.3.3 Test protocol: disk sinking tests

Both disk sinking and vane rheometry experiment were started after the same foam age.

Disk sinking tests

For the disk sinking tests, one or multiple disks can be deposited on top of one another, so to generate step-wise increasing stress onto the foam. The disks were deposited on the foam near the foam interface to avoid splashing effects first by continuously stacking disks. The procedure was then repeated with a new foam, waiting 20 s in between each disk to ensure the reliability of the critical mass determination. The interfacial forces, see fig. 5.6 a), were calibrated by using the minimum weight for which the interfacial forces are overcome in a liquid of the same composition as the foam. The interfacial stress thus obtained is of 6.2 Pa, which is lower than each measured yield stress from the disk sinking test, but not negligible.

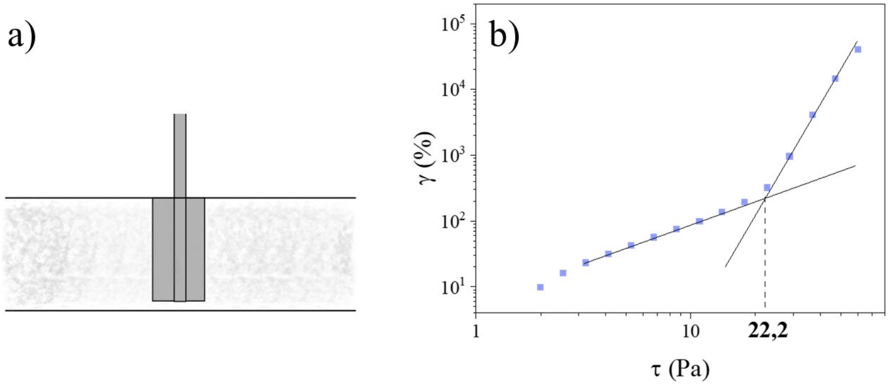

Figure 5.3: a) Four edge vane operating in a foam layer. b) Tangent intersection method for the foam type A, with a foam total height of approx. 22 mm. There is an abrupt change in the slope, and the intersection of the two slopes is taken as a measure of the foam's yield stress.

Rheology

The vane rheometry experiments were performed with an Anton Paar rheometer, Physica MCR 501. The foam was probed directly in the unmodified beaker using a four edge vane upper geometry to avoid slip. The geometry was immersed in the foam 30 s before the beginning of the measurement, at an average depth of 20 mm, see fig. 5.3 a). Shear stress was increased in logarithmically distributed steps, and the apparent yield stress was determined using the tangent intersection method [163], as depicted in fig. 5.3 b).

5.4 Results

5.4.1 Results of the disk settling trials

Fig 5.4 summarizes experimental observations of the stability of disks on top of a generic foam within the experimental timeframe, as a function of increasing disk weights, i.e stacking heights. We identify three distinct behaviors for increasing disk stacking heights: first stability with an undisturbed planar interface as in

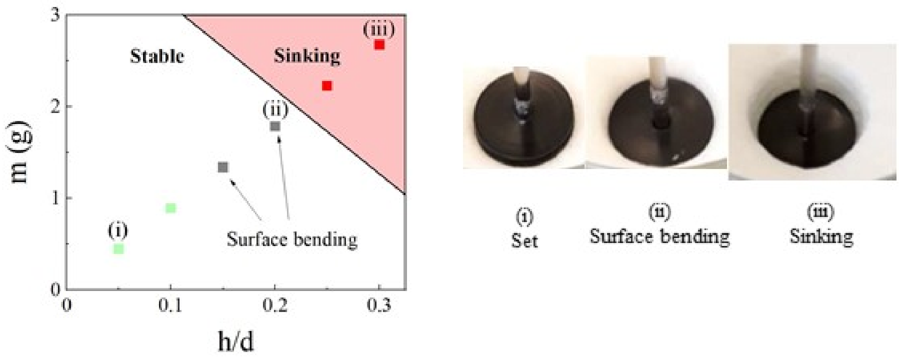

(i) Set (ii) Surface bending (iii) Sinking

Figure 5.4: Stability diagram of the disks of the foam of type A, with a foam total height of 20 mm. The stable and sinking situation are separated by a line, and depend on the probe overall mass, which is a linear function of the stacking height normalized by the disk diameter. On the right of the diagram, three pictures of the disks stacks set on the foam are displayed as a function of their position in the stability diagram. (i) For few disk stacks, the disk stacks are set on a planar foam interface. (ii) For higher stacking the interface gets curved. (iii) Even higher stacking overcome the foam strength, the foam interface breaks up and the disk stacks form tunnel shapes in the foam while they sediment.

(i), then stability with increasing amplitude of interface bending [144], which goes from a slight curvature to a position of the disk below the foam's average interface as in (ii). Lastly for high stacking heights, the foam interface first breaks up and then the disk stack visibly sinks, and the sinking speeds is quicker for heavier, higher disk stacks. The criterion for saying that a given disk stack yields through the foam is that within the experimental timeframe of 20 s, the disks form a tunnel in the foam as in (iii), or even falls through the foam and are covered by the foam's interface.

The disk stacks that are stable on the foam within the experimental timeframe have a gravity stress that does not overcome the apparent yield stress, as explained for inclusions in bulk yield stress fluids in section 2.2.1. The disks that sink in the foam have a total gravity force that overcomes the foam's yield stress. The lower limit of disk stacks that sink in the foam, is used as the critical mass from which the foam apparent yield stress is calculated using eq. 5.6 using $Y_{\mathrm{crit}} = 0.083$. Since it requires both overcoming the interfacial forces and sinking through the foamy material, it can hence be interpreted as the onset of viscous motion through the foam.

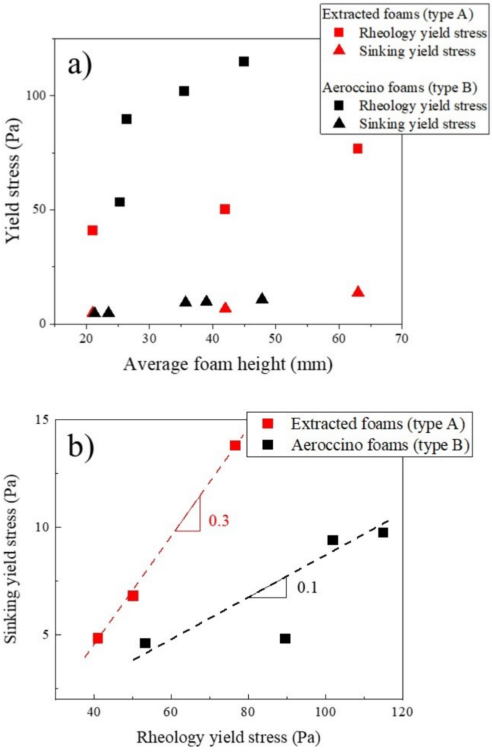

Figure 5.5: a) Sinking and vane rheometry yield stress as a function of foam height, for foam types A (extracted foams) and B (Aeroccino foams). b) Sinking tests yield stress as a function of the vane rheometry yield stress. The two straight lines correspond to foams generated by two different techniques: the red line correspond to foams of type A and the black line to foams of type B.

5.4.2 Comparison of disk settling trials with vane rheometry data

Fig. 5.5 a) displays the sinking and vane rheometry apparent yield stress as a function of foam height for both foam types. For both tests, the yield stress of foams linearly increase as a function of foam height, which can be expected [158]. Differences of correlation of the apparent yield stress determined with the disk sinking tests as a function of the apparent yield stress determined with vane rheometry data are better displayed in fig. 5.5 b). A correlation line of slope 0.3 can be drawn for foams of type A and of slope 0.1 for foams of type B. The foam type dependant quantitative discrepancy between both type of

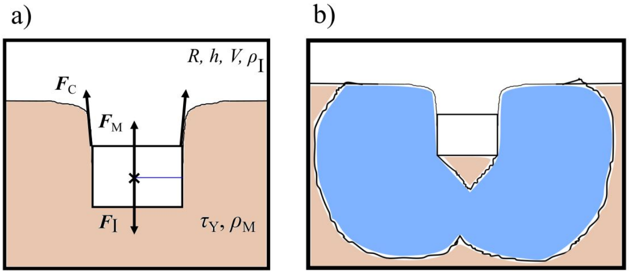

Figure 5.6: a) Forces exerted on a cylinder of radius R, and small height h, volume V and density ρ_I, set at the interface of a yield stress fluid layer, where the yield stress fluid has a yield stress τ_Y and density ρ_M. The cylinder mass is just below the critical mass, according to experimental observations that account for interfacial forces. F_Y is the yield force, F_I the force exerted by the inclusion, F_C the interfacial forces. b) In orange, unyielded yield stress fluid, in blue, hypothetical corresponding yielded region. The sketch is inspired by the experimental shape of the interface prior to disk stack sinking and the theoretical shape of yielded regions for immersed squares and rectangles [118, 26].

measurement techniques suggests that the use of the critical yield number for immersed cylinders of small heights is not seem universal. We therefore attempt to define for each foam type a critical yield number that links the critical sinking mass to the measured vane rheometer yield stress. As depicted in fig. 5.6 a), disk stacks on top of a foam sink through the foam when the effect of the buoyancy force substracted by the interfacial force, overcome the yield force. The use of the buoyancy force rather than the weight is justified by the experimental observation that prior to yielding, the cylinder volume is immersed below the average interface height, as shown in fig. 5.6 b).
Using a graphical approach, the yield force calculated from vane rheometer tests is plotted as a function of the inclusion buoyancy force substracted by the corresponding interfacial force as depicted in fig. 5.7. For both foams, the affine relationship between the two considered forces with a non-zero intercept. Our suggestion for an "on top" critical yield number $\mathrm{Y}_{\mathrm{crit,OT}} = F_Y/(F_{I,crit} - F_C)$, where "on top" relates to the fact that the inclusion is initially set at the top of the yield stress fluid is therefore both foam type and foam height dependant, there is therefore no unique "on top" critical yield number for a considered foam type, as shown in Table 1. However, the slope of the affine function, has the meaning of a corrected $\mathrm{Y}_{\mathrm{crit}}$, and is a characteristic of each type of foam that can be used for relative comparison: 0.3 for the extracted foams and 0.9 for the Aeroccino foams. As a last comment, as shown in Table 1., for foams of type A, $\mathrm{Y}_{\mathrm{crit}}$ varies significantly with foam height. The average value, for information

Type A		Type B	
h (mm)	Y_{crit}	h(mm)	Y_{crit}
21	0.79	21	1.08
42	0.66	36	0.95
63	0.48	39	1.04

Table 5.1: "On top" critical yield number as a function of foam type and height.

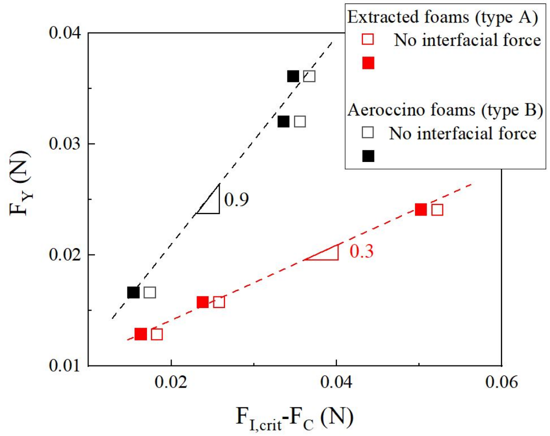

Figure 5.7: Yield force as a function of the critical buoyancy force substracted by the interfacial force. The two straight lines correspond to foams generated by two different techniques: the red line correspond to foams of type A and the black line to foams of type B. The slope of the curves has the meaning of a critical yield number.

purpose only, is of 0.64. In contrast, for comparable height variation, Y_{crit} takes a rather constant value, close to 1 and with an average of near 1.0 and with an average of 1.02 over the 3 values measured.

5.5 Discussion

Using foams of different heights, we showed that the critical mass determined with the sinking tests increases linearly with foam height. Apparent yield stresses determined experimentally with vane rheometry tests also increase linearly with foam height [158]. Theoretically speaking, there indeed exists a yield stress gradient in the foam due to height variation of bubble's characteristic size and liquid contents, and it was shown experimentally that the average yield stress increases with foam height [158]. This validates the linear dependance of the critical sinking mass with the foam yield stress in accordance with literature on spheres sinking onset at foams interface [95] and using a constant critical yield number.

A remarkable feature is thus the correlation between the sinking stress and vane rheometer apparent yield stress, nevertheless the correlation slope appears to depend on the foam type.

There is therefore no universal correlation for inclusions sinking from the top of the foam's surface, using the critical yield number for immersed non-slipping small aspect ratio cylinders in a yield stress considered as a continuum. That implies that the critical sinking stress of disk stacks of small height on a foam relies both on the macroscopic yield stress of the foam and on foams properties. The inclusion to bubble ratios validates the use of the continuum approximation for both foam types. However, due to different foaming processes, foams of type B have a smaller liquid fraction, while foams of type A interstitial fluid contains protein aggregates [153, 46], and is therefore more viscous. This higher interstitial viscosity potentially affects the sinking behavior of large inclusions, and might have an influence on the foam's height dependant structure through bubbles kinetics. The exact influence at fixed rheological yield stress of the aggregation state of the interstitial fluid on the foam's height dependant properties could be an interesting investigation avenue to clarify its influence on the inclusion sinking behavior.

In the absence of an universal correlation, the sinking onset of inclusions at the interface of foams of different types can be compared using the slopes of the affine functions between the yield force and the buoyancy force corrected for interfacial effects. The slopes are respectively 0.3 and 0.9 for foams of type A and B, which suggests that for a fixed vane rheometry apparent yield stress, the buoyancy force required to yield foams of type A, whose interstitial fluid is more complex, is larger than the buoyancy force require to yield foams of type B. As for the experimental values of the newly defined "on top" critical yield numbers $\mathrm{Y}_{\mathrm{crit}}$, the value for foam type B, which is the simplest considered foam, is quite independent of foam height. For foam A, however, $\mathrm{Y}_{\mathrm{crit}}$ decreases for increasing foam height, which may be due to the higher complexity of the interstitial fluid. Although the values of $\mathrm{Y}_{\mathrm{crit}}$ are both foam type and height dependant, their average order of magnitude can however be compared with critical yield numbers for immersed inclusions. For all foams considered, the "on top" critical yield number are higher than the immersed inclusion critical yield number: lighter disk stacks yield through foams than in the immersed setting.

The configuration "on top" potentially plays a large role in this discrepancy. In the immersed case, the yielding of the foam by the inclusion induces the unjamming of a three-dimensional structure surrounding the inclusion. In the case of the inclusion at the yield stress fluid interface, the yielding of the foam is facilitated as the foam "on top" does not contribute to the trapping of the inclusion. This supports the statement that lower buoyancy forces can overcome the yield stress. As depicted in fig. 5.6 b), the amount of foam "on top" is rather small as the interface curvature prior to yielding induces a significant coverage of the disk stacks by the foam, similar to the immersed case. Simulations or dedicated experiments as a function of the ratio of free surface to immersed volume for a model foam or a yield stress fluid with a constant yield stress would help quantify the influence of the ratio of free surface to immersed volume on the unjamming mechanisms. Lastly, the relative amplitude of the interfacial force with regards to the buoyancy force indicates that interfacial forces have a neglectible impact on the discrepancy between $\mathrm{Y_{crit}}$ for foams and $\mathrm{Y_{crit}}$ for immersed object in model yield stress fluids. As a last comment, the different value of the offset of the affine function for foams type A and B, may be an additional "interfacial effect", which amplitude would be larger than the surface tension effects measured. Our assumption is that this additional "interfacial effects" could be attributed to a combination or separate effects of the interfacial elasticity or a qualitative difference in the foam bending behavior, and would increase with the complexity of the interstitial fluid, such as the presence of protein aggregates in foams of type A.

Our results therefore hint at a combined effect of foam type, height and immersion degree dependant unjamming mechanisms on the onset of small cylinders motion from the top at a foam. In order to assess the inclusion geometry dependance of our results, we compare our results to the critical sinking spheres masses at the interface in Le Goff et al. publication, [95]. There, the critical sinking stress is calculated from the critical sinking weight and is four times larger than the yield stress, which is roughly two times lower than in the immersed sphere case using Beris et al. critical yield number $\mathrm{Y_{crit}} = 0.143$ [72, 36], and would be even smaller if we were considering the buoyancy force rather than weight. Although an exact investigation of inclusion geometry is restricted by the foam dependance of correlations, this validates the fact that for a generic inclusion on top of a foam, the critical yield number is higher than in the immersed case. Lastly, slip effects at the inclusion surface are generally associated to higher critical yield numbers.

5.6 Conclusion

In this chapter, we tested the relevance of the critical yield number for immersed cylinders of small height in the case of hydrophilic disk stacks at milk foams interfaces. Using the critical yield number for immersed cylinders of small height, a critical sinking stress was calculated from the disk stack mass associated to the onset of disk stack sinking through the foams. Using foams produced by two techniques, and of different heights, we showed that both the sinking stress and the apparent yield stress determined by vane rheometry increase linearly with increasing foam height, in accordance with previous work. The correlation between the two types of stresses is satisfactory, however the critical sinking stresses have a lower amplitude than the vane rheometry apparent yield stress, and the correlation is foam type dependant. Experimental "on top" critical yield numbers Y_{crit} are defined for each foam, and are independant of height for the simplest foam only. Foams of different types can however be compared according to the slope of the affine function of the yield force as a function of the critical buoyancy force substracted by the interfacial force. The higher magnitude of the Y_{crit} with regards to the Y_{crit} suggests that lower cylinder masses yield the foam than in the immersed case, which may be explained by the greater ease to unjam the foam in the configuration where the cylinder is on top of the foam. Lastly, complex foam interstitial fluid microstructures seem to induce extra interfacial effects that shift the onset of small cylinders sinking to higher masses. As an outlook, two possible directions of research are relevant to our study. Firstly, studies on the onset of sinking for spheres and cylinders of fixed frontal area on top of model yield stress fluids, would allow to calibrate the influence of the immersion degree dependant unjamming as a function of inclusion geometry on the critical yield number. Secondly, the immersed and interfacial yield region for foams with different yield stress gradient would be of fundamental interest.

5.7 Acknowledgements

Eric Joannet at Nestlé Research and Lionel Walther and Angiolino Del Vecchio at NPTC Orbe are acknowledged for their support of the project. Hélène Deyber is acknowledged for technical support. The NRC workshop is acknowledged for the assistance in design and realization of the centered beaker and the pierced disks.

Chapter 6

Conclusion

In this PhD work, we explored two key aspects of yield stress or highly shear-thinning dispersions containing large inclusions with a density mismatch: inclusion stability against sedimentation and the influence of inclusion on rheological properties. We chose to use model systems that allow for a physical description of the results. We expect that the results can be used to design industrial soft composites, in particular in the area of food applications.

Stability of inclusions in yield stress fluids or highly shear thinning dispersions is traditionally predicted with macroscopic parameters. Nevertheless, the drag enhancement or stabilization properties of anisotropic particles needs to be further investigated. Moreover, phenomenological models for linear and non linear rheology of yield stress fluids doped with inclusion were developed, but however remain to be validated for model gels of attractive colloidal rod-like, or spherical particles. Finally, the validity of the macroscopic stability criterion needs to be assessed for inclusions set on top of yield stress fluids and for different foams types.

In ch. 3, we studied the factors influencing sedimentation speeds of inert inclusions suspended in semi-dilute dispersions of ideal mono-disperse rod-like particles. No apparent yield stress could be identified for the system, although inclusions are quasi-static when combining drag enhancement factors such as high rod concentration, length and low inclusions stresses. We show that the increase of rods concentration induces a strong decrease of the reduced sedimentation speeds. A theoretical prediction relying on the Stokes terminal velocity using zero-shear viscosity for semi-dilute suspension is used to account for the effect of rods length, flexibility and concentration. The predicted concentration dependence is found, and the effect of the rod length is very pronounced so that a two-fold increase in the length of the rod slows down the sedimentation speeds by two orders of magnitude at a fixed concentration. The results for both rod lengths superimpose, however, when scaling the concentration with the overlap concentration. Experimental sedimentation speeds are lower than predicted: there is indeed a constant difference between experiment and theory of a factor 2 and 4 for the shorter and longer rods, respectively. When flexibility is taken into account, the difference between experimental and theoretical values is even larger. We hypothesize that crowding in front of the inclusions, causing an increased viscosity, is not sufficiently equilibrated by translational diffusion of the rods, as suggested by the high values of the experimental translational Peclet. With regards to rod length, we assume that the significant sedimentation speed difference is linked to the density of entanglement between the rods, since both rod systems have equal mesh sizes.

As a summary, we evidenced drag enhancement factors for inclusions in semi-dilute ideal rods dispersion. This provides a reference for drag enhancement effects on inclusions sedimenting visco-elastic fluids such as linear polymer chains or wormlike micelles. The results are also of interest for weak gels composed of fibers, which potentially involve similar reorganisation and crowding front on the inclusions.

In ch. 4, we investigated the influence of the fractions of inclusions on rheological properties of model weakly attractive gels. The reduced elastic modulus was shown to be an increasing function of the inclusion fraction as expected for hard inclusions interacting mechanically with the matrix. The increase is however higher than the usual Krieger-Dougherty homogenization law, which we attribute to depletion effects at the surface of the inclusion that leads to stronger matrix-inclusion interaction and resulting gel strength. Non-linear yielding properties were investigated by LAOS rheometry and step rate tests. Both reduced crossover stress and first peak stress where shown to be an increasing function of inclusion fraction, especially for high shear rates/oscillation amplitudes. We compared the results with the corresponding reduced yield stress homogenization model and noted that it underestimated our experimental data. The two-step yielding feature of the gels was shown to be affected by inclusions content as the first peak broadens, suggesting a more gradual breaking of inter-cluster bonds and the second peak seems shifted to higher values. Structure recovery tests were not significantly influenced by inclusions, which may be linked to the small gravity-induced stresses by the inclusion.

Those results are relevant for real gel systems, where the existence of the network is induced by depletion, or to give keys to understand deviations from the Krieger-Dougherty phenomenological model.

In ch. 5, we studied the factors influencing the critical sinking stress of hydrophilic disk stacks of fixed frontal area at the interface of milk foams. Both critical sinking stresses and vane rheometry apparent yield stresses increase linearly with foam height, when using the critical yield number Y_{crit} for immersed cylinders of small height to calculate the critical sinking stress. However, the correlation depends on the foam type and the correlation factors values are low. Experimental "on top" critical yield numbers $Y_{\text{crit,OT}}$ are defined for each foam, and are independant of height for the simplest foam only. Their magnitude suggests that lower cylinder masses yield the foam than in the immersed case, which may be explained by the greater ease to yield the foam in the configuration "on top" of the foam. Lastly, complex foam interstitial fluid microstructures seem to induce extra interfacial effects that shift the onset of small cylinders sinking to higher masses.
This study is of direct interest for jammed systems such as foams and emulsions with or without a complex interstitial fluid. Practically speaking, the study of disk sinking can be used to discriminate between foams created by the same foaming technique, in the context of quality or product development tests.

As a conclusion of this work, we evidenced drag enhancement parameters for large spherical inclusions in suspensions of colloidal rods. Moreover depletion colloidal gels have outstanding linear and non-linear rheological properties as explained by depletion interactions at the inclusion surface. Lastly, we applied our approach to milk based foams and showed that the sedimentation of large cylinders of small height on top of a foam relies on foam microstructure.

6.1 Outlook

Our results hints to a few possible directions of research.

As an outlook for ch. 3, recently hollow silica rods were developed, which could be used to further understand the dependence on aspect ratio of the discrepancy between experiments and Stokes prediction. The use of fluorescently labeled rods in inclusion sedimentation experiments, would be recommended to directly access to the rods dynamics during inclusion sedimentation. Sedimentation studies of inclusions in suspensions of ideal attractive colloidal rods is an exciting prospect, however the synthesis of thermo-responsive rods has been proved challenging. We therefore recommend grafting alternative stimuli responsive polymers on fd rods to optimize the succesful synthesis thermo-responsive of gels. Our results for visco-elastic shear-thinning suspensions could be then systematically compared to those on gels composed for ideal colloidal rods.

A full rheological characterisation will be required to draw parallels between macroscopic and local flow behavior.

As an outlook for ch. 4, the influence of depletion interactions could be further assessed by varying the interaction and assessing whether this influences the reduced elastic modulus trend. Rheo-imaging and Brownian Dynamics would be useful to further understand the mechanisms at stake. Furthermore, systems of thermo-responsive attractive inclusions were recently studied, and they may be an interesting model material to investigate the influence of inclusions on rheological properties.

Lastly, as an outlook for ch. 5, a study of the sinking onset of inclusion of various shapes and different surface properties such as roughness and hydrophobicity at the interface of yield stress fluids with no yield stress height gradient would be interesting. The effect of interstitial fluid microstructure on inclusion sinking behavior should be studied by using various interstitial fluid gel strength, and varying bubble to inclusion sizes.

As pointed out at the beginning of this manuscript, this PhD research is of wide practical relevance with regards to the shelf-life and process of heterogeneous products. We therefore close this outlook with both a biological and a food science application:

- In the field of biological tissue engineering, suspending cells in three-dimensional extracellular matrices is an interdisciplinary challenge, which success requires a good understanding of the suspending properties of the matrices at both macroscopic and network relaxation level. As a further step, shaping the obtained soft composites into bio-active implants or organ parts via 3D printing requires extensive knowledge on the influence of soft inclusions on linear and non-rheological properties.
- In the field of food science, there are wide perspectives for the design of innovative and health-conscious products within the context of process, shelf-life and mouthfeel. To pick one, the remarkable stabilization properties of anisotropic subunits confirmed their status of low concentration alternative to thickeners relying on crowding. Reformulating products accordingly has the potential to modify flavours perceptions and could lead to a significant decrease in excipient's content.

Appendix A

Pnipam grafting of fd rods: preparation and rheology

A.1 Introduction

In this appendix, the attempt to perform yielding experiments on gels of pnipam-grafted rods is described. First, the grafting trials that were performed to obtain pnipam grafted gels are detailed. Then, preliminary rheological results on the bare gels are presented. Their purpose was to identify a range of concentrations, ionic strengths and temperatures that optimizes the successive recovery of the gel in a short experimental time frame. The wider aim of those tests was to determine the optimal test parameters to carry out stability tests as described in ch. 3, and rheological tests on the inclusions doped gel, as in ch. 4.

A.2 Materials

A.2.1 Samples characteristics

The first batch is composed of fd suspensions grafted with 9k pnipam polymers, prepared in the IBI-4 lab and used in ref. [136]. This batch was used here for the preliminary rheological recovery tests. Due to very limited amount of sample, the synthesis of new pnipam grafted fd sample was initiated.
In these synthesis, the selected polymers were put to react with fd virus dispersed

in a 100 mM phosphate buffer, according to the procedure described by Zhang et al. [166]. When possible, polymers of length close to 10 k were selected in order to obtain pnipam grafted fd suspensions similar to the reference publications, where 7k [166] and 9k [136] long chains have been respectively grafted on viruses. The second batch is composed of fd suspensions that reacted with N-hydroxylsuccinimide (NHS) ester terminated 10k polymers purchased from Polymer Source. The third batch is made from fd suspensions that reacted with (NHS) terminated 2k pnipam chains purchased from Sigma-Aldrich. Lastly the fourth batch is made from fd suspensions that reacted with 10k TFP terminated pnipam synthetized at IESL-FORTH in Prof. Vamvakaki group by Dr. L. Chambon.

A.2.2 Validation of the grafting procedure

We applied several techniques to validate if the grafting procedure described above was successful, as described below.

Birefringence

Rectangular capillaries, which specifications are indicated in section 4.3.3, are filled with the solutions obtained after the grafting process, at an ionic strength of 100 mM and a rods concentrations of $c = 18$ mg/mL. Birefringence of the suspension is assessed with a polarizing microscope first after capillary loading and then after one night. For this ionic strength and concentration, fd solutions are expected to be isotropic whereas pnipam grafted fd solutions are expected to be nematic due to the larger volume per particle [166]. Birefringence thus indicates a successful grafting of the viruses with pnipam.

AFM imaging

AFM studies of the fd samples having reacted with the 2k polymers, *batch 3*, were performed in the Physics Department of KU Leuven by Dr. O. Deschaumes.

A.2.3 Gel formation and characteristics

Once grafting of the rods has been established, it needs to be established if the systems actually form a gel. Several ways to establish gelation are described below.

Figure A.1: Vial turning technique for a batch of successfully grafted fd-pnipam.

Vial turning technique

A reaction vial with grafted rods is heated in an oven for 1h at a temperature of 40 ° C. The vial is then tilted and gelation is evidenced when the system remains in the bottom of the vial, as in fig. A.1. This technique is especially accurate for strong gels that easily sustain their weight but needs to be complemented by more precise tests to probe weak gels such as rheology, dynamic light scattering, or inclusions sedimentation monitoring, see below.

Microscopic imaging

Rectangular capillaries are filled up with a mix of fd-pnipam and inclusions, as described in section 4.3.3. The capillary is inserted in the setup described in section 3.3.1 and put in contact with a commercial transparent heating sheet purchased from Minco, which temperature calibration was performed with an infrared camera, Testo 890. Inclusion sedimentation is imaged during the heating up of the capillary from 25 ° C to 40 ° C. A transition from a sedimenting behavior to an arrested behavior indicates that the matrix is a thermo-responsive gel.

Dynamic light scattering

Dynamic light scattering experiments are performed in Jülich, IBI-4 at temperatures of 25 °C then 40 °C. For thermo-responsive gels, the auto-correlation fuction $g_2(0) - 1$ decreases above the critical temperature as the dynamics freezes [166], as displayed on fig. A.2 .

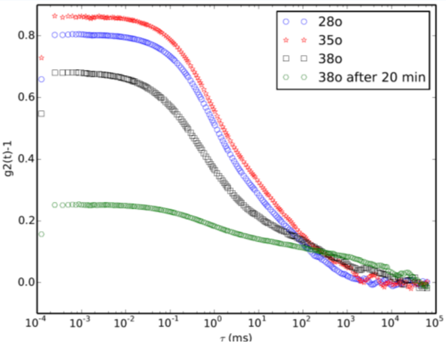

Figure A.2: Auto-correlation functions $g_2(0) - 1$ as obtained by DLS for a fd-pnipam at the indicated temperatures. The relaxation of $g_2(0) - 1$ slows down when the gelation temperature is reached.

Rheology

Macro-rheological measurements were performed on a strain-controlled TA instruments rheometer, equipped with a smooth cone-plate geometry and a Peltier heating system. The cone-plate is equipped with an oil trap to prevent evaporation during the high temperature tests.

Gelation
The gelation temperature is assessed by gradually warming up the solution from 25°C to 40°C at steps of 1°C and carrying out dynamic frequency tests at 10 % strain for each temperature. Gelation is evidenced if the elastic modulus is higher than the viscous modulus at all frequencies. [136]

Recovery tests
Experiments were carried out on *batch 1* for the following ionic strength (mM) concentration (mg/mL) doublets: (100;6) to probe a "strong gel", (100;3) and (10;3) to probe "weaker gels". The first tests were carried out 4° C above the gelation temperature [136, 137], then 1° C above the gelation temperature. The non-linear aging and recovery properties were assessed through the following protocol: after equilibration at the test temperature as previously defined, cycles of yielding-recovery were performed. In a first step, oscillatory strain sweeps at a frequency $\omega = 6.28$ rad/s are carried out and stopped after reaching the crossover strain for which the elastic and viscous modulus are equal $G' = G$". In a second step, time sweeps at 4% strain were carried out until reaching an equilibrium plateau for the elastic modulus. If a gel is recovered after the second step, the cycle is repeated until no gel can be reformed.

A.3 Results

A.3.1 Grafting of pnipam on fd virus

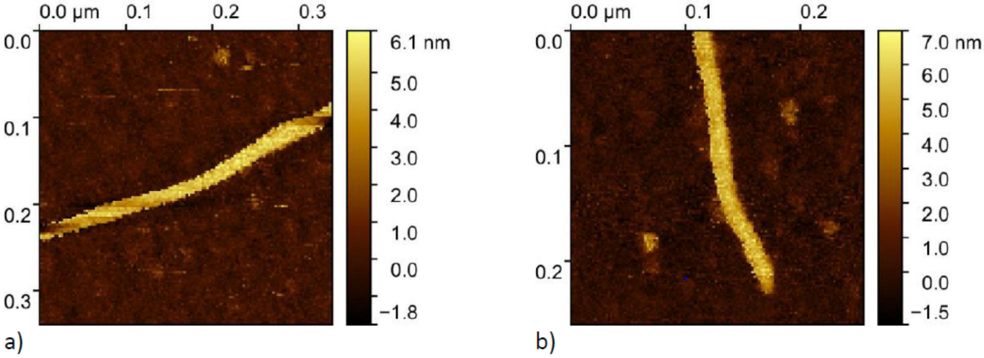

Figure A.3: AFM pictures of a) fd wild type b) 2k pnipam coated fd virus, *batch 3*.

In the case of the grafting trials with commercial pnipam polymers, for both *batches 2 and 3*, no gelation was detected by the turning vial technique, dynamic light scattering tests, and rheological analysis, regardless of the buffer ionic strength and probing temperature. The commercial polymers purchased from Polymer Source did not dissolve in the ice-cooled reaction buffer, which we attribute to impurities in the polymer. We thus assume that this prevented grafting from taking place in *batch 2*.

The 2k commercial polymers from Sigma Aldrich successfully dissolved in the reaction buffer. Further analysis was then carried out in order to check the polymer's reactivity. NMR studies, data not displayed here, showed that the commercial polymer used was 70% hydrolyzed from the start, but still had reactive groups. NMR tests on small amino-terminated molecules, data not displayed here, showed that the reaction indeed takes place between the NHS group of the polymer and the amino group. This argument is in favour of a successful grafting of the polymer on the fd backbone. Fig. A.3 shows AFM pictures of the bare fd virus and the pnipam grafted fd virus: the dna structure was less visible on the pnipam grafted fd sample than the bare fd sample was evidenced, therefore further validating existence of a grafted layer. Gelation should therefore be theoretically possible, according to calculations of the electrostatic and steric layer at ionic strengths of 100 mM and 150 mM. We thus infer that the absence of gelation of *batch 3* could be due to the fact that the grafted pnipam length of 2k may be too small to undergo a coil to globule transition, as reported for pnipam grafted surfaces [167]. Lastly, small scale grafting of custom synthetized, TFP terminated 10 k polymers [22], *batch 4*, was successful: the vial turning, birefringence [22] and inclusion stoppage all evidenced gelation for *batch 4*. However, larger scale synthesis did not succeed.

A.3.2 Rheology of pnipam grafted fd gels

Fig. A.4 displays typical yielding-recovery tests for a weak *batch 1* gel, with $c = 3$ mg/mL, $I = 10$ mM, $T = 36°$ C. The best recovery behaviour was evidenced for low concentrations, ionic strength, and temperature. For the "strong gels", the initial structure is more difficult to reform after yielding, and a liquid is obtained after the second yielding, data not shown there. An increased electrostatic length, distance between neighbouring rods, as well as a low hydrophobicity of the pnipam chains thus seems to promotes gel recovery, which is associated to weaker bonds between its individual components.

A.4 Conclusion

Although the grafting of 2k pnipam polymers is succesful, gelation does not take place. The small length of the polymer may prevent the coil to globular transition when grafted at the virus surface. Gelation of fd virus grafted with custom synthetized pnipam chains succeeded only for small scale production of the polymer, thus preventing us to start extensive rheological studies. A possible solution may be to graft fd virus with another thermo-responsive polymer than pnipam, such as the copolymer of N-Isopropylacrylamide and N-tert-Butylacrylamide, which may be easier to graft on virus [166] and may facilitate the formation of thermoresponsive gels. Lastly, fd virus suspensions grafted with pnipam polymers where shown to display interesting recovery properties above the gelation temperature. Those promising preliminary results show that recovery is optimized at low concentrations, ionic strength and temperatures as that may promote the formation of weak, easy to reform gels. Such systems would provide key insights on stabilization properties of inclusions by a model suspension of attractive rods, as a function gel strength, and following successive gel yielding. Furthermore, the influence of a varying fraction of inclusions on gel recovery [109] would be of interest.

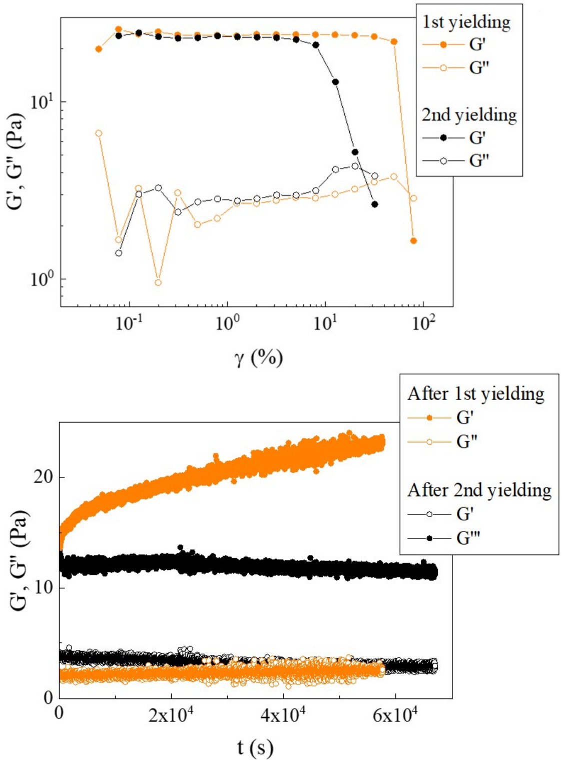

Figure A.4: a) Oscillatory dynamic strain sweeps for a pnipam grafted fd virus sample at $c = 3$ mg/mL in a 100 mM Tris buffer. The first dynamic strain sweep is stopped right after yielding, defined here as G’<G". Then following recovery and equilibration of linear properties, a second dynamic strain sweep is perfomed, and stopped after yielding. b) Oscillatory dynamic time sweeps for a pnipam grafted fd virus sample at $c = 3$ mg/mL in a 100 mM Tris buffer. The time sweeps after the first and the second dynamic strain sweep start just after the critical strain in the strain sweeps corresponding to an higher viscous than elastic modulus has been reached.

A.5 Acknowledgements

Dr. Lucille Chambon is acknowledged for the collaboration, in particular the synthesis, characterization of custom pnipam polymers, and the experiments on small molecules simulating fd virus, to assess reactivity. Pr. Dr. Maria Vamvakaki is acknowledged for the discussions and the access to her lab and group meetings at the University of Creta. Dr. Johan Buitenhuis, Pr. Eric Grelet and Dr. Hu Tang are acknowledged for the useful discussions on fd grafting and systems of thermoresponsive rods. S. Nicolae is acknowledged for the grafting of commercial pnipam sample on the fd rods.

Bibliography

[1] Ahonguio, F. *Ecoulements de fluides à seuil autour d' obstacles.* PhD thesis, Université Grenoble Alpes, 2016.

[2] Alvarez, L., Lettinga, M. P., and Grelet, E. Fast Diffusion of Long Guest Rods in a Lamellar Phase of Short Host Particles. *Physical Review Letters 118*, 17 (2017), 1–5.

[3] Ancey, C., and Jorrot, H. Yield stress for particle suspensions within a clay dispersion. *Journal of Rheology 45*, 2 (2001), 297–319.

[4] Anton, M., Le Denmat, M., Beaumal, V., and Pilet, P. Filler effects of oil droplets on the rheology of heat-set emulsion gels prepared with egg yolk and egg yolk fractions. *Colloids and Surfaces B: Biointerfaces 21*, 1-3 (2001), 137–147.

[5] Arigo, M. T., and McKinley, G. H. An experimental investigation of negative wakes behind spheres settling in a shear-thinning viscoelastic fluid. *Rheologica Acta 37*, 4 (1998), 307–327.

[6] Atapattu, D. D., Chhabra, R. P., and Uhlherr, P. H. Creeping sphere motion in Herschel-Bulkley fluids: flow field and drag. *Journal of Non-Newtonian Fluid Mechanics 59*, 2-3 (1995), 245–265.

[7] Au, P.-i., and Leong, Y.-k. Applied Clay Science Surface chemistry and rheology of Laponite dispersions — Zeta potential , yield stress , ageing , fractal dimension and pyrophosphate. *Applied Clay Science 107* (2015), 36–45.

[8] Bagdassarov, N., and Pinkerton, H. Transient phenomena in vesicular lava flows based on laboratory experiments with analogue materials. *Journal of Volcanology and Geothermal Research 132* (2004), 115–136.

[9] Ballesta, P., Koumakis, N., Besseling, R., Poon, W. C., and Petekidis, G. Slip of gels in colloid-polymer mixtures under shear. *Soft Matter 9*, 12 (2013), 3237–3245.

[10] Balmforth, N. J., Frigaard, I. A., and Ovarlez, G. Yielding to Stress: Recent Developments in Viscoplastic Fluid Mechanics. *Annual Review of Fluid Mechanics 46*, 1 (2014), 121–146.

[11] Bannwarth, M. B., Klein, R., Kurch, S., Frey, H., Landfester, K., and Wurm, F. R. Processing and adjusting the hydrophilicity of poly(oxymethylene) (co)polymers: Nanoparticle preparation and film formation. *Polymer Chemistry 7*, 1 (2016), 184–190.

[12] Barabé, B., Abakumov, S., Gunes, D. Z., and Lettinga, M. P. Sedimentation of large particles in a suspension of colloidal rods. *Physics of Fluids 32*, 5 (2020).

[13] Barnes, H. A., and Walters, K. The yield stress myth? *Rheologica Acta 326* (1985), 323–326.

[14] Barry, E., Beller, D., and Dogic, Z. A model liquid crystalline system based on rodlike viruses with variable chirality and persistence length. *Soft Matter 5*, 13 (2009), 2563–2570.

[15] Beaulne, M., and Mitsoulis, E. Creeping motion of a sphere in tubes filled with Herschel-Bulkley fluids. *Journal of Non-Newtonian Fluid Mechanics 72*, 1 (1997), 55–71.

[16] Bentz, D. P., Ferraris, C. F., Galler, M. A., Hansen, A. S., and Guynn, J. M. Influence of particle size distributions on yield stress and viscosity of cement-fly ash pastes. *Cement and Concrete Research 42*, 2 (2012), 404–409.

[17] Beris, A. N., Tsamopoulos, J. A., Armstrong, R. C., and Brown, R. A. Creeping motion of a sphere through a Bingham plastic. *Journal of Fluid Mechanics 158* (1985), 219–244.

[18] Blackery, J., and Mitsoulis, E. Creeping motion of a sphere in tubes filled with a Bingham plastic material. *J. Non-Newtonian Fluid Mech.*, 70 (1997), 59–77.

[19] Bonn, D., Denn, M. M., Berthier, L., Divoux, T., and Manneville, S. Yield stress materials in soft condensed matter. *Reviews of Modern Physics 89*, 3 (2017), 1–44.

[20] Bringer, A., Eisenriegler, E., Schlesener, F., and Hanke, A. Polymer depletion interaction between a particle and a wall. *European Physical Journal B 11*, 1 (1999), 101–119.

[21] Cantat, I., Pitois, O., Cantat, I., and Pitois, O. Stokes experiment in a liquid foam. *Journal of Physics: Condensed Matter 17*, 45 (2006), S3455—-S3461.

[22] Chambon, L. *Anisotropic particles : synthesis and characterisation of responsive rod-like colloids.* PhD thesis, University of Crete, 2019.

[23] Chambon, L., and Vamvakaki, M. Hollow polymer microrods of tunable flexibility from dense amphiphilic block copolymer brushes. *Soft Matter 16*, 3 (2020), 833–841.

[24] Chaparian, E., and Frigaard, I. A. Cloaking: Particles in a yield-stress fluid. *Journal of Non-Newtonian Fluid Mechanics 243* (2017), 47–55.

[25] Chaparian, E., and Frigaard, I. A. Yield limit analysis of particle motion in a yield-stress fluid. *Journal of Fluid Mechanics 819* (2017), 311–351.

[26] Chaparian, E., Wachs, A., and Frigaard, I. A. Inline motion and hydrodynamic interaction of 2D particles in a viscoplastic fluid. *Physics of Fluids 30*, 3 (2018).

[27] Chapot, D., Bocquet, L., and Trizac, E. Interaction between charged anisotropic macromolecules: Application to rod-like polyelectrolytes. *Journal of Chemical Physics 120*, 8 (2004), 3969–3982.

[28] Chateau, X., Ovarlez, G., and Trung, K. L. Homogenization approach to the behavior of suspensions of noncolloidal particles in yield stress fluids. *Journal of Rheology,American Institute of Physics 52*, 2 (2008), 489–506.

[29] Cheddadi, I., Saramito, P., Dollet, B., Raufaste, C., and Graner, F. Understanding and predicting viscous, elastic, plastic flows. *European Physical Journal E 34*, 1 (2011), 1–15.

[30] Chen, J., and Dickinson, E. Effect of surface character of filler particles on rheology of heat-set whey protein emulsion gels. *Colloids and Surfaces B: Biointerfaces 12*, 3-6 (1999), 373–381.

[31] Chen, S., and Rothstein, J. P. Flow of a wormlike micelle solution past a falling sphere. *Journal of Non-Newtonian Fluid Mechanics 116*, 2-3 (2004), 205–234.

[32] Chhabra, R. P. *Bubbles, Drops and Particles in Non-Newtonian Fluids*, second edi ed. CRC Press, Taylor and Francis Group, 2007.

[33] Chung, C McClements, D. J. Structure-function relationships in food emulsions : Improving food quality and sensory perception. *Food Structure 1*, 2 (2013), 106–126.

[34] Cohen-Addad, S., and Höhler, R. Rheology of foams and highly concentrated emulsions. *Current Opinion in Colloid and Interface Science 19*, 6 (2014), 536–548.

[35] Coussot, P. Bingham' s heritage. *Rheologica Acta 56* (2017), 163–176.

[36] Cox, S. J., Alonso, M. D., Hutzler, S., and Weaire, D. The Stokes experiment in a foam.

[37] Cox, S. J., and Davies, I. T. Bubble entrainment by a sphere falling through a horizontal soap foam. *Epl (Europhysics letters) 130*, 1 (2020).

[38] Dagois-Bohy, S., Hormozi, S., Guazzelli, É., and Pouliquen, O. Rheology of dense suspensions of non-colloidal spheres in yield-stress fluids. *Journal of Fluid Mechanics 776* (2015), R2.

[39] Damineli, B. L., John, V. M., Lagerblad, B., and Pileggi, R. G. Viscosity prediction of cement-filler suspensions using interference model : A route for binder efficiency enhancement. *Cement and Concrete Research 84* (2016), 8–19.

[40] Das, M., and Petekidis, G. Microstructural changes in colloidal rod glasses undergoing shear flow – Investigation by rheology and confocal microscopy. 2018.

[41] Daugan, S., Talini, L., Herzhaft, B., and Allain, C. Aggregation of particles settling in shear-thinning fluids. Part 2 - Three-particle aggregation. *European Physical Journal E 9*, 1 (2002), 55–62.

[42] Davies, I. T., and Cox, S. J. Sedimenting discs in a two-dimensional foam. *Colloids and Surfaces A: Physicochemical and Engineering Aspects 344*, 1-3 (2009), 8–14.

[43] Dogic, Z., Zhang, J., Lau, A. W., Aranda-Espinoza, H., Dalhaimer, P., Discher, D. E., Janmey, P. A., Kamien, R. D., Lubensky, T. C., and Yodh, A. G. Elongation and fluctuations of semiflexible polymers in a nematic solvent. *Phys Rev Lett 92*, 12 (2004), 125503.

[44] Doi, M., and Edwards, S. F. The Theory of Polymer Dynamics. *Journal of Non-Newtonian Fluid Mechanics 25* (1987), 385–386.

[45] Dollet, B., Elias, F., Quilliet, C., Huillier, A., Aubouy, M., and Graner, F. Two-dimensional flows of foam: Drag exerted on circular obstacles and dissipation. *Colloids and Surfaces A: Physicochemical and Engineering Aspects 263*, 1-3 SPEC. ISS. (2005), 101–110.

[46] Dombrowski, J., Johler, F., Warncke, M., and Kulozik, U. Correlation between bulk characteristics of aggregated β-lactoglobulin and its surface and foaming properties. *Food Hydrocolloids 61* (2016), 318–328.

[47] Doorn, J. M. V., Sprakel, J., and Kodger, T. E. Well-Defined Grafted Polymeric Surfaces. *Gels 3*, 21 (2017).

[48] Du, L., and Folliard, K. J. Mechanisms of air entrainment in concrete. *Cement and Concrete Research 35*, 8 (2005), 1463–1471.

[49] Ducloué, L., Pitois, O., Goyon, J., Chateau, X., and Ovarlez, G. Coupling of elasticity to capillarity in soft aerated materials. *Soft Matter 10*, 28 (2014), 5093–5098.

[50] Ducloué, L., Pitois, O., Goyon, J., Chateau, X., and Ovarlez, G. Rheological behaviour of suspensions of bubbles in yield stress fluids. *Journal of Non-Newtonian Fluid Mechanics 215* (2015), 31–39.

[51] Emady, H., Caggioni, M., and Spicer, P. Colloidal microstructure effects on particle sedimentation in yield stress fluids. *Journal of Rheology 57*, 6 (2013), 1761–1772.

[52] Erdogan. *Determination of Aggregate Shape Properties Using X-ray Tomographic Methods and the Effect of Shape on Concrete Rheology.* PhD thesis, University of Texas, 2005.

[53] Fahs, H., Ovarlez, G., and Chateau, X. Pair-particle trajectories in a shear flow of a Bingham fluid. *Journal of Non-Newtonian Fluid Mechanics 261*, July (2018), 171–187.

[54] Farahnaky, A., Abbasi, A., Jamalian, J., and Mesbahi, G. The use of tomato pulp powder as a thickening agent in the formulation of tomato ketchup. *Journal of texture studies 39*, 2 (2008), 169–182.

[55] Feneuil, B., Roussel, N., and Pitois, O. Yield stress of aerated cement paste. *Cement and Concrete Research 127*, June 2019 (2020), 105922.

[56] Fernández-Rico, C., Yanagishima, T., Curran, A., Aarts, D. G., and Dullens, R. P. Synthesis of Colloidal SU-8 Polymer Rods Using Sonication. *Advanced Materials 31*, 17 (2019).

[57] Firouznia, M., Metzger, B., Ovarlez, G., and Hormozi, S. The interaction of two spherical particles in simple-shear flows of yield stress fluids. *Journal of Non-Newtonian Fluid Mechanics 255* (2018), 19–38.

[58] Fraggedakis, D., Dimakopoulos, Y., and Tsamopoulos, J. Yielding the yield-stress analysis: A study focused on the effects of elasticity on the settling of a single spherical particle in simple yield-stress fluids. *Soft Matter 12*, 24 (2016), 5378–5401.

[59] Garduño, I. E., Tamaddon-jahromi, H. R., Webster, M. F., Ciencias, C. D., Tecnológico, D., Nacional, U., México, A. D., and México, C. D. Flow past a sphere : Predicting enhanced drag with shear-thinning fluids , dissipative and constant shear-viscosity models. *Journal of Non-Newtonian Fluid Mechanics 244* (2017), 25–41.

[60] Geiker, M. R., and al, E. On the effect of coarse aggregate fraction and shape on the properties of self compacting concrete. *Cement, Concrete and Aggregates 24*, 1 (2002), 3–6.

[61] Goyon, J., Bertrand, F., Pitois, O., and Ovarlez, G. Shear induced drainage in foamy yield-stress fluids. *Physical Review Letters 104*, 12 (2010), 1–10.

[62] Gravelle, A. J., Nicholson, R. A., Barbut, S., and Marangoni, A. G. The impact of model rigid fillers in acid-induced sodium caseinate/xanthan gum cooperative protein gels. *Food Hydrocolloids 113*, October 2020 (2021), 106439.

[63] Grelet, E. Hexagonal order in crystalline and columnar phases of hard rods. *Physical Review Letters 100*, 16 (2008), 1–4.

[64] Grelet, E., and Fraden, S. What is the origin of chirality in the cholesteric phase of virus suspensions? *Phys Rev Lett 90*, 19 (2003), 198302.

[65] Gueslin, B., Talini, L., Herzhaft, B., Peysson, Y., and Allain, C. Flow induced by a sphere settling in an aging yield-stress fluid . *Physics of Fluids 18* (2006), 1–20.

[66] Guggisberg, D., Cuthbert-Steven, J., Piccinali, P., Bütikofer, U., and Eberhard, P. Rheological, microstructural and sensory characterization of low-fat and whole milk set yoghurt as influenced by inulin addition. *International Dairy Journal 19*, 2 (2009), 107–115.

[67] Gumulya, M. M., Horsley, R. R., Pareek, V., and Lichti, D. D. The effects of fluid viscoelasticity on the settling behaviour of horizontally aligned spheres. *Chemical Engineering Science 66*, 23 (2011), 5822–5831.

[68] Guu, D. M. *Rod-sphere mixture in equilibrium and under shear flow.* PhD thesis, Heinrich–Heine–Universität Düsseldorf, 2014.

[69] Hafid, H., Ovarlez, G., Toussaint, F., Jezequel, P. H., and Roussel, N. Effect of particle morphological parameters on sand grains packing properties and rheology of model mortars. *Cement and Concrete Research 80* (2016), 44–51.

[70] Harlen, O. G. The negative wake behind a sphere sedimenting through a viscoelastic fluid. *Journal of Non-Newtonian Fluid Mechanics 108*, 1-3 (2002), 411–430.

[71] Holenberg, Y., Lavrenteva, O. M., Shavit, U., and Nir, A. Particle tracking velocimetry and particle image velocimetry study of the slow motion of rough and smooth solid spheres in a yield-stress fluid. *Physical Review E 86*, 066301 (2012), 1–6.

[72] Ireland, P. M., and Jameson, G. J. Drag force on a spherical particle moving through a foam: The role of wettability. *International Journal of Mineral Processing 102-103* (2012), 78–88.

[73] Jaensson, N. O., Hulsen, M. A., and Anderson, P. D. Direct numerical simulation of particle alignment in viscoelastic fluids. *Journal of Non-Newtonian Fluid Mechanics 235* (2016), 125–142.

[74] Ji, X., Oh, J., Dunker, A. K., and Hipps, K. W. Effects of relative humidity and applied force on atomic force microscopy images of the filamentous phage fd. *Ultramicroscopy 72*, 3-4 (1998), 165–176.

[75] John C. Crocker, D. G. G. Methods of Digital Video Microscopy for Colloidal Studies. *Journal of colloid and interface science 310*, 179 (1996), 298–310.

[76] Joshi, Y. M., Reddy, G. R. K., Kulkarni, A. L., Kumar, N., and Chhabra, R. P. Rheological Behavior of Aqueous Suspensions of Laponite : New Insights into the Ageing Phenomena. *Proc. R. Soc. A.* (2008), 464469–489.

[77] Jossic, L., Briguet, A., and Magnin, A. Segregation under flow of objects suspended in a yield stress fluid and NMR imaging visualisation. *Chemical Engineering Science 57*, 3 (2002), 409–418.

[78] Jossic, L., and Magnin, A. Drag and stability of objects in a yield stress fluid. *AIChE Journal 47*, 12 (2001), 2666–2672.

[79] Jossic, L., and Magnin, A. Drag of an isolated cylinder and interactions between two cylinders in yield stress fluids. *Journal of Non-Newtonian Fluid Mechanics 164*, 1-3 (2009), 9–16.

[80] Kang, K., Gapinski, J., Lettinga, M. P., Buitenhuis, J., Meier, G., Ratajczyk, M., Dhont, J. K., and Patkowski, A. Diffusion of spheres in crowded suspensions of rods. *J Chem Phys 122*, 4 (2005), 44905.

[81] Kang, K., Wilk, A., Buitenhuis, J., Patkowski, A., and Dhont, J. K. Diffusion of spheres in isotropic and nematic suspensions of rods. *J Chem Phys 124*, 4 (2006), 44907.

[82] Kelessidis, V. C., and Mpandelis, G. Measurements and prediction of terminal velocity of solid spheres falling through stagnant pseudoplastic liquids. *Powder Technology 147*, 1-3 (2004), 117–125.

[83] Kemiha, M., Frank, X., Poncin, S., and Li, H. Z. Origin of the negative wake behind a bubble rising in non-Newtonian fluids. *Chemical Engineering Science 61*, 12 (2006), 4041–4047.

[84] Kirimlidou, M., Matsakidou, A., Scholten, E., Nikiforidis, C. V., and Kiosseoglou, V. Composite gels structured by a gelatin protein matrix filled with oil bodies. *Food Structure 14*, June (2017), 46–51.

[85] Kogan, M., Ducloué, L., Goyon, J., Chateau, X., Pitois, O., and Ovarlez, G. Mixtures of foam and paste: Suspensions of bubbles in yield stress fluids. *Rheologica Acta 52*, 3 (2013), 237–253.

[86] Kostrzewa, M., Delgado, A., and Wierschem, A. Particle settling in micellar solutions of varying concentration and salt content. *Acta Mechanica 227*, 3 (2016), 677–692.

[87] Koumakis, N., and al, E. Colloidal gels under shear : Strain rate effects. *AIP Conf. Proc. 1518*, 365 (2013).

[88] Koumakis, N., Moghimi, E., Besseling, R., Poon, W. C., Brady, J. F., and Petekidis, G. Tuning colloidal gels by shear. *Soft Matter 11*, 23 (2015), 4640–4648.

[89] Koumakis, N., Pamvouxoglou, A., Poulos, A. S., and Petekidis, G. Direct comparison of the rheology of model hard and soft particle glasses. *Soft Matter 8*, 15 (2012), 4271–4284.

[90] Koumakis, N., and Petekidis, G. Two step yielding in attractive colloids : Transition from gels to attractive glasses. *Soft Matter 7* (2011), 2456.

[91] Koumakis, N. N. *A study on the effects of interparticle interactions on the dynamics, rheology and aging of colloidal systems out of equilibrium.* PhD thesis, University of Crete, 2011.

[92] Kumar, G., and Natale, G. Settling dynamics of two spheres in a suspension of Brownian rods. *Physics of Fluids 073104*, June (2019).

[93] Lang, C., Kohlbrecher, J., Porcar, L., Radulescu, A., Sellinghoff, K., Dhont, J. K. G., and Lettinga, M. P. Microstructural Understanding of the Length- And Stiffness-Dependent Shear Thinning in Semidilute Colloidal Rods. *Macromolecules* (2019).

[94] Laurati, M., Petekidis, G., Koumakis, N., Cardinaux, F., Schofield, B., Brader, J. M., Fuchs, M., Egelhaaf, S. U., Matter, C., and Road, M. Structure, dynamics, and rheology of colloid-polymer mixtures: From liquids to gels. *J. Chem. Phys. 134907* (130).

[95] Le Goff, A., Quéré, D., and Clanet, C. Shooting in a foam. *Soft Matter 10* (2014), 6696–6704.

[96] Lettinga, M. P., Dhont, J. K., Zhang, Z., Messlinger, S., and Gompper, G. Hydrodynamic interactions in rod suspensions with orientational ordering. *Soft Matter 6*, 18 (2010), 4556–4562.

[97] Liu, A., and Nagel, S. *Jamming and Rheology: Constrained Dynamics on Microscopic and Macroscopic Scales*, london: cr ed. CRC Press, 2001.

[98] Macosko, C. W. *Rheology: Principles, Measurements, and Applications.* Wiley-WCH, 1994.

[99] Mahaut, F., Chateau, X., Coussot, P., and Ovarlez, G. Yield stress and elastic modulus of suspensions of noncolloidal particles in yield stress fluids. *Journal of Rheology 52*, 1 (2008), 287.

[100] Mahaut, F., Mokéddem, S., Chateau, X., Roussel, N., and Ovarlez, G. Effect of coarse particle volume fraction on the yield stress and thixotropy of cementitious materials. *Cement and Concrete Research 38*, 11 (2008), 1276–1285.

[101] Mahmood, H. Y. Theoretical investigation of wall effect on drag coefficient of different particles shape moving in non-Newtonian fluids.

Global Journal of Engineering Science and Research Management, January (2016).

[102] Malhotra, S., and Sharma, M. M. Settling of spherical particles in unbounded and confined surfactant-based shear thinning viscoelastic fluids: An experimental study. *Chemical Engineering Science 84* (2012), 646–655.

[103] Mehta, M., Shah, N., and Shah, S. Gellified Emulsion : A Review of State of Art and Recent Advances. *Journal of Pharmaceutical Science and Bioscientific Research 6*, 2271 (2016), 420–426.

[104] Mendoza-Fuentes, A. J., Manero, O., and Zenit, R. Evaluation of drag correction factor for spheres settling in associative polymers. *Rheologica Acta 49*, 9 (2010), 979–984.

[105] Merkak, O., Jossic, L., and Magnin, A. Spheres and interactions between spheres moving at very low velocities in a yield stress fluid. *Journal of Non-Newtonian Fluid Mechanics 133* (2006), 99–108.

[106] Mewis. *Colloidal suspensions rheology.* Cambridge University Press, 2001.

[107] Mirzaagha, S., Pasquino, R., Iuliano, E., D'Avino, G., Zonfrilli, F., Guida, V., and Grizzuti, N. The rising motion of spheres in structured fluids with yield stress. *Physics of Fluids 29*, 9 (2017).

[108] Missirlis, K. A., Assimacopoulos, D., Mitsoulis, E., and Chhabra, R. P. Wall effects for motion of spheres in power-law fluids. *Journal of Non-Newtonian Fluid Mechanics 96*, 3 (2001), 459–471.

[109] Moghimi, E., Jacob, A. R., Koumakis, N., and Petekidis, G. Colloidal Gels Tuned by Oscillatory Shear. *Soft Matter 13* (2017), 2371–2383.

[110] Mohammadigoushki, H., and Muller, S. J. Sedimentation of a sphere in wormlike micellar fluids. *Journal of Rheology 60*, 4 (2016), 587–601.

[111] Møller, P. C. F., and Bonn, D. Yield stress and thixotropy : on the difficulty of measuring yield stresses in practice. *Soft Matter 2* (2006), 274–283.

[112] Moseley, K., Fairweather, M., and Harbottle, D. Settling dynamics of two identical vertically aligned spheres in a thixotropic fluid. *Journal of Non-Newtonian Fluid Mechanics 271* (2019).

[113] Mrokowska, M. M., and Krztoń-Maziopa, A. Viscoelastic and shear-thinning effects of aqueous exopolymer solution on disk and sphere settling. *Scientific Reports 9*, 1 (2019), 1–13.

[114] Neirynck, N., Meeren, P. V. D., Gorbe, S. B., Dierckx, S., and Dewettinck, K. Improved emulsion stabilizing properties of whey protein isolate by conjugation with pectins. *Food Hydrocolloids* (2004).

[115] Nelson, A. Z., and Ewoldt, R. H. Design of yield-stress fluids: A rheology-to-structure inverse problem. *Soft Matter 13*, 41 (2017), 7578–7594.

[116] Nelson, A. Z., Schweizer, K. S., Rauzan, B. M., Nuzzo, R. G., Vermant, J., and Ewoldt, R. H. Designing and transforming yield-stress fluids. *Current Opinion in Solid State and Materials Science 23*, 5 (2019), 100758.

[117] Ning, M., Zeng, Z., Han, M., Xu, Z., Zhang, B., Wang, P., Kong, W., Jia, J., and Liu, Q. Study on the Performance of a New Type of Anionic-nonionic Surfactant. *IOP Conference Series: Earth and Environmental Science 446*, 2 (2020).

[118] Nirmalkar, N., Chhabra, R. P., and Poole, R. J. On creeping flow of a Bingham plastic fluid past a square cylinder. *Journal of Non-Newtonian Fluid Mechanics 171-172* (2012), 17–30.

[119] Okesanya, T., Abdukarimov, A., and Kuru, E. Generalized models for predicting the drag coefficient and settling velocity of rigid spheres in viscoelastic and viscoinelastic power-law fluids. *Journal of Petroleum Science and Engineering 191*, February (2020), 107077.

[120] Oldenbourg, R., Wen, X., Meyer, R. B., and Caspar, D. L. D. Orientational Distribution Function in Nematic Tobacco-Mosaic-Virus Liquid Crystals Measured by X-Ray Diffraction. *Physical Review Letters 61*, 1851 (1988).

[121] Onsager, L. the Effects of Shape on the Interaction of Colloidal Particles. *Annals of the New York Academy of Sciences 51*, 4 (1949), 627–659.

[122] Oosawa, F. On Interaction between Two Bodies Immersed in a Solution of Macromolecules. *American Institute of Physics 22* (1954), 1255.

[123] Ovarlez, G., Barral, Q., and Coussot, P. Three-dimensional jamming and flows of soft glassy materials. *Nature Materials 9*, 2 (2010), 115–119.

[124] Ovarlez, G., Bertrand, F., Coussot, P., and Chateau, X. Shear-induced sedimentation in yield stress fluids. *Journal of Non-Newtonian Fluid Mechanics 177-178* (2012), 19–28.

[125] Ovarlez, G., Krishan, K., Goyon, J., and Coussot, P. On the existence of a simple yield stress fluid behavior. *J Non-Newtonian Fluid Mech 193* (2013), 68–79.

[126] Ovarlez, G., Mahaut, F., Deboeuf, S., Lenoir, N., Hormozi, S., and Chateau, X. Flows of suspensions of particles in yield stress fluids. *Journal of Rheology 59*, 6 (2015), 1449–1486.

[127] Ozogul, H. *Écoulements De Fluides À Seuil Autour D ' Un Cylindre En Milieu Confiné*. PhD thesis, Université Grenoble Alpes, 2016.

[128] P. Coussot. Aging and solid or liquid behavior in pastes. *Journal of Rheology 50*, 975 (2006).

[129] Papanastasiou, T. C. Flows of Materials with Yield. *Journal of Rheology 31*, 5 (1987), 385–404.

[130] Peysson, B. G. L. T. Y. Sphere settling in an aging yield stress fluid : link between the induced flows and the rheological behavior. *Rheologica Acta* (2009), 961–970.

[131] Piech, M., Weronski, P., Wu, X., and Walz, J. Y. Prediction and measurement of the interparticle depletion interaction next to a flat wall. *Journal of Colloid and Interface Science 247*, 2 (2002), 327–341.

[132] Poon, W. C. K. Colloidal Glasses. *MRS Bulletin 29*, 02 (2004), 96–99.

[133] Putz, A., and Frigaard, I. A. Creeping flow around particles in a Bingham fluid. *Journal of Non-Newtonian Fluid Mechanics 165*, 5-6 (2010), 263–280.

[134] Putz, A. M., Burghelea, T. I., Frigaard, I. A., and Martinez, D. M. Settling of an isolated spherical particle in a yield stress shear thinning fluid. *Physics of Fluids 20*, 3 (2008).

[135] Qiao, Z., Wang, Z., Zhang, C., Yuan, S., Zhu, Y., and Wang, J. Merkak. *AIChE Journal 59*, 4 (2012), 215–228.

[136] Reddy, N. K., and Zhang, Z. Probing structure in colloidal gels of thermoreversible rodlike virus particles : Rheology and scattering. *Journal of Rheology 56*, 5 (2012), 1153–1174.

[137] Reddy, N. K., Zhang, Z., Lettinga, M. P., Dhont, J. K., and Vermant, J. Rheology and Structure of Thermoreversible Gels of Sticky Rod-Like Particles. In *Colloidal Mikado* (2010).

[138] Rooki, R., Ardejani, F. D., Moradzadeh, A., Kelessidis, V. C., and Nourozi, M. Prediction of terminal velocity of solid spheres falling through Newtonian and non-Newtonian pseudoplastic power law fl uid using artificial neural network. *International Journal of Mineral Processing 110-111* (2012), 53–61.

[139] Rouyer, F., Cohen-Addad, S., and Höhler, R. Is the yield stress of aqueous foam a well-defined quantity? *Colloids and Surfaces A: Physicochemical and Engineering Aspects 263*, 1-3 SPEC. ISS. (2005), 111–116.

[140] Saha, S., Saint-Michel, B., Leynes, V., Binks, B. P., and Garbin, V. Stability of bubbles in wax-based oleofoams: decoupling the effects of bulk oleogel rheology and interfacial rheology. *Rheologica Acta 59*, 4 (2020), 255–266.

[141] Schindelin, J., Arganda-Carreras, I., Frise, E., Kaynig, V., Longair, M., Pietzsch, T., Preibisch, S., Rueden, C., Saalfeld, S., Schmid, B., Tinevez, J. Y., White, D. J., Hartenstein, V., Eliceiri, K., Tomancak, P., and Cardona, A. Fiji: An open-source platform for biological-image analysis. *Nature Methods 9*, 7 (2012), 676–682.

[142] Sgreva, N. R., Davaille, A., Kumagai, I., and Kurita, K. Interaction between a falling sphere and the structure of a non-Newtonian yield-stress fluid. *Journal of Non-Newtonian Fluid Mechanics 284*, December 2019 (2020), 104355.

[143] She, W., Du, Y., Miao, C., Liu, J., Zhao, G., and Jiang, J. Application of organic- and nanoparticle-modified foams in foamed concrete: Reinforcement and stabilization mechanisms. *Cement and Concrete Research* (106), 12–22.

[144] Singh, P., and Joseph, D. D. Fluid dynamics of floating particles. *Journal of Fluid Mechanics 530* (2005), 31–80.

[145] Song, J., Caggioni, M., Squires, T. M., Gilchrist, J. F., Prescott, S. W., and Spicer, P. T. Heterogeneity, suspension, and yielding in sparse microfibrous cellulose gels 1. Bubble rheometer studies. *Rheologica Acta 58*, 5 (2019), 217–229.

[146] Song, J., Caggioni, M., Squires, T. M., Gilchrist, J. F., Prescott, S. W., and Spicer, P. T. Heterogeneity, suspension, and yielding in sparse microfibrous cellulose gels 2: strain rate-dependent two-fluid behavior. *Rheologica Acta 58*, 5 (2019), 231–239.

[147] Sugeng, F., and Tanner, R. I. The drag on spheres in viscoelastic fluids with significant wall effects. *Journal of Non-Newtonian Fluid Mechanics 20*, C (1986), 281–292.

[148] Tabuteau, H., and Coussot, P. Drag force on a sphere in steady motion through a yield-. *J Non-Newtonian Fluid Mech* (2006), 125–137.

[149] Tabuteau, H., Coussot, P., and de Bruyn, J. R. Drag force on a sphere in steady motion through a yield-stress fluid. *Journal of Rheology 51*, 1 (2007), 125–137.

[150] Talini, L. Aggregation of particles settling in shear-thinning fluids. *The European Physical Journal E volume*, October (2002).

[151] Tang, J., and Fraden, S. Isotropic-cholesteric phase transition in colloidal suspensions of filamentous bacteriophage fd. *Liquid Crystals 19:4* (1995), 459–467.

[152] Tokpavi, D. L., Magnin, A., and Jay, P. Very slow flow of Bingham viscoplastic fluid around a circular cylinder. *Journal of Non-Newtonian Fluid Mechanics 154*, 1 (2008), 65–76.

[153] Tolkach, A., and Kulozik, U. Reaction kinetic pathway of reversible and irreversible thermal denaturation of β-lactoglobulin. *Dairy Science and Technology 87*, 4-5 (2007), 301–315.

[154] Tran, A., Rudolph, M. L., and Manga, M. Bubble mobility in mud and magmatic volcanoes. *Journal of Volcanology and Geothermal Research 294* (2015), 11–24.

[155] Trappe, V., Prasad, V., Cipelleti, L., Segre, P. N., and Weitz, D. A. Jamming phase diagram for attractive particles. *Nature 411* (2001), 772–775.

[156] van Vliet, T. Rheological properties of filled gels. Influence of filler matrix interaction. *Colloid & Polymer Science 266*, 6 (1988), 518–524.

[157] Verneuil, E., Phillips, R. J., and Talini, L. Axisymmetric two-sphere sedimentation in a shear thinning viscoelastic fluid: Particle interactions and induced fluid velocity fields. *Journal of Rheology 51*, 6 (2007), 1343–1359.

[158] Völp, A. R., Kagerbauer, L., Engmann, J., Gunes, D. Z., Gehin-Delval, C., and Willenbacher, N. In-situ rheological and structural characterization of milk foams in a commercial foaming device. *Journal of Food Engineering 290* (2021).

[159] Walawender, W. P., Chen, T. Y., and Cala, D. F. An approximate casson fluid model for tube flow of blood. *Biorheology 12*, 2 (1975), 111–119.

[160] Wang, Z., Wang, S., Jing, Z., and Luo, X. Viscoelastic Drag of Particles Settling in Wormlike Micellar Solutions of Varying Surfactant Concentration. *Journal of Dispersion Science and Technology 37:3* (2016), 442–449.

[161] Wang, Z., Wang, S., Xu, L., Dou, Y., and Su, X. Extremely slow settling behavior of particles in dilute wormlike micellar fluid with broad spectrum of relaxation times. *Journal of Dispersion Science and Technology 41*, 5 (2020), 639–647.

[162] Wijarnprecha, K., de Vries, A., Santiwattana, P., Sonwai, S., and Rousseau, D. Rheology and structure of oleogelled water-in-oil emulsions containing dispersed aqueous droplets as inactive fillers. *Lwt 115*, March (2019), 108067.

[163] Willenbacher, N., and Lexis, M. Foam rheology. In *Foam Films and Foams: Fundamentals and Applications.* CRC Press, Boca Raton, 2018, ch. Rheology o.

[164] Wu, S., and Mohammadigoushki, H. Sphere sedimentation in wormlike micelles: Effect of micellar relaxation spectrum and gradients in micellar extensions. *Journal of Rheology 62*, 5 (2018), 1061–1069.

[165] Ying, D. L., and Hyoung, J. C. Electrorheological fluids: smart soft matter and characteristics. *Soft Matter 8* (2012), 11961–11978.

[166] Zhang, Z., Krishna, N., Lettinga, M. P., Vermant, J., Grelet, E., Zhang, Z., Krishna, N., Lettinga, M. P., Vermant, J., Grelet, E., Pascal, P., and Cnrs-uni, V. Reversible Gelation of Rod-Like Viruses Grafted with Thermoresponsive Polymers Reversible Gelation of Rod-Like Viruses Grafted with Thermoresponsive Polymers. *Langmuir 25*, 4 (2009), 2437–2442.

[167] Zhu, X., Yan, C., Winnik, F., and Leckband, D. End-Grafted Low-Molecular-Weight PNIPAM Does Not Collapse above the LCST. *Langmuir 23*, 162-169 (2007).

[168] Zöttl, A., Klop, K. E., Balin, A. K., Gao, Y., Yeomans, J. M., and Aarts, D. G. Dynamics of individual Brownian rods in a microchannel flow. *Soft Matter 15*, 29 (2019), 5810–5814.

[169] İnce Coşkun, A. E., and Özdestan Ocak, Ö. Foaming behavior of colloidal whey protein isolate micro-particle dispersions. *Colloids and Surfaces A: Physicochemical and Engineering Aspects 609*, October 2020 (2021).

Scientific communication

A.6 Publications in peer-reviewed journals

The corresponding author is marked with an asterix.

- BARABÉ, B.*, ABAKUMOV, S., GUNES, D.Z., LETTINGA, M.P.* Sedimentation of large particles in a suspension of colloidal rods, *Physics of Fluids* 32, 053105 (2020); https://doi.org/10.1063/5.0006076.
- BARABÉ, B., GUNES, D.Z., LETTINGA, M.P. Inclusions in yield stress and shear-thinning dispersions: a review. In preparation.
- BARABÉ, B., GUNES, D.Z., LETTINGA, M.P., PETEKIDIS, G. Rheology of inclusion doped model depletion gels. In preparation.
- BARABÉ, B., GUNES, D.Z., LETTINGA, M.P. Critical sinking stress of disks through a foam. In preparation.

A.7 Posters

- “Rheology of doped depletion gels”, Rheo 360° joint symposium from the Belgian Group of Rheology / German Rheological Society, Luxembourg, March 2018.
- “Spherical inclusions in gels: microstructural and aging effects” workshop Playing Colloidal Mikado V, Heraklion, July 2017.

A.8 Presentations in international conferences or workshops

"Sedimentation rate of large inclusions in networks of rod like particles":

- Annual European Rheology Conference, Slovenia, April 2019
- Playing Colloidal Mikado VI, UK, May 2018

FACULTY OF SCIENCE
DEPARTMENT OF PHYSICS AND ASTRONOMY
SOFT MATTER AND BIOPHYSICS
Celestijnenlaan 200A box 2402
B-3001 Leuven
blandine.barabe@kuleuven.be
https://fys.kuleuven.be/zmb